UCLouvain

AGRO LOUVAIN

Faculté des bioingénieurs

Development of Intelligent Piezochromic Materials based on Spin Crossover Complexes

Auteur : Arnaud Nizet

Promoteur(s) : Prof. Yann Garcia

Lecteur(s) : Prof. Bart Van der Bruggen, Prof. Evelyne Van Ruymbeke

Année académique 2021-2022

Mémoire de fin d'études présenté en vue de l'obtention du diplôme de Bioingénieur : Chimie et bio-industries

1. Acknowledgements

First, I would like to thank Prof. Garcia, for his support and guidance, as well as the trust that was given to me.

I would also thank Weiyang Li, Afaf Oulmidi, Yousra Bahjou, Li Sun, Jean-Francois Statsyns, and all other members of the CMOL laboratory who helped me all along the course of this year.

I am grateful for the warm welcome that Prof. Aurelian Rotaru, Prof. Andrei Diaconu, and his team gave me in their laboratory during my stay in Suceava, as well as the tremendous help they provided me. Furthermore, I cannot express enough appreciation for the time and resources the Prof. Rotaru invested in me during my visit.

Finally, I want to thank my family for their continuous support and reassurance, especially during hard times, both mine and theirs. My friends also deserve a special acknowledgement for providing me a shoulder to rest on during moments of doubts.

2. Table of Contents

3. Content Scheme

Here is a graphic representation of the main sections of this work, for more clarity. The width of the rectangles roughly represents the length of each section.

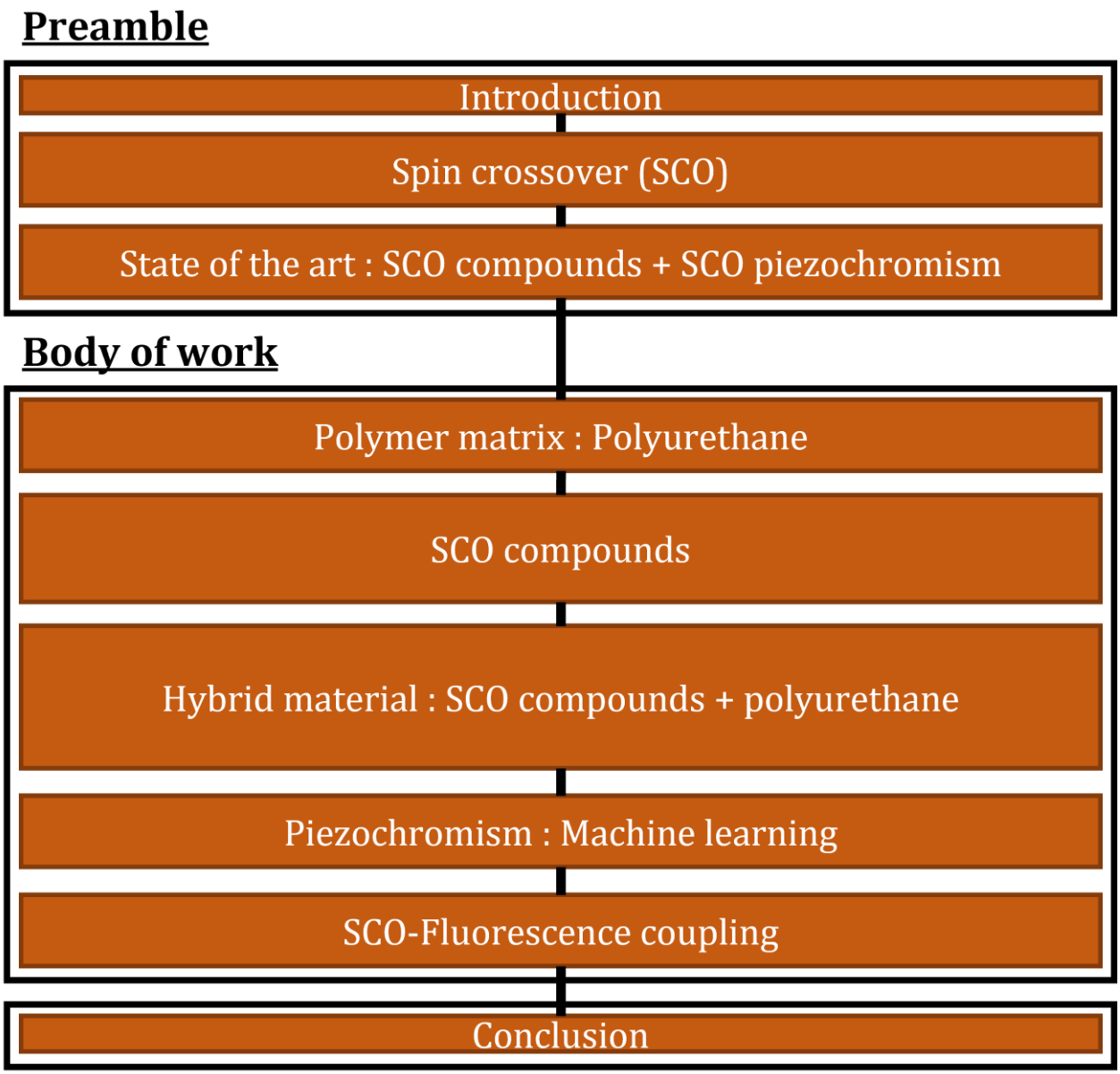

4. Abreviations

SCO : Spin Crossover

SS : Soft segment

CFT : Crystal field theory

LFT : Ligand field theory

DSC : Differential scanning calorimetry

PEG : Polyethylene Glycol

LS : Low spin

HS : High spin

SEM : Scanning electron microscopy

AFM : Atomic force microscopy

HDI : Hexamethylene diisocyanate

IPDI : Isophorone diisocyanate

DMPA : Dimethylol propionic acid

TEA : Triethylamine

EDA : Ethylene diamine

BDL : Butanediol

WBPU : Water-based/Waterborne polyurethane

PU : Polyurethane

RT : Room temperature

TGA : Thermogravimetric analysis

SQUID : Superconducting Quantum Interference Device

FTIR : Fourier transform infrared spectroscopy

PETA : Pentaerythritol triacrylate

ΔG : Gibbs free energy variation

ΔS : Entropy variation

ΔS_{el} : Electronic entropy variation

ΔS_{vib}: Vibrational entropy variation

Γ: Interaction (or cooperativity) parameter

P : Pressure

ΔV : Volume variation

ΔH : Enthalpy variation

γ : Molar fraction

χ : Molar Magnetic susceptibility

R: Universal gas constant

δ: Isomer shift

ΔE_Q : Quadrupole splitting

Δ_O: Octahedral ligand field splitting

Π : Electron pairing energy

Rf : Random Forest model

k-NN : k-Nearest-Neighbours model

MDEA : N-methyl diethanolamine

PUD : Polyurethane dispersion

MOFs : Metal-organic frameworks

RMSE : Root mean square error

5. Introduction

Piezochromic compounds comprise a family of materials which are able to change colour with the application of a pressure, with great potential in pressure sensors technologies. Yet, the domain of piezochromic compounds remains largely unexplored and underexploited both in the research field and in industry, even though this technology represents a real opportunity in industrial settings. Indeed, they would allow to detect potential damages earlier, allow for safer and more reliable transportation (railways safety components, naval hulls, automotive parts), energy generation (wind turbines, nuclear etc.) and aeronautical and defense composite materials. The sensors market reflects this potential with a new ever-increasing demand for effective sensors technologies (Figure 1). [1]

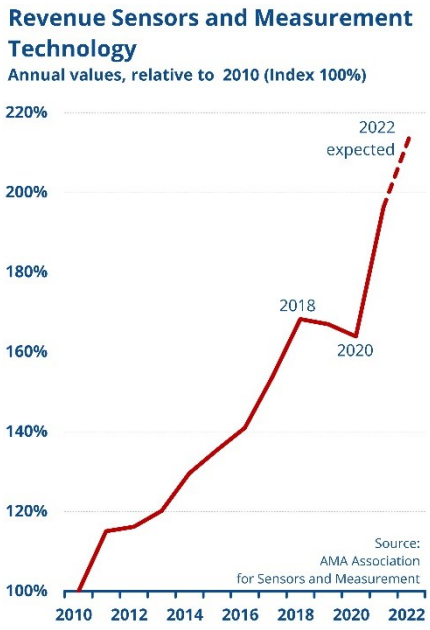

Figure 1 Growth of the sensors market [1]

Moreover, nowadays early structural damage assessments are usually done using sophisticated ultrasonic [2] and eddy current [3] techniques to probe the materials' inner structure. However, these techniques are expensive, complex, and only realizable sporadically, increasing the likelihood that critical damages might be missed. With this in mind, the alternative of using piezochromic coatings present the obvious advantages of being relatively inexpensive, simple in their use and essentially providing 24/7 monitoring.

As an original idea to produce piezochromic sensors of acceptable characteristics for industry, this current work aims at developing and assessing the viability of a novel type of piezochromic coating made up of a polymer matrix hosting molecules with known piezo-responsive properties : spin crossover (SCO) compounds.

5.1 Current technologies → piezochromic materials

The reason behind the lack of adoption of piezochromic technologies lies mainly in the fact that most compounds stand in one of two categories : unconditionally **reversible compounds** and **irreversible compounds**.

For **reversible piezochromic compounds**, the colour change disappears directly after the constraint is removed. The reversibility of the colour change is then completely unavoidable. There exists a variety of compounds which exhibit these properties. Certain polymers fit into this category. As an example, a piezochromic cholesteric elastomer is displayed on Figure 2. The advantage of this compound is that it is very sensitive to pressure,

already switching colour at low overpressures (starting at 0.4 bar). [4] A vast number of inorganic solids have also been studied, such as $MnPS_3$, as depicted on Figure 3. These compounds usually respond to higher pressures. [5] Since the information is not stored in the compound after removal of the constraint, this category cannot be classified as "Smart" materials and is heavily restricted in terms of practical applications.

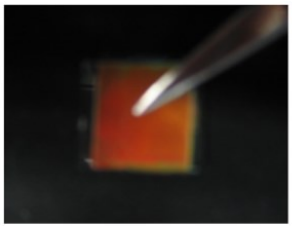

Figure 2 Pressure induced change from red to green for a cholesteric elastomer [4]

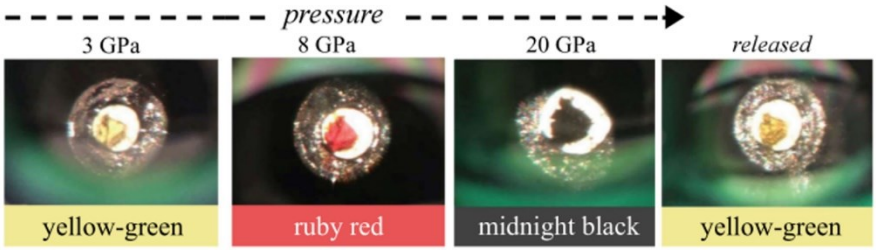

Figure 3 Pressure induced color change of $MnPS_3$ [5]

The other category encompasses **irreversible piezochromic compounds**, for which, once a certain threshold is reached, the change of colour is irreversible even after the return to atmospheric pressure. The most studied compounds of this substance class are inorganic oxides, where the piezochromic change is triggered by a first-order transition between different lattice structures. Here, a particular family has been mostly studied : $AMoO_4$ (A = Co,Cu) molybdates. The most promising compounds are $CoMoO_4$ and $CuMo_{0.9}W_{0.1}O_4$, which present a hysteresis loop width that is 500 K wide (between 400 and -100 °C) and 100 K wide (between 100 and 0 °C), respectively. So, they present a bistability at room temperature, which makes the storage of information about shocks and impacts felt by the material possible. The obvious drawback of these compounds is that after the switch, the material is "spent" and cannot be reused. Indeed, researchers have demonstrated (on Figure 4) that the low-pressure phase is only about 60% recoverable after a complete change of colour, and that is after numerous severe thermal treatments (5 treatments of 5 minutes at 130 °C). [6] The limited reversibility, as well as the extreme conditions required to achieve it, clearly illustrate the limitations of possible applications for these compounds. [7,8]

There is thus a need for a new generation of piezochromic bistable **and** reversible materials to be proposed.

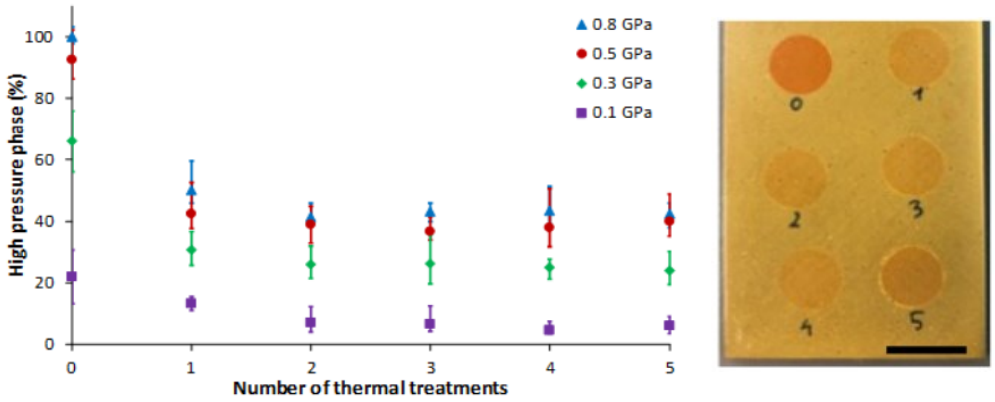

Figure 4 Demonstration of the incomplete reversibility of $CuMo_{0,9}W_{0,1}O_4$ piezochromic properties. After 5 thermal treatments at 130 °C (5 minutes), only 60% of the material reverted to its original state. [6]

5.2 Introduction to spin crossover complexes

To overcome the current limitations in piezochromic technologies described above, the following work proposes the use of spin crossover (SCO) complexes as piezo-responsive compounds. As a short introduction, SCO complexes (Figure 5) are transition metal (usually Fe^{II}) complexes which can present in two or more different electronic states, depending on the thermodynamical conditions. In certain cases, several of these electronic states can be stable for the same conditions, and the actual state will be determined by the previous conditions of the system (memory effect, required for most practical applications). [9]

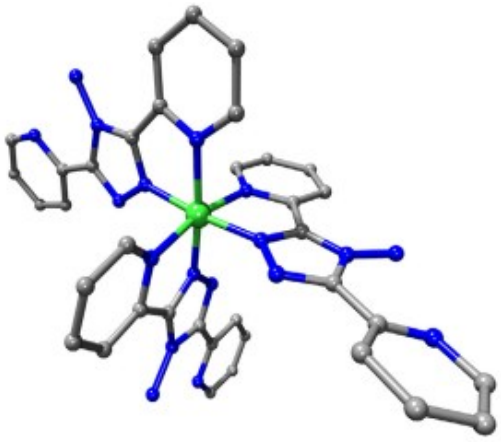

Figure 5 Example of SCO compound. Fe^{II} coordination complex (Fe = green, N = blue, C = grey) [9]

Due to their interesting characteristics, they could combine the advantages of both reversible and irreversible categories of piezochromic compounds previously presented. An example, represented on Figure 6, allows to understand how these compounds can meet the requirements for piezochromic technologies. We see that, for a target temperature (eg: T_{eq}), if it is reached from higher temperatures, we obtain the stable A state. If it is reached by heating from low temperatures, we obtain the B state. This allows the storage of information.

For example, if the system is initially at T_{eq} in the B state and later it is observed in the A state, it must have been heated up at some point, and that information is retained in the compound. Such a system allows to write binary information.

SCO compounds respond to pressure in a similar way. This means that the thermal stability of both the A and B states in a certain temperature region allows for a pressure-induced A↔B switch to remain stable within that region. Thus, they can also be used as shock detection devices with information storage, just as the molybdates. [10]

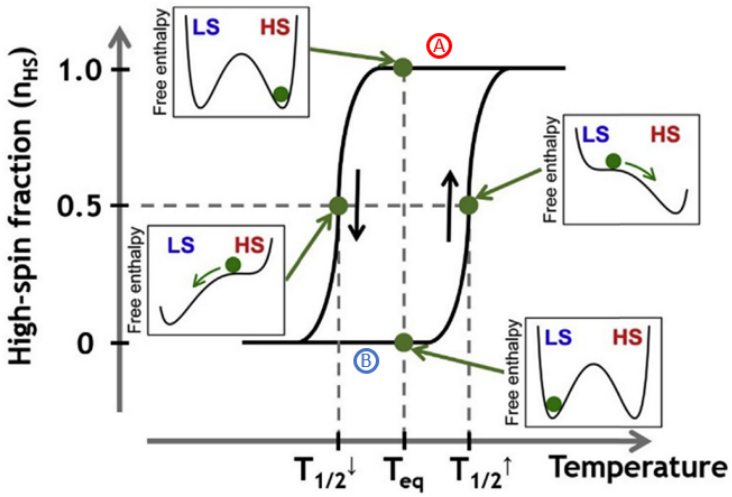

Figure 6 Example of the magnetic properties of a cooperative SCO compound based on the temperature. [10]

However, their properties differ from the molybdate family in that they are usually completely reversible (the switch from the two states can be done an infinite amount of time without fatigue or degradation of the material) using another stimulus (e.g. heat after a pressure stimulus). In that way, they also benefit from the properties of the first class of piezochromic compounds, although their reversibility is no longer unavoidable but rather conditional on a stimulus. This property allows for the control of the state reversal, which does not occur directly after removal of pressure like the first class of piezochromic compounds. Therefore, they have been recognized as having tremendous potential not only in the field of piezochromism, but also thermochromism and information storage technologies (molecular storage devices with very high information density).[11–13]

The piezochromic properties of SCO compounds have been studied [14–18], but their application has, to the best of my knowledge, never been implemented in a piezochromic device. This current work is an attempt at bringing such a technology to life via the development of piezochromic SCO-polymer hybrid coatings, as well as displaying the possibilities that they could bring for the prediction of applied pressures. In addition, this work aims at providing multiple spin state detection possibilities for these coatings, such as the classical optical (color change) detection as well an attempt at providing "piezofluorescent" properties to these coatings.

But before diving into the purpose of this work, it is important to provide the necessary background on the SCO phenomenon and SCO complexes, as well as on the current state of the research that is critical for the purpose of this work.

6. Spin crossover phenomenon

Spin crossover is a thermodynamical phenomenon driven by entropy, through which certain coordinated metals (from d^4 to d^7) can exist in different 3d-electronic configurations, namely high-spin (HS) and low-spin (LS) states (for some transition metals, an intermediate spin state (IS) is also possible) (see Figure 7). [19] To understand this concept further, it is necessary understand the concept of field splitting from both crystal field theory (CFT) and ligand field theory (LFT). An introduction to CFT and LFT can be found in Annex 17.1 and 17.2, for reference.

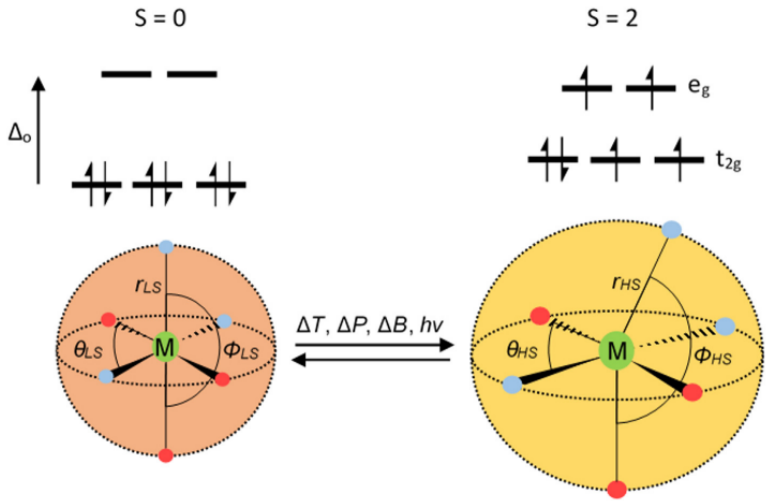

Figure 7 High and low spin representations of a d^6 metal [21]

6.1 Spin crossover

The understanding of the field splitting from crystal and ligand field theory allows to comprehend the SCO mechanism. Two electrons require a certain amount of energy to be paired into the same orbital, called the pairing energy **Π**, due to the electrostatic repulsion that is felt between them. So, orbitals of the same energy are usually all half-filled first. Then if some electrons are still leftover, the orbitals will be completely filled. In the general case, this is the situation which minimises the system's energy, and is called Hund's rule.

The situation is a little bit more complicated for SCO complexes, since the 3d orbitals are split into e_g and t_{2g} valence orbitals and do not have the same energy, and the pairing energy **Π** competes with the field splitting Δ_o.

As mentioned previously, certain metal complexes (with configurations from d^4 to d^7) can be in the LS state, where the electrons prioritize filling the lower energy t_{2g} orbitals, or in the HS state where filling all e_g and t_{2g} orbitals with electrons of parallel spin is prioritized, in accordance with Hund's rule for the filling of orbitals.

The HS case is encountered when the field splitting value is low, which we call a "weak field" situation. In this configuration, the splitting Δ_o is smaller than the electron pairing energy **Π**, thus electrons are energetically inclined to reach the highly stable half-filled orbital configuration. In other words, it will cost less energy to the electron to switch to the higher energy orbital e_g than to pair itself with another electron in a t_{2g} orbital. The LS case is encountered when the field splitting value is higher than the electron pairing energy, which we call a "strong field" situation. In this configuration, the high splitting Δ_o renders the half-filled configuration energetically unfavourable. The state of lowest energy is then the complete filling of the t_{2g} orbitals, bypassing Hund's rule. [20] An example of both states for a d^6 metal (e.g. Fe^{II}) is represented on Figure 7. [21]

The field splitting value is generally expressed by the following expression:

$$\Delta_o = 10Dq(d) \approx \frac{\mu}{d^6} \quad (1)$$

For a neutral ligand, where μ is the dipole moment of the ligand and *d* is the metal-ligand distance. [22] Along with the formula of CFT (Annex 17.1), this demonstrates that Δ_o has a 5-6th power dependence on the metal-ligand distance R. Indeed, ab initio DFT+U calculations showed a good accordance with this theory for a range of R (-2.5 to 5 % displacement relative to the original bond length), as can be seen on Figure 8.

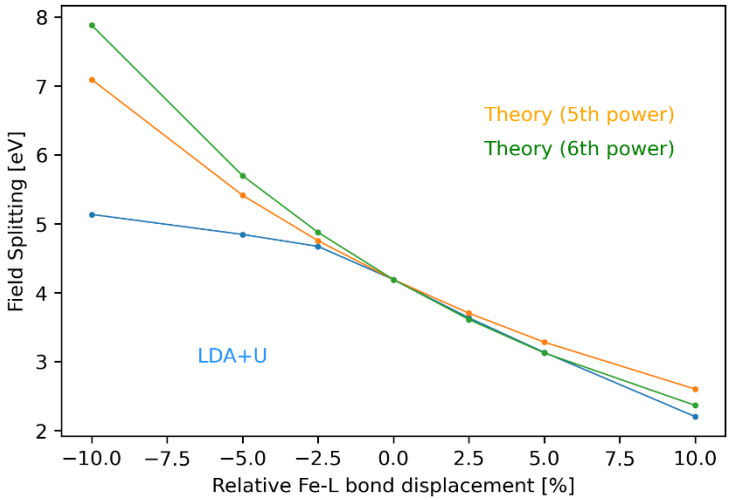

Figure 8 DFT+U calculations with the LDA functional (blue), CFT expression (5th power) and LFT expression (6th power) for Δ_o for a Fe^{II} octahedral complex.

However, the existence of a HS and LS state does not guarantee the possibility of a spin transition to occur. Generally, it is considered that if the ligand field splitting value is <

11000 cm^{-1} (1.36 eV), then Hund's rule will always be followed (field splitting $\Delta_o <$ pairing energy $\mathbf{\Pi}$) and the compound will remain in HS independently of the thermodynamical conditions (T, P). If the ligand field splitting is $> 21500\ cm^{-1}$ (2.67 eV), then the field splitting will always be stronger than the pairing energy ($\Delta_o > \mathbf{\Pi}$), and the compound will remain in the LS state. [22]

In SCO compounds, the metal-ligand distance varies from the LS to the HS state, which is partially responsible for a change in the field splitting value, according to Eq.(1) and Figure 8. The range of values where SCO is possible is $\Delta_{o\,\boldsymbol{HS}} \approx 11500 - 12500\ cm^{-1}$ for the splitting in the HS state, and $\Delta_{o\,\boldsymbol{LS}} \approx 19000 - 21000\ cm^{-1}$ in the LS state. [22] These values represent a very short range of energies. The fact that the energy range required to have a SCO is so narrow means that a small modification in a compound's environment (ligand, anion, non-coordinated solvent, synthesis method…) can drastically change its SCO properties. This is also the reason why the SCO phenomenon is attainable using thermal energy. For this reason, it is generally very difficult to predict whether or not a compound will present a SCO, or how it will behave in a specific matrix.

6.2 Consequences of SCO

It is evident that depending on the spin state, the magnetism of the complex is modified. Indeed, on the example above (Figure 7, for Fe^{II}), in the LS state, all the electrons are paired in the t_{2g} orbitals, which amounts to a total spin value $S_{LS} = 0$, so a diamagnetic behaviour is expected. On the other hand, in the HS state, four unpaired electrons are to be accounted for (2 in two t_{2g} orbitals and 2 in the e_g orbitals), so the complex spin is higher $S_{HS} = 2$, from which we can expect a paramagnetic behaviour. This means that measurements of a compound magnetism allow to access information about its spin state, specifically the fraction of HS and LS states. A very common way of studying spin crossover is by measuring their magnetic susceptibility χ and plotting $\chi T \propto T$. As an example, χT for 100% Fe^{II}_{HS} phase is roughly 3.5 $[cm^3.K.mol^{-1}]$ whereas for a 100% Fe^{II}_{LS} phase it is close to 0. For any value in between, the χT can be easily converted into the HS fraction via the following equation:

$$\gamma_{HS} = \frac{\chi - \chi_{LS}}{\chi_{HS} - \chi_{LS}} \qquad (2)$$

As is illustrated on Figure 7, the volume and symmetry of the complex is also affected. Whereas the LS state presents a smaller volume and an octahedral symmetry, the HS state has a higher volume and a slightly distorted octahedral symmetry (due to the Jahn-Teller effect). This is because, as explained by LFT, the e_g^* orbitals are antibonding orbitals, so the bonding between the metal centre and the ligand is weakened in the HS state (where the e_g^* orbitals are occupied), thus the metal-ligand distance is increased. This implies that pressure,

or guest effects (molecules sterically interacting with the complex in a network) can induce a spin crossover by modifying the complex' volume. [15] Indeed, pressure decreases the metal-ligand distance, leading to an increase of the field splitting Δ_o, according to Eq. (1). The pressure dependence of the field splitting can also be described by the following thermodynamical equation:

$$\Delta = \Delta_0 + p\Delta V \quad (3)$$

As the pressure increases, Δ eventually overcomes the electron pairing energy, so all the electron pair up in the t_{2g} orbitals, leading to a LS state. [23] Figure 9 is also a way to understand this: as the pressure increases, the metal-ligand distance decreases, until it is equal to R, at which point the LS state becomes energetically favourable.

Since the distance between the metal centre and the ligand is affected, XRD is a very powerful tool to evaluate the spin state. For example, in the case of Fe^{II} complexes, the distance between the Fe centre and the ligand is about 2.2 Å in the HS state and 2 Å in LS state. It is also a predictive tool: if a Fe^{II} compound has a metal-ligand distance > 2.3 Å, SCO shouldn't be expected, since the field splitting in this situation will be too low.

Another consequence of this change is that the optical properties of the complex are altered. Indeed, the spin transition can be expressed using this equation for a d^6 metal, indicating a change in ground state between the singlet state $^1A_{1g}$ (LS) and quintet state $^5T_{2g}$ (HS):

$$t_{2g}^4 e_g^2 \ (^5T_{2g}) \rightleftharpoons t_{2g}^6 \ (^1A_{1g}) \quad (4)$$

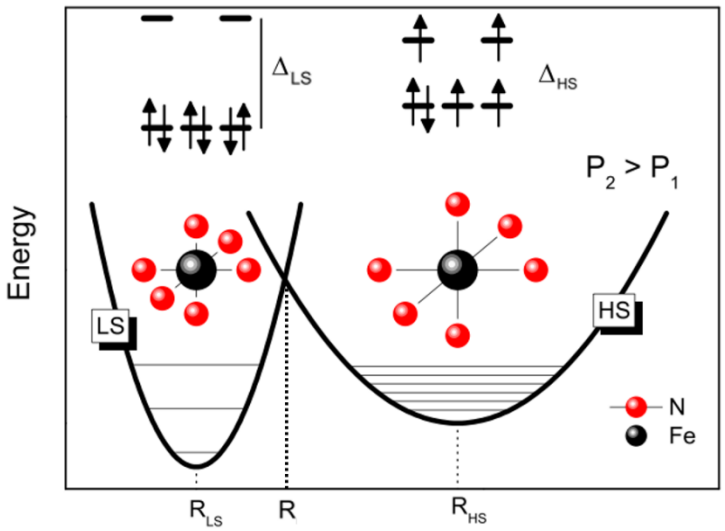

Figure 9 : Energy of a SCO system as a function of Metal-Ligand distance. Increase in metal-ligand distance and decrease of field splitting in HS are also shown [23]

As Figure 9 shows, HS and LS state have different ground states ($^5T_{2g}$ and $^1A_{1g}$) and the possible electronic excitation transitions are also different, as displayed on Figure 10, which shows the absorption spectra of a typical Fe^{II} iron compound. [24] This often results in different optical characteristics in the visible spectrum. For example, a HS Fe^{II} compound is often white whereas a LS one is deep purple. This enables UV/Vis spectroscopy, among other techniques, to map the relative proportions between the two states in a system (at least on the surface). Figure 10 shows that in the HS state the compound absorbs slightly at ~12000 cm^{-1} (830 nm) in the NIR range, while the LS state absorbs at ~18000 cm^{-1} (550 nm) in the visible range. [12]

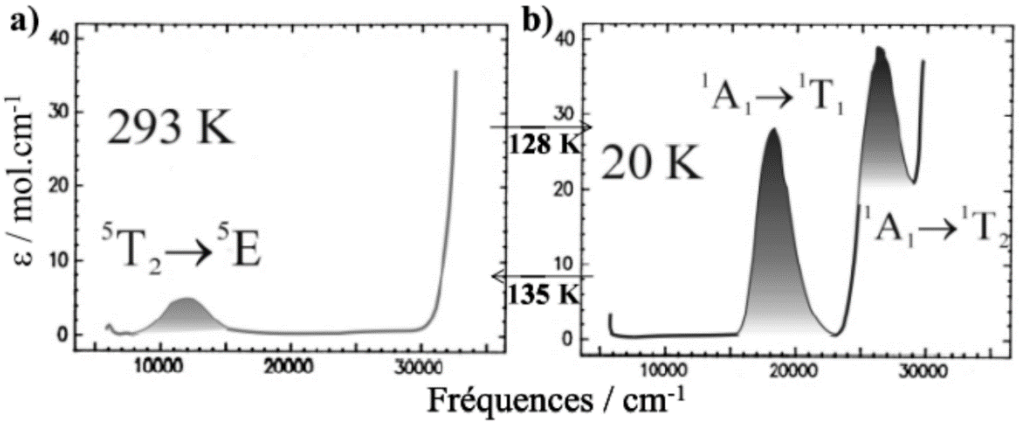

Figure 10 Absorption spectra of a typical Fe^{II} SCO complex in a) the HS state b) LS state [24]

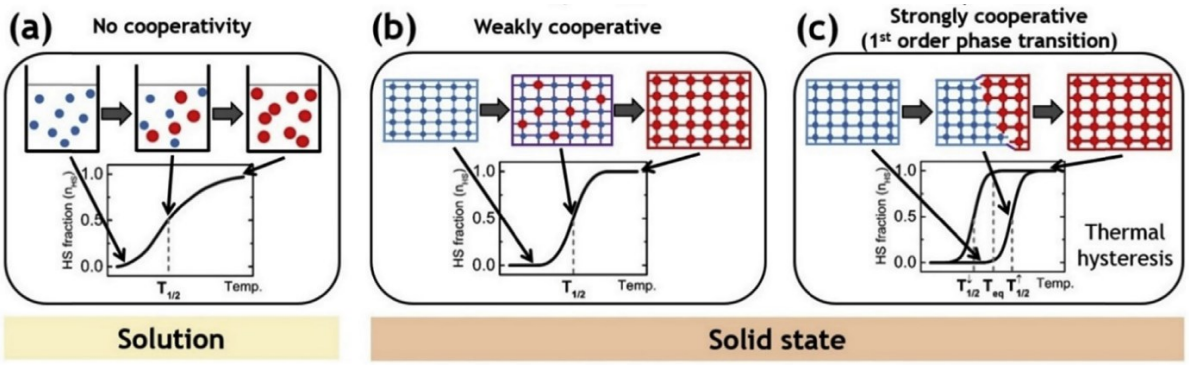

Figure 11 Illustration of the origin and consequence of cooperativity on the memory effect of SCO compounds [10]

As mentioned and depicted on Figure 7, the SCO can be induced by several external stimuli. The spin state is determined by a thermodynamical equilibrium, so a variation of pressure or, much more commonly, temperature can shift that equilibrium, modifying the stable spin state towards one direction. Figure 11 roughly represents the most SCO behaviours versus temperature. The spin state conversion can be quite gradual and proceeds over a broad range of temperatures, such as in Figure 11a. It can also be quite sudden, such as in Figure 11b, in which case we shall refer to it as a spin transition (ST) and we define the temperature at which the transition occurs (more precisely, the temperature at which half of

the active metal centres have switched), $T_{1/2}$. The next case displayed in Figure 11c corresponds to a steep spin transition presenting a temperature range of bistability, where the spin state is determined not only by the thermodynamic parameters (such as temperatures) but also by the previous state of the system (history of the system). [14] This state has already been presented in the introduction on SCO compounds. The result is that at a single temperature, the system can be in a HS or LS state depending on whether the system was heated up or cooled down. On Figure 11c, this is characterized by a hysteresis loop and two transition temperatures are recorded: $T_{1/2}^{\uparrow}$ and $T_{1/2}^{\downarrow}$. Such properties offer many assets in industrial research and therefore many efforts are undertaken to design SCO compounds displaying a memory effect at room temperature with a wide bistability domain. Such properties could be exploited to store information as well as in sensors, to name a few examples. [13] We shall focus on such materials in the frame of this master thesis, in order to propose new materials able to store the information after a pressure impact (of various energies) to detect and prevent accidents, in our daily life.

The factor which will determine a compound's behaviour, gradual, abrupt or with a hysteresis loop, is the compound cooperativity. That is, the magnitude of the interactions between the active metal complexes in a given system. As cooperativity increases, the spin state switch information is transmitted between the complexes, so the transition occurs abruptly throughout the system. This effect has been attributed to the change in volume between HS and LS states, which affects the phonon system of the lattice, driving the cooperative interaction. In other words, cooperativity will be affected by the distance between the metal centres, but also the type and mechanical properties of the ligands for example. With this in mind, major strategies were developed to increase cooperativity in SCO compounds: the first is to add covalent bonds to link metal complexes together, essentially making 1,2 or 3D coordination polymers. These bonds help transmit the spin state switch information between the metal centres. The second is to select ligands which will favour the formation of H bonds, or electrostatic interactions. The third strategy consists in designing for more π-π interactions between aromatic cycles for example, bridging the polymer chains together. The two latest strategies can be combined in a single compound and even be added to the first strategy. [25,26]

Cooperativity is also affected by the number of metal centres. Usually, the smaller the particles the less abrupt the transition will be, and up to now no SCO nanoparticle with high cooperativity has been found. Such a size effect is not to be neglected and represents a challenge for the goal of this work. [22]

6.3 Thermodynamics of SCO systems

Spin crossover is considered an entropy-driven phenomenon. This is because, in a "weak field", HS situation, electrons favour occupying e_g^* orbitals, even if they are of higher energy, because of an entropy gain. In this configuration, this gain is of two origins :

The first is the greater spin and orbital multiplicity engendered by the occupation of more orbitals in the HS state. Indeed, if we look at the Fe^{II} ($3d^6$) example: In the LS state, the electrons only have one spin configuration available, since they are all in the t_{2g} orbitals, which are completely filled (see Figure 7). If we take Boltzmann's entropy definition:

$$S = k_B ln(\Omega) \qquad [J.(K.mol)^{-1}] \tag{5}$$

The total number of configurations is 1, which gives a $S_{LS}^{spin} = Rln(1) = 0$ $[J.(K.mol)^{-1}]$. However, in the HS state, 5 different configurations are available (quintet : $\Omega_{HS} = 2S + 1$; $S = 2$) which gives $S_{HS}^{spin} = Rln(5) = 13{,}38$ $[J.(K.mol)^{-1}]$. Consequently, the spin entropy change during the spin transition is $\Delta S^{spin} = S_{HS}^{spin} - S_{LS}^{spin} = 13.38$ $[J.(K.mol)^{-1}]$. The orbital entropy contribution can also be computed the same way. Once again, the LS state only has one configuration available, which defines its orbital entropy to $S_{LS}^{orb} = Rln(1) = 0$ $[J.(K.mol)^{-1}]$. There are three distinct HS orbital configurations (see Figure 12), returning a $S_{HS}^{orb} = Rln(3) = 9{,}13$ $[J.(K.mol)^{-1}]$. Then, the orbital entropy change is $\Delta S^{orb} = S_{HS}^{orb} - S_{LS}^{orb} = 9{,}13$ $[J.(K.mol)^{-1}]$. This would mean that the total electronic contribution to the entropy change would be 22,52 $[J.(K.mol)^{-1}]$. However, this is rarely the case in practice. In reality, only the spin entropy is considered, $\Delta S_{el} = \Delta S^{spin} + \Delta S^{orb} = \Delta S^{spin} = 13.38$ $[J.(K.mol)^{-1}]$. This is because the orbital component has a non-null value only if the t_{2g} orbitals are degenerated, which is only the case when the octahedral symmetry of the complex is perfect. As mentioned previously, the HS state is most often found with a distorted octahedral symmetry, where the degeneracy of the t_{2g} orbitals is lifted. Then, the electron cannot move freely between these 3 orbitals, and only one configuration is available (*ergo* $S_{HS}^{orb} = Rln(1) = 0$ $[J.(K.mol)^{-1}]$). [5,15,16,17]

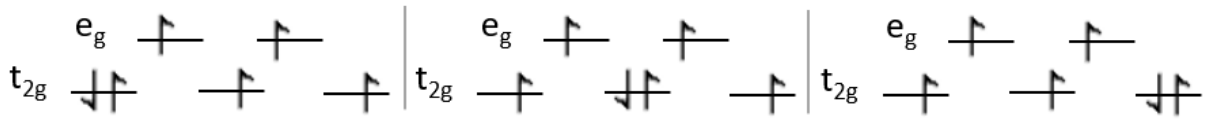

Figure 12 Illustration of the 3 HS ideal orbital configurations for a Fe^{II} complex

The second contribution to entropy is that in the HS state, metal-ligand bonds are "looser" than in the LS state. This means that these bonds are of lower energy. The lower bond strength of the HS state implies a greater vibrational amplitude of the bonds (or a lower vibrational frequency), which explains the resulting increase in entropy ΔS_{vib}^{intra}. In addition,

this change in metal-ligand bond length also induces a change in the neighbouring bonds (H bonds, electrostatic bonds with anion, solvent…), which is accounted for in ΔS_{vib}^{net}.

Since calorimetric measurement on Fe^{II} compounds returns values of $\Delta S_{LS\rightarrow HS}^{tot} \sim 48 - 86\ [J.(K.mol)^{-1}]$, it is deduced that most of the entropy change of SCO comes from the vibrational contributions. (This value also accounts for other phenomenon often coupled to SCO, such as a phase transition). [28,30]

6.4 Thermodynamics of SCO system without interactions

For a diluted system, where the metal centres are spread too far apart to interact, the thermodynamical approach to spin transition can be described using the Gibbs equation, assuming constant pressure:

$$\Delta G = \Delta H - T\Delta S \tag{6}$$

With $\Delta G = G_{HS} - G_{LS}$, $\Delta H = H_{HS} - H_{LS}$, $\Delta S = S_{HS} - S_{LS}$. Since the transition requires to overcome the field splitting, ΔH will always be positive, and ΔS is also always positive, as has already been mentioned previously. So, Eq. (6) tells us that at low temperatures, the spin transition won't be favoured ($\Delta G > 0$) and the stable state is LS while at high temperature the stable state is HS ($\Delta G < 0$). The temperature separating the two regimes is found for $\Delta G = 0$ ($at\ equilibrium$):

$$T_{1/2} = \frac{\Delta H}{\Delta S} \tag{7}$$

When $T > T_{1/2}$, $T\Delta S$ will be bigger than ΔH, which will render the spin crossover energetically favourable. Just like mentioned earlier, this allows to understand that SCO is an entropy driven phenomenon.

6.5 Thermodynamics of SCO system with interactions

When dealing with an interactive system, cooperativity between the metal centres must be considered. Multiple models have attempted to describe this phenomenon. Here, one of the most popular is presented : a modified version of Gibbs equation is used to take the intra- and intermolecular interactions and a cooperativity factor, Γ (which is characterized by a critical value Γ_C), is introduced in the Slichter and Drickamer model: [31]

$$G = (1 - x_{HS})G_{LS} + x_{HS}G_{HS} + \Gamma x_{HS}(1 - x_{HS}) - TS_{mix} \qquad (J.mol^{-1}) \tag{8}$$

With x_{HS}, the fraction of HS complexes in the system, Γ the cooperativity factor ($J.mol^{-1}$) and S_{mix} defined according to Boltzmann statistic (Eq. (5))

In our case:

$$S_{mix} = -R\left(x_{HS}ln(x_{HS}) + (1 - x_{HS})ln(1 - x_{HS})\right) \qquad (J.(K.mol)^{-1}) \qquad (9)$$

This definition allows us to obtain an expression of the HS fraction at equilibrium as a function of the temperature, by deriving the Gibbs free energy with regards to the HS fraction x_{HS} :

At equilibrium, $\frac{\partial G}{\partial x_{HS}} = 0$, which returns:

$$T = \frac{\Delta H + \Gamma(1 - 2x_{HS})}{Rln\left(\frac{1 - x_{HS}}{x_{HS}}\right) + \Delta S} \qquad (10)$$

The result of this equation is found on Figure 13. With a low cooperativity factor, the black line corresponds to a gradual spin crossover ($\Gamma < \Gamma_C$). The red line represents a more cooperative compound ($\Gamma = \Gamma_C$), with an abrupt spin transition. The blue line represents a very cooperative compound, with the appearance of a hysteretic spin transition ($\Gamma > \Gamma_C$).

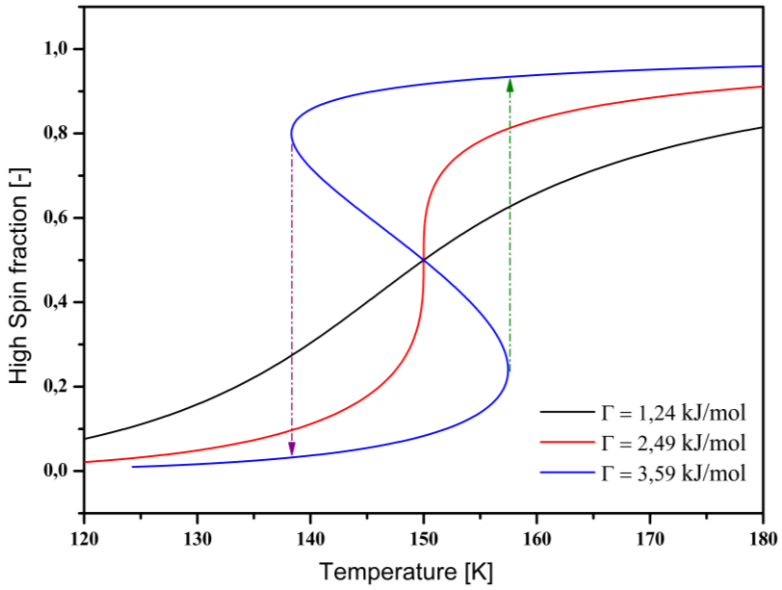

Figure 13 – Spin crossover behaviour predicted by Slichter and Drickamer model. For the blue line, the green and purple arrows show the true path during heating or cooling respectively (from fictitious value of $\Delta H = 7.173 \frac{kJ}{mol}, \Delta S = 47.8 \frac{J}{mol.K}$)

7. State of the art

7.1 SCO research

Spin crossover complexes are found in many different forms. Most of the SCO complexes studied for applications in SCO research are Fe^{II} compounds, due to their generally good cooperative properties, stability, distinct optical properties in HS or LS state and their ease of analysis, with advanced technologies like Mössbauer spectroscopy. But spin crossover is not limited to Fe^{II}. Other research topics include Cr^{II}, Fe^{III}, Co^{II} and Mn^{III} and Mn^{II} compounds.

The research on Fe^{II} compounds is too extensive to be covered entirely in this work. Since the compounds of interest for this work will be talked about in a later section, here we will only describe the broad types of compounds which have been discovered, as well as develop some of the influencing factors of SCO transition.

The first class of compounds that were ever studied are Fe^{II} mononuclear complexes, such as $[Fe^{II}(phen)_2(NCS)_2]$, $[Fe^{II}(2\text{-pic})_3]X_2 \cdot Sol$ (X = Cl, Br, I; Sol = EtOH, MeOH, H_2O, $2H_2O$) or $[Fe(phen)_3]X_2$. These compounds are made up of a single metal ion surrounded by its ligands, and while showing poor cooperativity due to the generally high distance between iron centres, have been very helpful to study the effect of different operational parameters of SCO compounds on their spin state behaviour. Although the effect of the ligand is obvious, it has been demonstrated experimentally by substituting a phenanthroline (phen) ligand with an NCS, lowering the ligand field strength enough to render spin transition possible. [32]

The effect of substituting the metal centre of the compounds has also been explored, by substituting Fe^{II} in $[Fe^{II}(2\text{-pic})_3]Cl_2 \cdot EtOH$ by Zn^{II}, forming $[Fe^{II}_xZn_{1-x}(2\text{-pic})_3]Cl_2 \cdot EtOH$. This resulted in a more gradual transition in the final compound. Again, this can be explained by the dilution of the SCO active metal (Fe^{II}) in the compound reducing the scope of possible cooperative interactions. [30]

By varying the solvent molecules found in $[Fe^{II}(2\text{-pic})_3]Cl_2 \cdot Sol$ (Sol = EtOH, MeOH, H_2O, $2H_2O$), researchers have been able to study the effect of these non-coordinated molecules on the spin transition, for the first time. [33] As can be seen on Figure 14, the nature of this solvent can drastically change the spin state behaviour, even introducing a hysteresis in some case. [22] This is important to keep in mind for the rest of this work since these solvent molecules tend to leave the compound during heating. This could result in a compound which seems promising at first glance, but which in real conditions (solvent free) would actually have less adequate SCO properties. This is the case for $[Fe(L2)_2](BF_4)_2 \cdot 2H_2O$ (Figure 14). Upon first review of the magnetic response of the compound (1 upon heating and 2 upon cooling), one could think that this compound presents bistability between 150 and 300 K (ΔT = 150K,

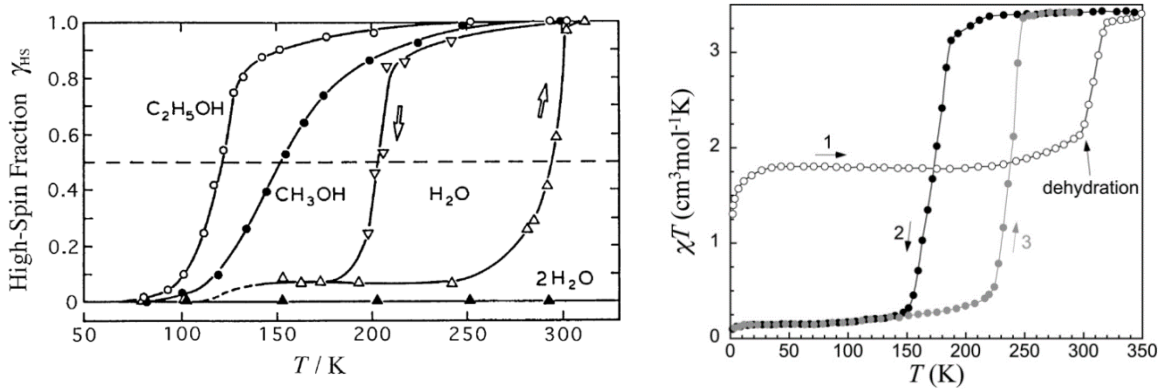

Figure 14 Effect of solvent nature on SCO behaviour in Left : $[Fe^{II}(2\text{-pic})_3]Cl_2 \cdot Sol$ [33] Right : $[Fe(L2)_2](BF_4)_2 \cdot 2H_2O$, L2 = 2,6-bis(5-methyl-1H-pyrazol-3-yl)pyridine [25]

which is enormous). However, upon several heating and cooling cycles, it becomes apparent that the initial behaviour was due to the solvent and that after its departure, the compound retrieved its native properties (3 upon heating and 2 upon cooling), which are much less desirable (ΔT = 50K but not centred on room temperature). [25] This is an effect often disregarded in literature, which exacerbates the need to keep this in mind for the remainder of this work. However, this solvent effect can be beneficial in cases where the compound is able to retain these solvent molecules.

One of the most important influence one can have on the SCO behaviour of a compound is by varying the pressure applied to that compound. Multiple studies have been conducted on the effect of pressure on SCO, with results that are not surprising considering the SCO phenomenon. In 2005, Gütlich *et al.* studied the effect of pressure on multiple compounds, including the previously talked about $[Fe^{II}(phen)_2(NCS)_2]$. Their results are displayed on Figure 15. This figure illustrates that raising the pressure shifts the transition towards higher temperatures. As a reminder, this can be explained by the fact that metal ions in the HS state have a higher volume than in the LS state, and that the field splitting Δ increases with pressure as described by Eq. (3). Since SCO is a phenomenon driven by thermodynamics, it is easy to understand how the lower volume LS state would be favourited over the HS state at high pressures. [34]

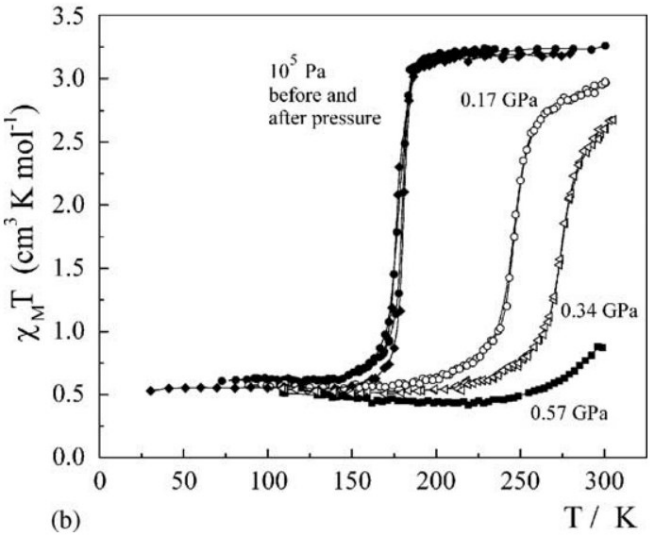

Figure 15 Influence of pressure on SCO behaviour of $[Fe^{II}(phen)_2(NCS)_2]$ [34]

Yet, "external" pressure is not the only way to induce such a constraint on SCO compounds. It is possible to apply "internal" pressure on certain SCO compounds, by choosing non-coordinated anions of high volume, which are still part of the lattice formed by the compound. These anions, confined into the tight lattice, also force the system to favour the LS state. [12,35]

Besides mononuclear compounds, some dinuclear molecules have also been studied. In these compounds, the two iron centres can have different ligand environments, thus behave distinctly, which can result in two-step spin transitions. They can also have the same environment, and even if the two centres are the same, a two-step spin transition is still sometimes possible because there are now 3 distinct possible states (HS-HS, HS-LS and LS-LS) with different stability regions, as can be seen on Figure 16. [36]

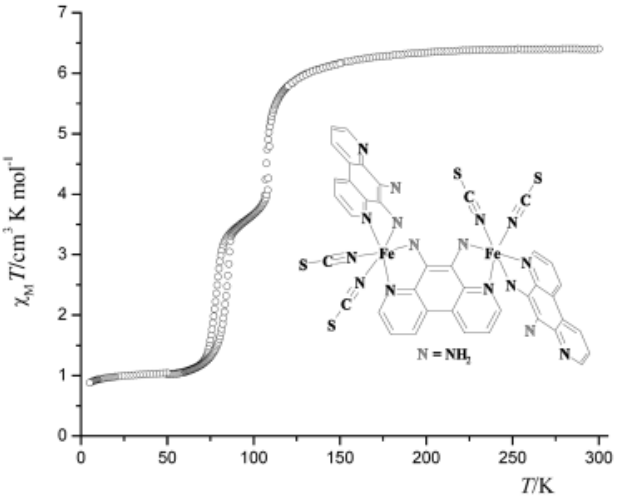

Figure 16 Example of two-step spin transition in a dinuclear complex. Here, the first step presents a hysteresis cycle [36]

With the right multidentate ligands, certain SCO complexes can form coordination polymers, or metal-organic frameworks (MOFs). These polymers can be present in the form of chains (1D), or in the form of 2D or 3D networks. With the recent growing interest of MOFs (metal-organic frameworks), these compounds are being studied more and more. The other reason for their popularity is that they tend to present better SCO properties. Indeed, it has already been mentioned that cooperativity, the feature most important for SCO, is the transmission of the spin state change information through elastic interactions between metal centres (via phonons). For SCO coordination compounds, these elastic interactions can be very effectively transmitted through the ligands that are bridging the metal centres together. As already mentioned, the first role a ligand must fill is to provide the right ligand field strength to render SCO possible. Much remains to be known on this subject, but research already showed that ligand selection for a coordination polymer must also strike a balance between elasticity and rigidity. Indeed, since the information is of a physical nature, if the ligand is too loose, it will tend to buffer the propagation of the information. On the other hand, if the ligand is too rigid, the information will also be poorly transmitted, for the same reason.

Among the 1D coordination chains, one popular family is the 4-R-1,2,4-triazole based Fe^{II} chains, due to their potential in practical applications, because of their tendency to form large hysteresis near or above room temperature. These compounds, of template [Fe(4-R-

1,2,4-triazole)$_3$]A$_2$·Solv vary for each combination of substituent R, anion A and non-coordinated solvent. [37] It is important to mention them since some will be studied and used in this work, namely [Fe(NH$_2$trz)$_3$](NO$_3$)$_{2-x}$(BF$_4$)$_x$, [Fe$_{1-x}$Zn$_x$(NH$_2$trz)$_3$]Cl$_2$, [Fe(NH$_2$trz-)$_3$]Br$_2$·nH$_2$O, and [Fe(Htrz)$_{3-3x}$(NH$_2$trz)$_{3x}$](ClO$_4$)$_2$·nH$_2$O.

Although there are still many other types of SCO compounds from different metal centres (Fe^{III}, Cr^{II}, Mn^{III}, Mn^{II}, Ni^{II}), none of those will be used in the rest of this work. Still, some great reviews exist on these compounds [5,38–44] and a small introduction can be found in Annex 17.3.

7.2 SCO piezochromic compounds and pressure sensors

Before discussing the results of this current work, it is important to describe the current research on piezochromic SCO compounds upon which this work is based. Several research articles have already been published concerning the elaboration of SCO based pressure sensors. This section will review them chronologically.

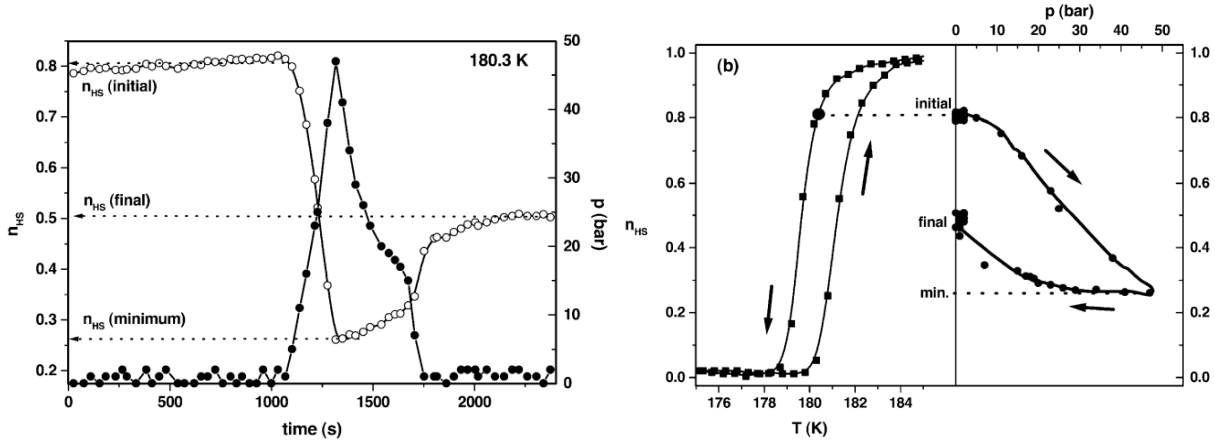

Figure 17 Left: HS fraction of [Fe(phen)$_2$(NCS)$_2$] dependence on time, according to the pressure pulse applied. Right : representation of the pressure cycle applied, with the final HS fraction. A stable switch from HS to LS is apparent [14]

In 2003, an article was published about the compound [Fe(phen)$_2$(NCS)$_2$]. It was the first article to mention the possibility of implementing SCO materials into piezo devices. Indeed, they showed that a high enough pressure (around 5 MPa) applied in a pulse was capable of switching [Fe(phen)$_2$(NCS)$_2$] from the HS state to the LS state. Figure 17 displays this switch, which renders possible the retaining of information about the pressure event. This article did not involve any impact pressure and was realised at low temperature (180 K), but it is considered as the first step in developing this technology. [14]

The idea of using SCO pressure sensors in some form of paint or film was introduced in a 2012 concept paper about temperature and pressure sensors by Garcia, Codjovi and Linares, and once again in 2015. However, the discussion was limited to measuring static pressure. [16,17]

In 2015, the compound $[Fe(hyetrz)_3]I_2 \cdot H_2O$ (hyetrz = 4-(2'-hydroxyethyl)-1,2,4-triazole, H_2O non-coordinated inside the lattice) was synthesized and used as a contact pressure sensor. The detection of the pressure change was made through the optical properties of the compound (switch from white to purple upon contact pressure). For this to be effective, the compound must present bistability of HS and LS state at the operating temperature (most often room temperature), and the hysteresis width must be as large as possible in order to avoid loss of information through thermal variations. This allows the spin state switching induced by pressure to remain stable after the release of said pressure. Researchers confirmed that $[Fe(hyetrz)_3]I_2 \cdot H_2O$ presents these characteristics, through optical reflectivity and DSC measurements. [17]

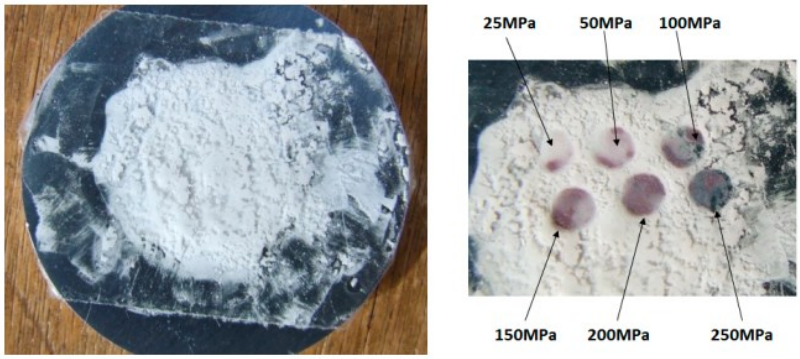

Figure 18 $[Fe(hyetrz)_3]I_2 \cdot H_2O$ powder sample subjected to different pressures [17]

Researchers showed that warming the powder to 303 K reliably caused the powder to switch back to the HS state (white colour), which is an important step in demonstrating the **conditional** reversibility, and thus the reusability of this technology. [17]

As seen on Figure 18, different pressure intensities were applied on the material, to varying results. Generally, the higher the pressure, the more intense the colour change appeared. This hints at the fact that through the colour change, the pressure applied could be quantified. However, it should also be noted that the pressures that needed to be applied to obtain a response from the compound are substantial, in the range of tens or hundreds of megapascals. The threshold pressure for irreversible HS → LS transition was determined to be 30 MPa. While it should be different for different compounds, we can expect compounds from the triazole family to be in the same range of values. [17]

This article represents the first proof of concept of the technology. The use of a triazole iron compound is to be highlighted, as it is a very popular family and the inspiration for some of the compounds which are tested in this work. However, tests were constrained to the compound powder.

The last step of research was published in 2018, where the same compound with an non-coordinated ethanol molecule, $[Fe(hyetrz)_3]I_2 \cdot 0.5EtOH$, was used as a sensor. This compound presented even better characteristics, with a wider hysteresis loop, better centred on room temperature (20-25 °C), as seen on Figure 19. [15]

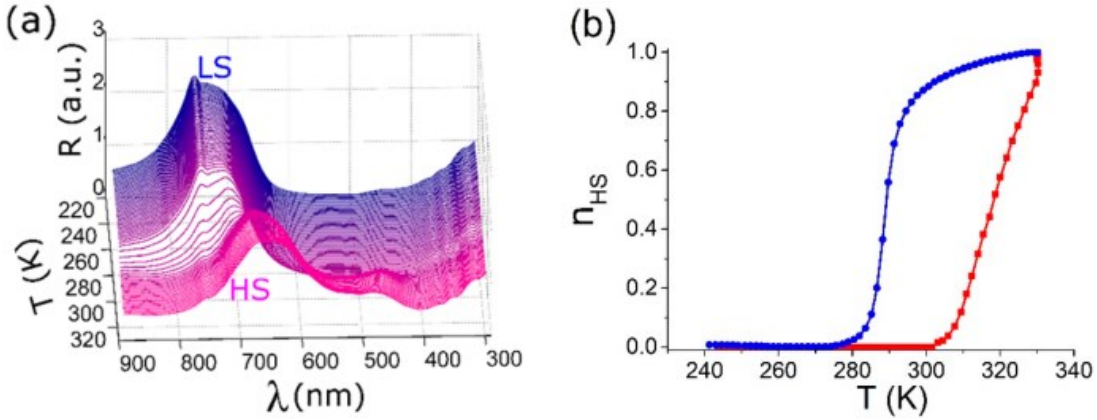

Figure 19 a) Absorption spectra of $[Fe(hyetrz)_3]I_2 \cdot 0.5EtOH$ according to the temperature b) HS fraction of $[Fe(hyetrz)_3]I_2 \cdot 0.5EtOH$ according to the temperature, obtained via integration of the spectra on a) [15]

The novelty that this article brings is the use of a UV/Vis spectrophotometer to measure the absorption intensity of the impacted material, in order to fit a model describing the absorption intensity based on impact pressure. Also, a simple RGB test, which can be done on any smartphone, was conducted to see if it would be possible to infer the impact pressure from simpler measurements. The results from both the absorption and RGB measurements are displayed on Figure 20. Both measurements are somewhat in accordance and show that it is indeed possible to deduce the impact intensity from optical measurements of the material. [15]

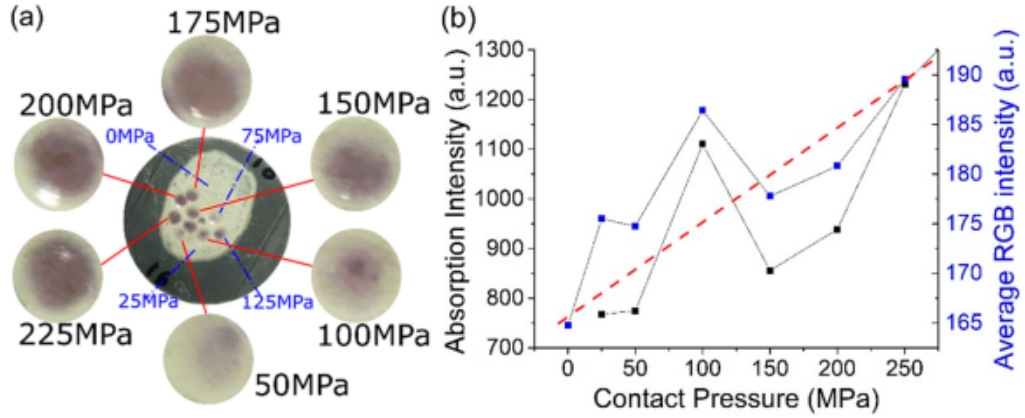

Figure 20 , a) $[Fe(hyetrz)_3]I_2 \cdot 0.5EtOH$ powder sample subjected to different pressures b) dependence of absorption and RGB intensity on the applied contact pressure [15]

However, the relationship between pressure and absorption/RGB intensity is far from ideally linear. The next approach of researchers was to isolate certain peaks of absorption spectrum to see if some permitted a better prediction. Indeed, Figure 21a shows peak number 4 as a prime candidate, which is confirmed by the much better linear relationship on Figure 21b.

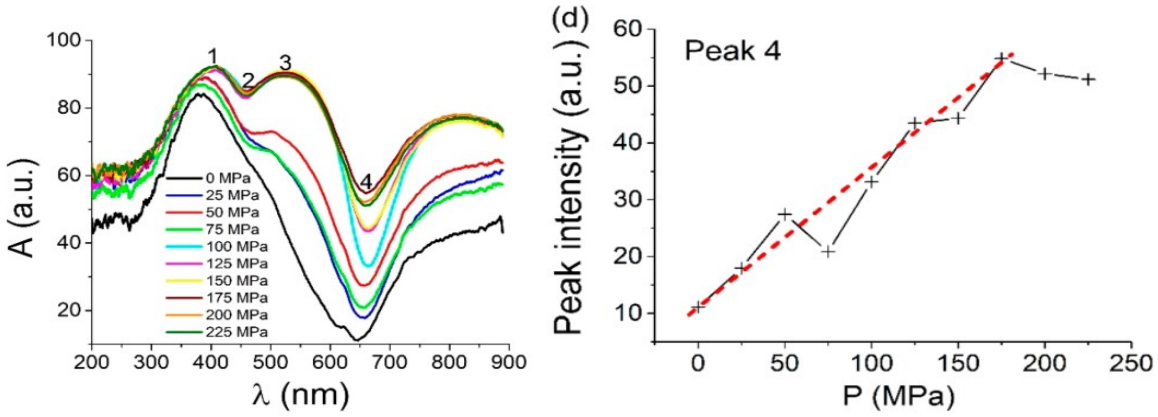

Figure 21 a) Full absorption spectra of [Fe(hyetrz)$_3$]I$_2$·0.5EtOH depending on contact pressure applied b) dependence on absorption at ~650 nm on contact pressure applied, chosen for its linearity [15]

This article also highlighted the importance of two parameters, gathered into a single term, $\frac{\Delta V}{\Delta S}$, ΔV being the unit cell volume change between the HS and LS state and ΔS the entropy variation as defined previously. This term appears in the Clapeyron equation :

$$\frac{dP_{HS\rightarrow LS}}{dT} = \frac{\Delta S_{HS\rightarrow LS}}{\Delta V_{HS\rightarrow LS}} \tag{11}$$

Which can be solved using the atmospheric pressure as reference :

$$T_{HS\rightarrow LS}(P) = T_{HS\rightarrow LS}(P_{atm}) - (P - P_{atm})\frac{\Delta V_{HS\rightarrow LS}}{\Delta S_{HS\rightarrow LS}} \tag{12}$$

And gives us the shift in the HS → LS transition temperature. This equation allows to theoretically determine the threshold pressure at room temperature mentioned previously P_{thr}, for which $T_{HS\rightarrow LS}$ is shifted all the way to room temperature. This represents the minimum pressure required to begin shifting the metal centres from the HS state to the LS state :

$$P_{thr} = P_{atm} + \frac{T_{ambient} - T_{HS\rightarrow LS}(P_{atm})}{\frac{\Delta V_{HS\rightarrow LS}}{\Delta S_{HS\rightarrow LS}}} \tag{13}$$

According to this equation, as $\Delta V_{HS\rightarrow LS}$ increases, the threshold pressure decreases, which is logical considering the previously talked about points on the field splitting. However, the effect is opposite for $\Delta S_{HS\rightarrow LS}$. This is to be expected, as an entropy decrease is unfavourable, and thus would require more energy to counteract. This threshold pressure is generally found around the MPa range. [15] For practical use in pressure sensing, the ideal

value should be intermediate. A too low threshold pressure would make it difficult to discriminate between low and high energy impacts, while a too high pressure would lack sensibility.

The ultimate contribution of all this research is that it opens the possibility for the elaboration of paints and varnishes which would hopefully retain the interesting properties of the SCO compound. Current research highlights the potential of SCO compounds in sensors technology, specifically the Fe^{II} triazole family for pressure sensing. It also shows that development of such technology not only represents a challenge into the synthesis of hybrid SCO-polymer compounds, but also development opportunities for predictive models of impact pressure.

8. Overview of the work

With all the required theoretical background presented, the substance of this current work, which is found in the following sections, deserves an introduction.

For the development of a SCO hybrid coating, there are obviously two principal components : the matrix used to disperse the SCO compounds and the SCO compounds themselves.

The first component discussed is the matrix. The matrix chosen in this work is a waterborne polyurethane dispersion (WBPU). The next sections highlight the motivations for this choice, the synthesis methods used as well as the characterization of the polymer, in order to compare it with the hybrid coating. Then, the axioms for the selection of the SCO compounds for tests are proposed, as well as a presentation and characterization of the two compounds ($[Fe(NH_2trz)_3]Br_2 \cdot nH_2O$ and Fe(pyrazine)$[Fe(CN)_5NO]$) which were selected for this work. The logical thread of this work then continues with the presentation of the two hybrid coatings obtained by combining matrices and SCO compounds with an attempt at understanding the interactions that appear between the two components.

Then, this work remains focussed on these hybrid coatings but takes another direction. Indeed, the technology imagined in this work has clear practical applications. With this in mind, a demonstration of the possibilities as “proof-of-concept” seemed appropriate. Here, attempts were made at developing both impact detection and pressure prediction models through these hybrid coatings, via the use of machine learning algorithms.

Finally, the last section describes an attempt at going beyond the scope of piezochromism by providing another piezo response than colour. Because of past success in recent articles as well as desire from industry, coupling SCO and fluorescence to obtain “piezofluorescent” coatings was attempted. [45–47]

9. Polyurethane polymer

9.1 Polymer matrix choice

One of the most versatile and widely used polymer in current coating technologies are polyurethanes (PU) due to their superior toughness, flexibility at low temperatures, abrasion resistance and ease of use. [48] For example, they constitute the topcoats for most airplane surface materials (see Figure 22). [49] Also, to the best of my knowledge almost no published research ever attempted to combine polyurethanes with SCO compounds, bar one single research paper using a commercial variant : polyurethane D6, although it was used in a hydrogel form and not as a dry coating. [50]

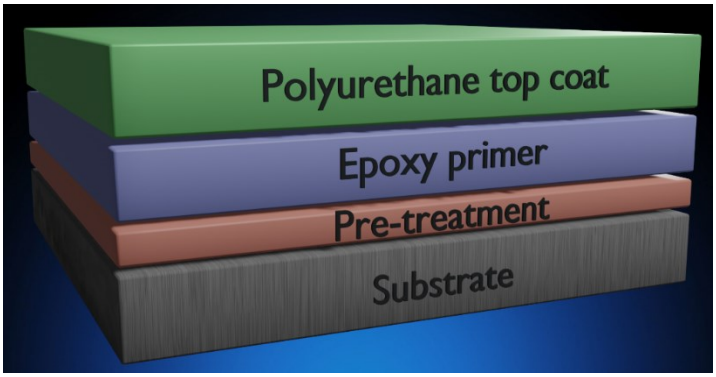

Figure 22 General depiction of the treatments and coatings applied to an aviation-grade aluminium

With this in mind, and since current research does not permit to predict a SCO compound behaviour in a matrix, it was decided to choose a polyurethane polymer as matrix for the hybrid coating material.

Historically, polyurethane coatings have been composed of organic solvent-based systems, which have many drawbacks, mostly due to their negative ecological and health impacts. [51] Nowadays, desire for more ecologically conscious products and the emergence of more stringent regulations from regulatory bodies pushed research to focus on finding water-based solution which would have the same or better properties than older systems. [52–54]

Generally, the simplest polyurethanes can be synthesized by reacting a diisocyanate with a polyol. For coating technologies, polyurethane dispersions (PUDs, in organic solvent or water) are used. PUDs are colloidal suspensions where interfacial forces are paramount in explaining the final properties of the coating, so the suspensions must be stable. Generally, PUDs polyurethane colloids are composed of hard and soft segments, respectively made up of the diisocyanate and the polyol, which both form distinct microphases due to immiscibility between the segments. [52] Additionally, to increase the polymer chain length, as well as to produce the hard segments,

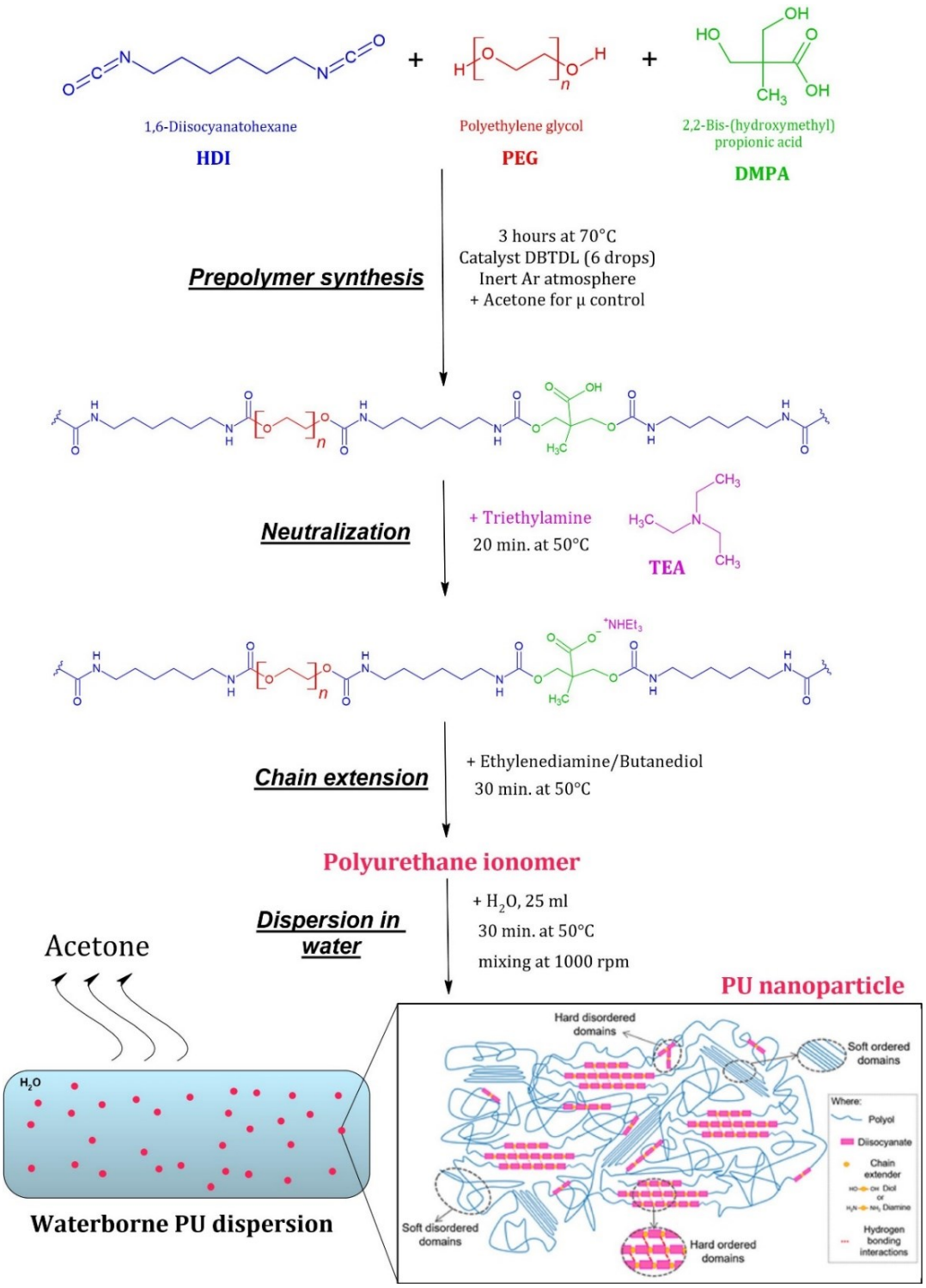

Figure 23 WBPU reaction pathway used in this work and representation of the Hard and Soft segment microphases found in polyurethane colloidal particles [54]

a chain extension step using either a low MW diol or diamine is done. The general synthesis involves the reaction of the diisocyanate with the polyol and the internal surfactant, a chain extension (partial or total), and dispersion in solvent step. Water-based (WBPU) solutions

require further tinkering to be viable. In order for the polyurethane particles to be stable in water, it is modified by the addition of ions (called internal emulsifiers) into both the hard and soft segments, producing ionomers. Non-ionic emulsifiers also exist but are much less common. To obtain better coating properties, it is better that the overall polyurethane chains remain neutral. For this reason, an additional step is used to neutralize (entirely or partially) the internal emulsifier. An illustrative scheme can be found on Figure 23 which gives an overview of the reaction pathway as well as of the typical structures found in PU. The coatings are then produced by subsequent casting of the liquid polymer and drying via evaporation under normal conditions or in an oven/vacuum to improve the process. [55]

9.2 Polymer synthesis

The WBPU used in this work was synthesized via the "acetone process". The general idea is that the synthesis is done using acetone as a solvent which allows to reduce the viscosity of the reaction medium, so as to conserve good polymerization kinetics. The acetone is then removed via an additional step, rotary evaporation, in the later stages of the synthesis, and only water is left as solvent. The precise process that was used in this work is described on Figure 23. This process has the advantage of being healthier and more ecologically friendly than the classical process, which involves organic solvents that are not removed, and are inhaled by workers applying and working around these paints. [56]

As 'hard segment' or diisocyanate, aliphatic diisocyanates were chosen based on their lesser tendency to turn yellow and degrade under UV light compared with aromatic diisocyanates. Moreover, aliphatic diisocyanates have been documented as being the main diisocyanates used in paints and surface coatings for their overall performance. [57] Thus, both Hexamethylene diisocyanate (HDI) and Isophorone diisocyanate (IPDI) have been tested as they have been reported to produce different mechanical properties. Indeed, linear aliphatic diisocyanates (HDI) have been reported to produce softer and more flexible coatings, while cycloaliphatic diisocyanates (IPDI) provide tensile strength and rigidity. [58–60] For 'soft segment' (SS), Polyethylene glycol (PEG) of molecular weight 1450 g/mol or 600 g/mol were used. Dimethylol propionic acid (DMPA), was initially used as internal emulsifier, and triethylamine (TEA) was subsequently used to neutralize the DMPA, as they are the two most commonly used internal emulsifier and neutralizer respectively. [61] As chain extender, ethylene diamine (EDA) was initially used, although butanediol (BDL) was ultimately chosen for reasons that will be explained later in this work.

For the synthesis of WBPUs, a wide range of factors such as the molecular weight of the segments (especially the polymeric soft segment polyol), chemical structure, the hard/soft segment ratio (NCO/OH), hard segment/internal emulsifier ratio (NCO/COOH), the degree of neutralization (%) and chain extension (%) all have a deep impact on the final properties,

which can range from sturdy elastic coatings to soft sticky adhesives. [62] This makes their use in this work tricky since their formulation heavily impacts their final properties, there are almost as many formulations as there are research articles about them, and the best formulations are essentially trade secrets. [63]

Therefore, a single formulation was not immediately selected, and several formulations were tested. Without getting too ahead of myself, the eighth polymer (**D8**) synthesized was the first to produce coatings with good performances that allowed to observe the piezochromic effect of a SCO compound. The composition of this WBPU as well as other performant polymers discussed in this work can be found in Table 1, for which the synthesis method is described on Figure 23:

Table 1 Chemical composition of different synthesized WBPUs

N°	SS	HS	Chain extender	NCO/OH (molar ratio)	NCO/COOH (molar ratio)	Neutralization (%)	Chain extension (%)	Water content (%w/w)
D8	PEG (1450 g/mol)	HDI	EDA	1.8	3.5	100 (TEA)	90	60
D9	PEG (1450 g/mol)	HDI	EDA	1.8	3.5	100 (TEA)	90	60
D11	PEG (1450 g/mol)	HDI	EDA	2.2	3.5	100 (TEA)	90	65
D13	PEG (1450 g/mol)	HDI	BDL	2.1	4.1	90 (TEA)	90	70
D14	PEG (1450 g/mol)	HDI	BDL	1.8	3.5	100 (NaOH)	100	70
D15	PEG (600 g/mol)	IPDI	BDL	1.8	4	100 (TEA)	100	60

9.3 Polymer characterization

FTIR measurements on the synthesized coatings have been realized and are displayed on Figure 25. The most notable peaks that can be pointed out are at ~3300 cm^{-1} corresponding to the stretching mode of N-H bonds, ~2880 cm^{-1} to the stretching mode of C-H (and OC-H) bonds and at ~1710 cm^{-1} for C=O stretching (of carbamates and carboxylic functions). The intense peak around ~1100 and 1240 cm^{-1} are believed to originate from C-O-C stretching modes of the ether oxygen of the soft segment. [64,65] An important thing to note is the absence of the characteristic isocyanate (NCO) peak at ~2270 cm^{-1}, which indicates

that all the diisocyanate molecules have reacted completely. [64] **D15** presents the same peaks but with different intensities because it differs in its PEG bond length (600g/mol). [65] For the coatings tested, two of them (**D9** and **D11**) present additional peaks at ~600 and ~750 cm^{-1}, which are attributed to impurities introduced in the polyurethane from a previous PU batch made from the same glassware. The same impurities responsible for these additional peaks are also thought to be responsible for the yellowish colour of D9 and D11. [66,67]

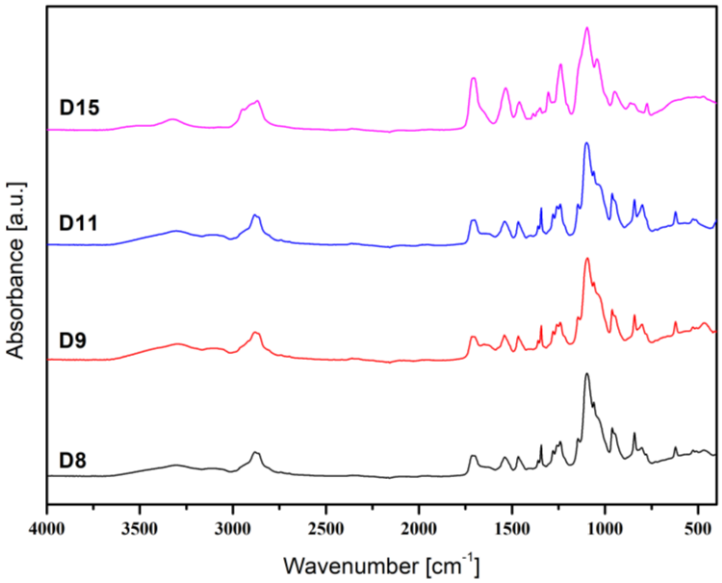

Figure 25 Normalized FTIR spectra for different synthesized PU

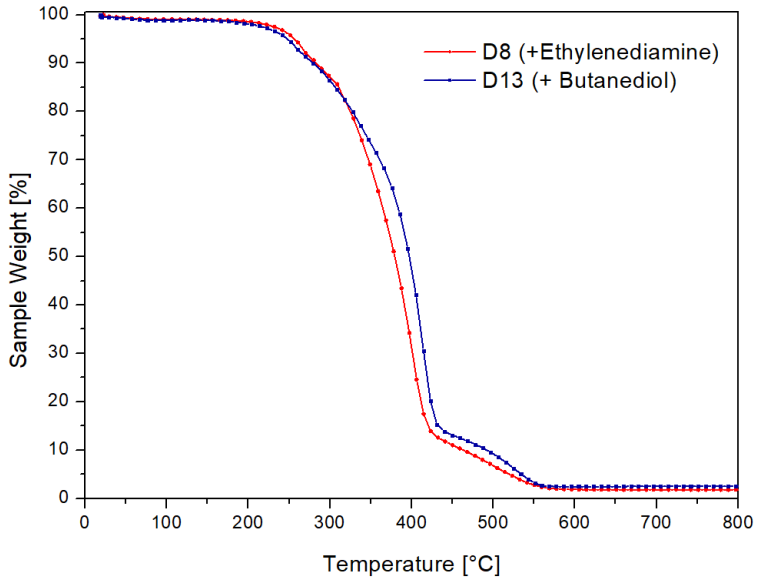

Figure 24 TGA curves of different PU, under Air atmosphere (100ml/min) at a rate of 10°C/min

To further confirm the obtention of a polymer of acceptable performances, TGA analyses of both the ethylenediamine- (**D8**) and butanediol-extended (**D13**) polymers were conducted. Both samples were heated to 800°C from room temperature at a rate of 10°C/min under air flux. As you can see on Figure 24, the experiment demonstrates the thermal stability of both polymers, with respective onset degradation temperatures $T_{d,onset}$ = 213 °C for both polymers, which is identified as the degradation of the hard segments. The temperature of half decomposition $T_{d,1/2}$ = 388 and 405 °C respectively for the ethylenediamine- and butanediol-extended polymers, while their temperature of maximal degradation is $T_{d,max}$ = 577 and 566 °C. These values are very much in accordance with the literature on waterborne polyurethane and are suitable for practical application. [48,68–72]

DSC analysis of the butanediol-extended (**D13**) polymer was carried out (for reasons which will become apparent later). The calorimetric data from -50 to 80 °C indicates a highly endothermic peak at 35 °C, with a $\Delta H_m^{ss} = 68.78\, J.g^{-1}$ (Figure 26). Due to the concordance with the literature on PEGs with similar molecular weight and for reasons which will be explained further on, this has been identified as the melting temperature of the soft segments of the polyurethane. [73,74] This heat of enthalpy value is not unexpected, but still on the high

end of expected values, which confirms the presence of microdomains and the high crystallinity of the soft segment as well as a great phase immiscibility between the PEG and diisocyanate segments of the polymer. This high $\Delta H_m^{ss}\ value$ allows to determine the degree of crystallinity of the soft segments. Using the theoretical value for the melting enthalpy of PEG (189.5 $J.g^{-1}$), and taking into account that PEG represents 74.5% of the polymer weight (assuming total water evaporation upon drying of the polymer), the degree of crystallinity of the PEG segments in the polymer is 48.7%, which is quite high. [75] The peak present at 6°C upon cooling corresponds to the recrystallisation temperature, with a corresponding $\Delta H_c^{ss} = 56.6\ J.g^{-1}$. The new melting temperature upon reheating is shifted at 30.1°C which could indicate a loss of crystallinity upon recrystallization. [76,77]

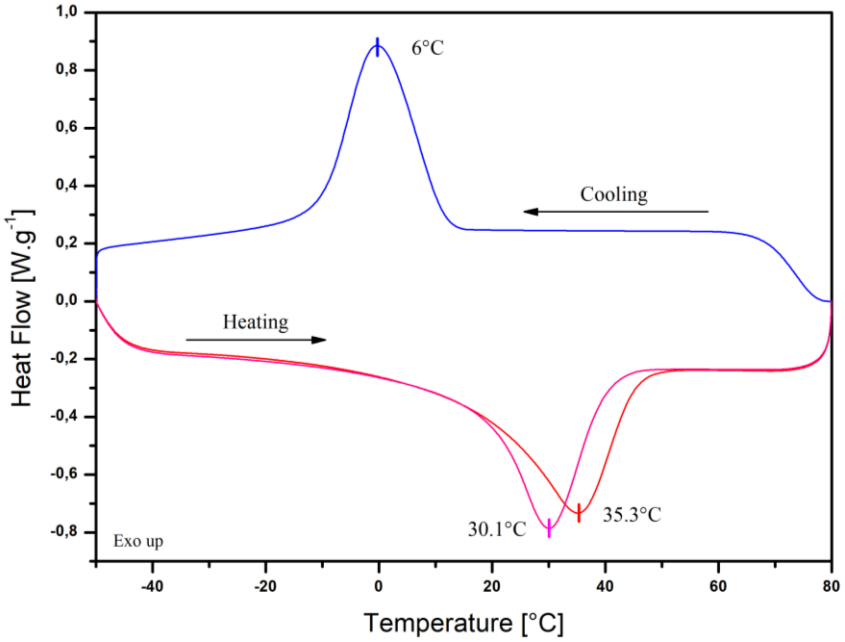

Figure 26 DSC measurement of butanediol-extended PU under N_2 atmosphere (100ml/min) at a rate of 10°C/min

The high crystallinity of the SS allows to attribute certain structures seen on SEM and AFM images of the same polymer. All SEM and AFM images presented in this work are images of the surface of coatings, previously coated with 5-7 nm of silver in the case of SEM, and with no additional treatments for AFM images (tapping mode).

SEM images (Figure 28) reveal a semi-crystalline spherulitic organization of the polymer with spherulite structures ranging between 10 and 37 µm in diameter, with a mean diameter of 22 µm. According to the DSC measurements, it can be assumed that these structures are constituted of the PEG segments since the high crystallinity required for these structures to form is met by the soft segment. AFM height images (Figure 27) are even more capable of confirming the presence of these semi-crystalline structures.

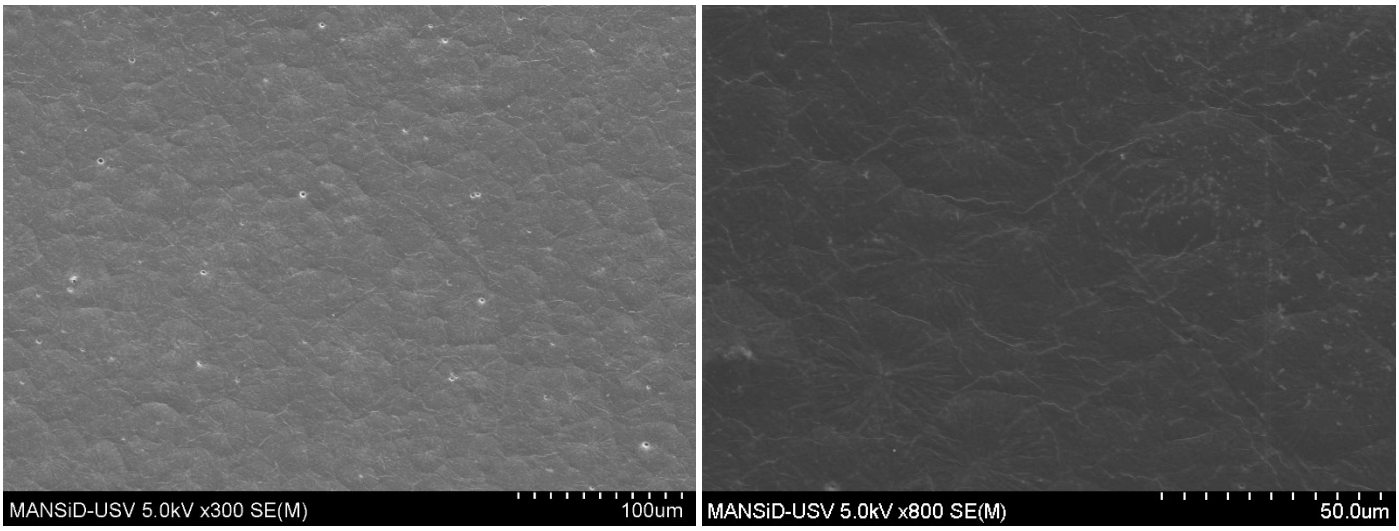

Figure 28 Scanning electron microscopy images of butanediol-extended PU revealing spherulitic structures

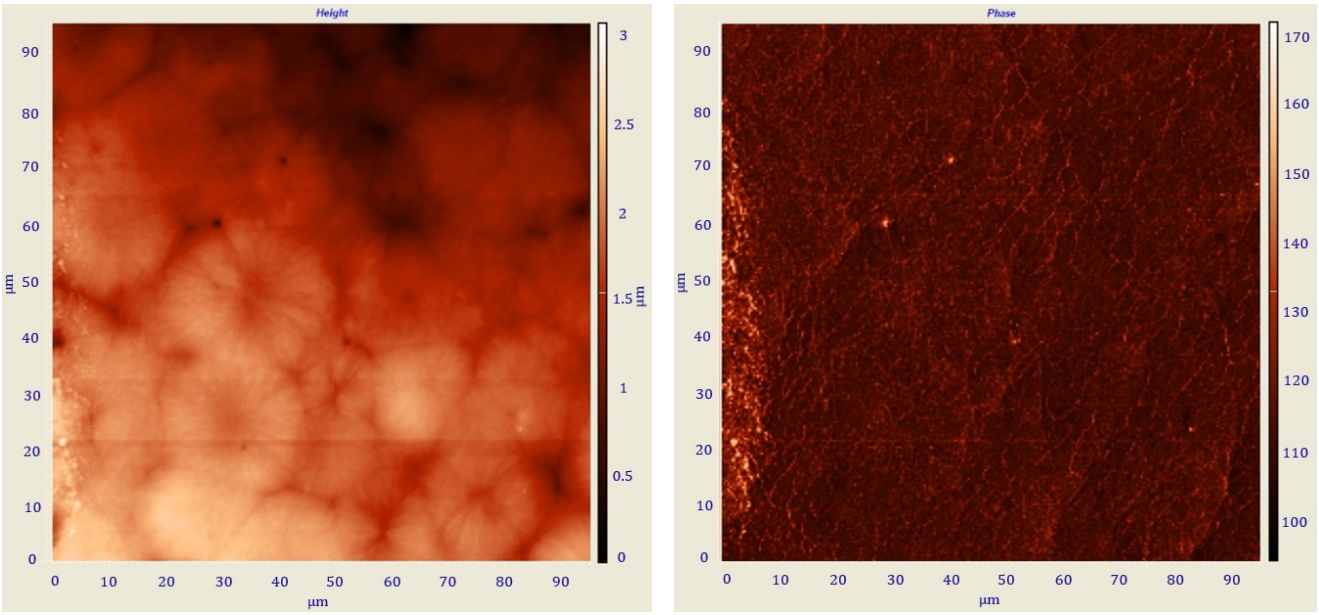

Figure 27 AFM images realized in tapping mode of butanediol-extended PU. Left) Height image Right) Phase image of a 100 µm² surface

Although the phase images were able to unveil microstructures when zooming, as seen on Figure 29, it is not clear whether these structures correspond to the soft and hard segment microphases, since they are usually present in more obvious ways in the literature and on a smaller scale (~µm or hundreds of nm). [74,78] Attempts at observing phase separation on a smaller scale was difficult due to the inability to avoid noise and artifacts for further zoomed images. Nevertheless, these images can be found in Annex 17.4. If the spherulites seen on height images are indeed made up of the soft segment, then it is reasonable to assume that the structures seen on Figure 29 are indeed made up of the hard segments. It is also possible that hard segment ordering can simply not be observed due to HDI tendency to have more disorder in the hard segment. [55] All the SEM and AFM images can be found in Annex 17.5.

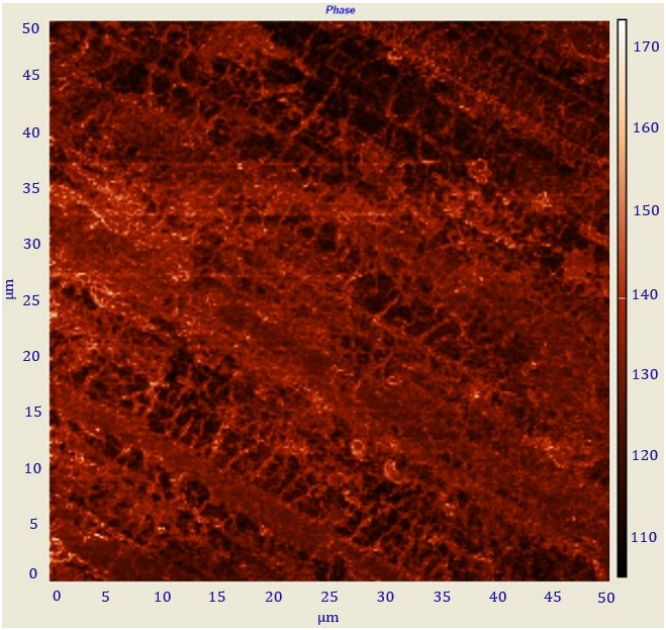

Figure 29 AFM phase image of a 50 µm² surface realized in tapping mode of butanediol-extended PU.

10. Selection of SCO compounds

The compounds which were selected for trials in the development of this technology were chosen based on a variety of criteria :

- They should be stable in air (the metal centre should not oxidise when in contact with oxygen), and ultimately in the selected polymer coating.
- They should also possess thermo- and piezochromic properties. Indeed, not all SCO complexes exhibit a change of colour when switching spin states. Particularly, most Fe^{III} and Co SCO complexes had to be discarded for that reason, and this work focusses exclusively on Fe^{II} compounds. As already mentioned, in terms of piezochromic properties, compounds with intermediate $\frac{\Delta V_{HS \rightarrow LS}}{\Delta S_{HS \rightarrow LS}}$ values would be preferable.
- They should preferably present bistable, hysteretic behaviour around room temperature, so that the compound is usable in most usual conditions, with no fatigue over multiple cycles. However, lower-temperature bistable compounds should not be discarded, as there is a real demand for low temperature piezochromic paints, especially in the aerospace field.
- For practical application, compounds which are easy to synthesize must be prioritized. Their production costs and the use of green (or no) reagents and solvents should also be considered, as well as their nontoxicity for environmental purposes.

Based on all these criteria, a category of Fe^{II} spin-crossover complexes is especially interesting : triazole complexes $Fe^{II}(L)_3X_2$, (L = triazole ligand, X = anion). They present in the form of one-dimensional coordination polymer chains where each Fe^{II} centre is coordinated with six triazole, and each triazole is coordinated with two metal centres. This structure is represented on Figure 30. The most commonly used ligands are 4-amino-1,2,-triazole (NH_2trz) and 1H-1,2,4-triazole. The anions are usually found between the chains and can sometimes help transmit interchain information by promoting various interactions, such as H bonds. [79]

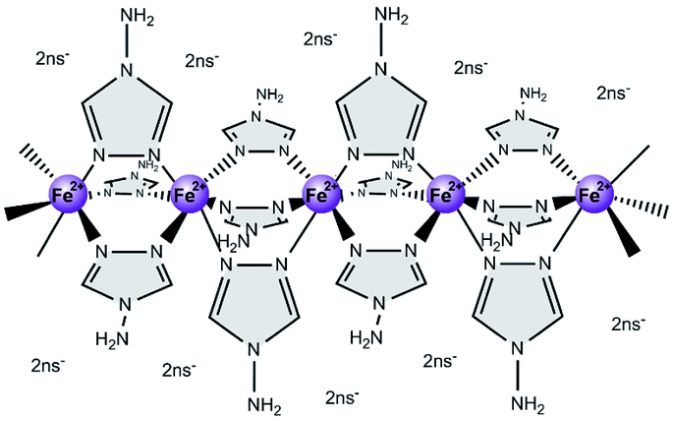

Figure 30 Example of an aminotriazole chain. Iron centres are surrounded by 6 ligands, and anions are found between the chains. [79]

Multiple triazole compounds have been tested, including : $[Fe(NH_2trz)_3](NO_3)_{2-x}(BF_4)_x$, $[Fe_{0.95}Zn_{0.05}(NH_2trz)_3]Cl_2$, $[Fe_{0.9}Zn_{0.1}(NH_2trz)_3]Cl_2$, $[Fe(Htrz)_{3-3x}(NH_2trz)_{3x}](ClO_4)_2 \cdot nH_2O$, $[Fe(NH_2trz)_3](NO_3)_2$ and $[Fe(NH_2trz)_3]Br_2 \cdot nH_2O$. In the remainder of this work, only $[Fe(NH_2trz)_3]Br_2 \cdot nH_2O$ will be discussed as it presented the best room temperature properties. Discussion about why some of the other compounds were discarded can be found in Annex 17.6, 17.7, 17.8.

Another very different compound, Fe(pyrazine)[Fe(CN)$_5$NO] will also be discussed for its interesting low temperature properties, as well as other reasons which will be explained later in this work.

10.1 $[Fe(NH_2trz)_3]Br_2 \cdot nH_2O$

A simple aminotriazole compound is $[Fe(NH_2trz)_3]Br_2 \cdot nH_2O$. This compound does present a hysteresis at room temperature, but **only** if it is hydrated. [80] The classical synthesis of triazole compounds is quite straight-forward, and is done according to the original protocol of Lavrenova *et al.*. [81] First, the iron salt (eg. $FeBr_2$) is solubilised in water and the triazole salt is solubilized in either ethanol, methanol, or water (the solvent may be heated to improve solubility). The iron salt solution is filtered and added drop-wise to the triazole solution under stirring then stirred for 3 hours. (It is worth noting that before this step,

ascorbic acid is also added, in order to avoid oxidation of the Fe^{II} into Fe^{III}. For the same reason, this acid will also be used as a potential solution to solve issues with the incorporation of the compound in the polyurethane. This subject is treated further along in this work.) The powder obtained can then either be centrifugated or filtered, depending on the grain size obtained, and washed with the same solvent mix used for the synthesis.

In this work, ethanol was used to solubilise NH_2trz, and the volumes used for NH_2trz and $FeBr_2$ were identical, so the final solvent mix in which the synthesis took place was a mix of 50/50 water-ethanol. The compound was indeed obtained this way, with a yield ranging between 56-70 %, depending on the volumes of solvents used, the separation technique (centrifugation or filtration) and the number of washes. As a side note, this solvent mix was used for the better dispersivity of its product in the WBPU. Indeed, $[Fe(NH_2trz)_3]Br_2$ synthesized only in water seemed to have greater difficulty at being dispersed in the aqueous polymer.

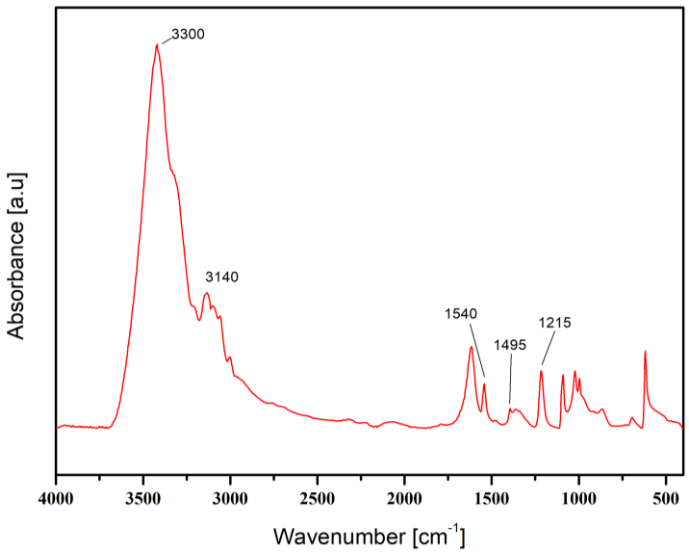

Figure 32 FTIR spectrum of $[Fe(NH_2trz)_3]Br_2 \cdot nH_2O$.

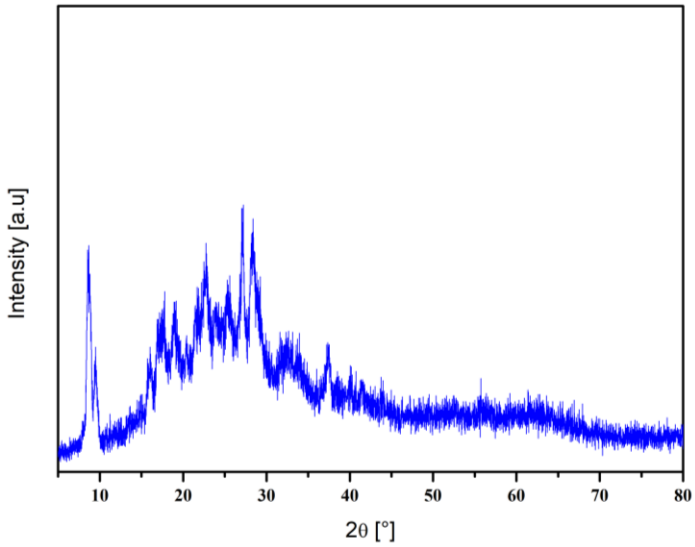

Figure 31 XRD diffractogram of $[Fe(NH_2trz)_3]Br_2 \cdot nH_2O$

FITR measurements were made to confirm the compound's nature (Figure 32), and it corresponds well to the available literature on $[Fe(NH_2trz)_3]Br_2$. As expected, the Fe-N signature peak is not visible since it belongs in the low frequency range between 250 to 300 cm^{-1}. [82] An interesting characteristic of this spectrum is the presence of a peak at exactly 1215 cm^{-1}. Indeed, the literature on triazole coordination compounds indicates that a 1215 cm^{-1} peak corresponds to a bi-coordinated triazole molecule, which further confirms the 1D polymeric structure of the compound. [82] The bands from 3140 to 3180 cm^{-1} correspond to the C=C and C=N vibrations of the aminotriazole cycle. [82] One band that differs from the literature is the very intense 3300 cm^{-1} peak, which can be attributed to the O-H bond of H_2O and confirms the presence of water in the compound.

The compound produced lacks crystallinity (Figure 31), as opposed to most other aminotriazole compounds, which displayed higher crystallinities. This lack of crystallinity is typical of $[Fe(NH_2trz)_3]Br_2 \cdot nH_2O$ and is believed to originate from the presence of H_2O in the lattice, introducing disorder in the structure.

To understand how prevalent H_2O is in the compound lattice, a TGA curve was recorded (Figure 34), which shows a loss of mass of approximately ~5.4% below 80 °C, attributed to water molecules. This mass corresponds to a stoichiometric ratio of 1.5 molecules per iron centre, so the compound can be written as **$[Fe(NH_2trz)_3]Br_2 \cdot 1.5H_2O$**. This is in contrast with the current literature, which identified 3 H_2O molecules per metal centre. [83,84] It is possible that this difference is due to the different solvent mix used during the synthesis, which might induce slight structural differences that disfavour the inclusion of H_2O into the solid. [24] Figure 34 clearly shows that the compound loses its water even at room temperature. Also, since the compound does not appear to recover its room temperature spin transition properties after heating, it can be assessed that it does not recover its water once lost.

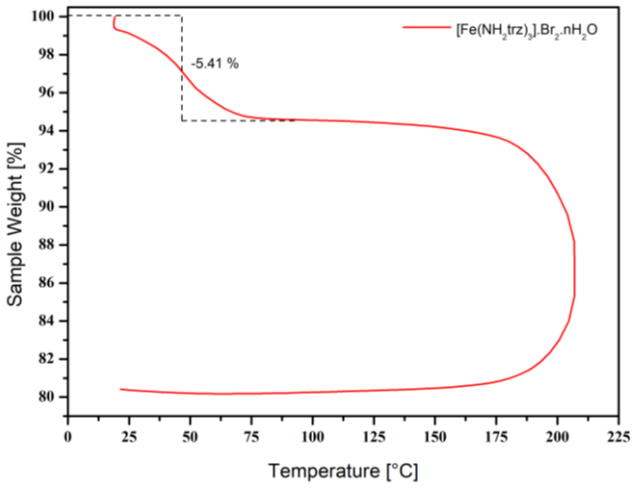

Figure 34 TGA curve of $[Fe(NH_2trz)_3]Br_2 \cdot 1.5H_2O$ recorded between 25°C and 210°C at a rate of 1°C/min under air (100ml/min)

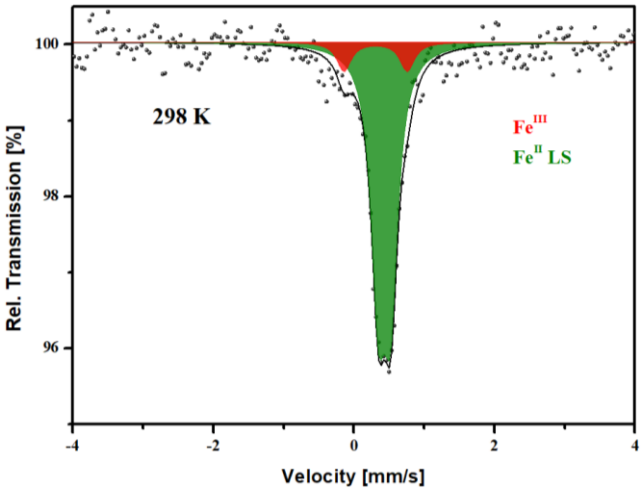

Figure 33 Mossbauer spectrum of $[Fe(NH_2trz)_3].Br_2$ recorded at 300 K, in the LS state

To confirm its purity, Mössbauer measurements were recorded on the compound at room temperature. Indeed, during the synthesis, iron centres in triazole compounds can oxidise into Fe^{III}, with a loss of cooperativity and a change in the SCO properties. Impurities coming from the reactants can also have the same effects. These impurities or oxidated states can usually be detected in Mössbauer.

Displayed on Figure 33, the best fit for this data was obtained by considering that a fraction of the iron present in the compound oxidised into Fe^{III} (red contribution). Indeed, this data (displayed in Table 2) is in accordance with previous measurements made on this compound. [85] Although this result might not indicate a general trend (a Fe^{III}-free compound is probably obtainable by tuning the amount of ascorbic acid added into the synthesis), it is

interesting in that it gives insight into a problem related to the inclusion of [Fe(NH_2trz-)$_3$]Br_2·1.5H_2O into the polyurethane polymer, which is discussed further in this document.

Table 2 Mössbauer parameters for the [Fe(NH_2trz)$_3$]Br_2·1.5H_2O system

[Fe(NH_2trz)$_3$]Br_2·1.5H_2O 298 K							
Fe^{II} LS site				**Fe^{III} site**			
δ [mm/s]	ΔE_Q (mm/s)	Γ (mm/s)	A (%)	δ [mm/s]	ΔE_Q (mm/s)	Γ (mm/s)	A (%)
0.436	0.1755	0.125	88.8	0.31	0.9	0.125	11.2

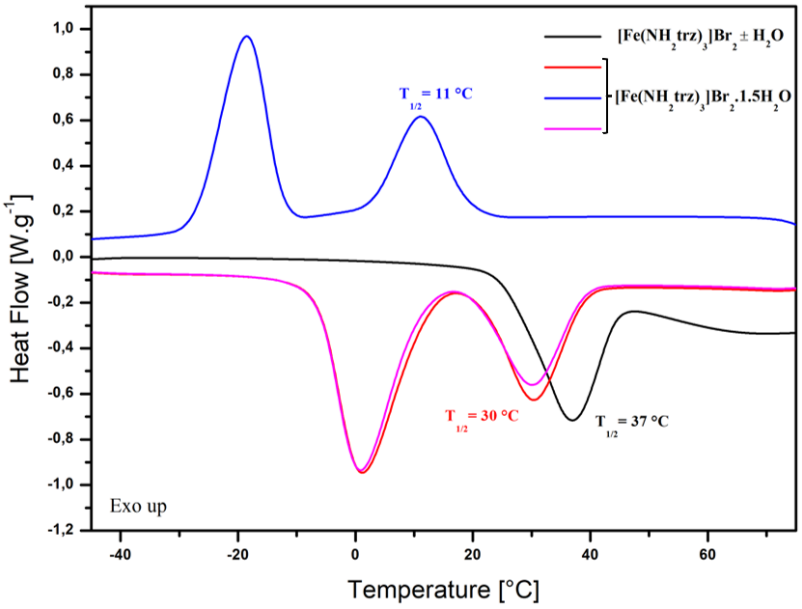

Figure 35 DSC measurements of [Fe(NH_2trz)$_3$]Br_2.1.5H_2O under N_2 atmosphere (100ml/min) at a rate of 10°C/min

The classical synthesis of the compound returned a purple powder, which could be switched to a white powder upon heating, with both states being stable at room temperature. Indeed, DSC measurements (Figure 35) on the compound revealed a room temperature hysteresis for the hydrated compound, with the upper bond of the hysteresis ($T_{max}^{\uparrow}$) = 30°C (303 K) and a lower bond ($T_{max}^{\downarrow}$) = 11 °C (284K) (red, purple and blue lines), which is almost in accordance with the literature ($T_{1/2}^{\uparrow}$ = 34°C, $T_{1/2}^{\downarrow}$ = 6°C). [86] The difference can probably be attributed to variations in the synthesis protocol, most notably the fact that literature only employs water as a solvent, whereas I used a mix of water and ethanol at a 50/50 ratio. Although, another possibility is that my version of the compound was more hydrated than theirs. Indeed, in order to be sure to observe the room temperature behaviour, the compound was exposed to an excess of water (which amounts to 13.4% of the total sample weight) which is the reason for the two peaks at -20 and 0 °C, which correspond to the crystallisation

and melting peaks of H_2O. [87] This also explains how the compound remains hydrated on the second cycle (as the RT behaviour is conserved).

It is interesting to see that a less hydrated version of the compound (black line) seems to transition at slightly higher temperature (37°C), or that the peak is shifted due to water loss, as TGA revealed that it loses water at the transition temperature (Figure 34). Indeed, the enthalpy variation $\Delta H_{HS\rightarrow LS}$ for the less hydrated compound ($27.4\ [kJ.(mol)^{-1}]$) is greater than for the hydrated compound ($17.37\ [kJ.(mol)^{-1}]$), which indicates the simultaneous departure of water for the less hydrated compound (black) (consistent with TGA measurements (Figure 34)). The shift to higher temperatures for the transition with variation of the water content is expected as already mentioned in Section 7.1. Looking at this same compound (black), an endothermic behaviour is observed above 50°C, which could again be attributed to loss of water, but could also be due to the appearance of a high T SCO phase, which could correspond to the completely dehydrated compound, $[Fe(NH_2trz)_3]Br_2$.

Nevertheless, in the presence of water the enthalpy of the LS → HS transition has been calculated as $\Delta H_{LS\rightarrow HS} = 17.37\ [kJ.(mol)^{-1}]$, assuming that all the Fe^{II} centres have transitioned, and correcting for the excess water. A similar value is obtained for the HS → LS transition ($-17.86\ [kJ.(mol)^{-1}]$). This value is not unexpected and is in accordance with the current literature on SCO compounds. [17,82,86,88–90]

Considering a simple non-interacting model, the entropy variation associated with the spin transition can then be computed by simply using the relation of Eq. (7) and is found at $\Delta S_{LS\rightarrow HS} = 57.32\ [J.(K.mol)^{-1}]$, which is in the upper limit of what has already been described for aminotriazole compounds. The same formula was used for the HS → LS transition with a found $\Delta S_{HS\rightarrow LS} = -62.89\ [J.(K.mol)^{-1}]$ If we remove the general spin contribution $\Delta S^{spin} = 13.38\ [J.(K.mol)^{-1}]$, we obtain a value for the vibrational contribution of the entropy ${\Delta S_{LS\rightarrow HS}}^{vib} = 43.94\ [J.(K.mol)^{-1}]$, ${\Delta S_{HS\rightarrow LS}}^{vib} = -49.51\ [J.(K.mol)^{-1}]$. The enthalpy and entropy values are a first step to be able to describe the thermodynamical behaviour of the SCO with respect to pressure. However, since the volume variation from the SCO is not known yet for $[Fe(NH_2trz)_3]Br_2{\cdot}nH_2O$, it is not possible to predict the threshold pressure. An attempt at estimating that volume variation based on experimental pressure measurements is made further on in Section 13.2.

Using a SQUID magnetometer, the high temperature phase (dehydrated phase) is observable, which displays a hysteresis between $T_{1/2}^{\uparrow}$ = 58°C (331 K) and $T_{1/2}^{\downarrow}$ = 47°C (320 K), although a small bump indicating that some part of the compound remains hydrated is visible on the first cycle (Figure 36). This is not in accordance with the literature ($T_{1/2}^{\uparrow}$ = 48°C, $T_{1/2}^{\downarrow}$ = 32°C) [83], with a shift of about 10°C towards higher temperatures, which could be explained by the different solvent mix engendering a different phase of the same compound.

Indeed, all literature on this compound used water as solvent for $FeBr_2$ as well as NH_2trz, while, as a reminder, in this work ethanol is used as solvent for NH_2trz. [80,83–85] Furthermore, literature on this compound already suggests the existence of different phases. [24] As explained in Section 6.2, a χT of ~ 3.5 $[cm^3.K.mol^{-1}]$ corresponds to a total HS fraction. Here, such values are found at high T, which indicates that the compound totally switches from LS to HS. However, the value of $\chi T \sim 0.44\ [cm^3.K.mol^{-1}]$ at low T, suggests that a fraction of centres which are not in LS (~12%). This is not unexpected for aminotriazole compounds and there are two explanations. First, considering the Fe^{II} centres at the end of the chains, they are not coordinated with 6 NH_2trz but rather 3 NH_2trz and 3 H_2O molecules. Water is known as a weak ligand, thus inducing a small field splitting and favouring the HS state, thus a fraction of the Fe^{II} centres remains in the HS state. In this context, the smaller the chain, the bigger fraction these residual HS centres represent. Furthermore, the second explanation could be a partial oxidation in Fe centres into Fe^{III}, which is more consistent with the Mössbauer measurements (which estimates 11.2% of Fe^{III} phase). [29,91] Nevertheless, Taking this non-switching HS fraction into account, the new enthalpy variation comes out at $\Delta H_{LS\rightarrow HS} = 19.74\ [kJ.(mol)^{-1}]$ and $\Delta S_{LS\rightarrow HS} = 65.14\ [J.(K.mol)^{-1}]$ (and $\Delta H_{HS\rightarrow LS} = -20.3\ [kJ.(mol)^{-1}]$, $\Delta S_{HS\rightarrow LS} = -71.47\ [J.(K.mol)^{-1}]$).

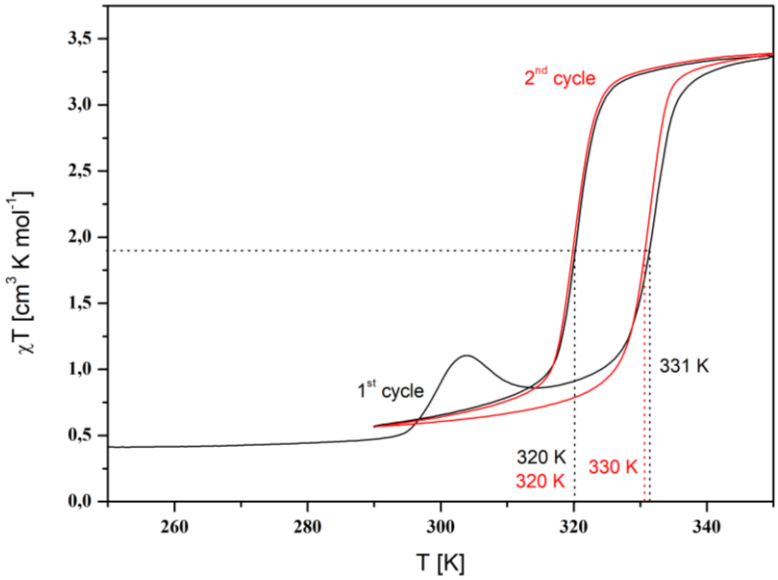

Figure 36 SQUID magnetic measurement of the high T phase of $[Fe(NH_2trz)_3]Br_2$ (classical synthesis) magnetic field = 1000 Oe and scan rate = 2K/min

10.2 Aminotriazole compounds synthesis

In the context of industrial application, the synthesis of a piezochromic SCO compound represents an important step, in terms of cost and consumption (e.g. : solvents). This is why the following section explores multiple ways of synthesizing these SCO compounds. Here are laid out the important steps of the classical solvent-based synthesis as well as two other

synthesis pathways for 4-aminotriazole 1D chains, which comprise most of the compounds used in this work.

10.2.1 Classical, solvent-based synthesis

This synthesis method is the one described above and is the most commonly used in research, but it requires high solvent quantities as well as some heating. It also requires a non-negligible amount of time to be carried out.

10.2.2 Mechanochemical synthesis

Recently, researchers have presented a novel way of synthesizing aminotriazole coordination compounds via mechanochemical means. [92,93]

The mechanochemical synthesis is simple in its conception : both the iron and triazole salts are mixed in solid form in a mortar (with a small amount of acid e.g. ascorbic acid to avoid oxidation of the Fe^{II} centres into Fe^{III}), then they are ground together to improve contact and allow an exchange between the two species. On Figure 37 is displayed the result of this current work on the mechanochemical synthesis of $[Fe(NH_2trz)_3]Br_2 \cdot nH_2O$. It is worth noting that to obtain the compounds that are desired in this work, a few drops of water needed to be added. Indeed, the Fe^{II} salts used by the researchers were hydrated, which I believe allowed the release of H_2O once ground and served as a medium for the exchange of molecules between the solids. However, the salts used in this work were not, and thus required an external exchange medium.

Figure 37 $[Fe(NH_2trz)_3]Br_2 \cdot nH_2O$ at room temperature, synthesized via mechanochemical synthesis, in the HS state (left) and LS state (right)

One possible drawback is that the final compound tends to be less crystalline than with the classical method (Figure 39), which could be the reason for the slightly more gradual spin transition measured for this compound (Figure 38). Although, the high T phase hysteresis remains centred on the same temperature and is a bit larger (14 K against 11 K for the classical synthesis) and the fraction of residual HS centres is smaller (0.25 against 0.44 $[cm^3.K.mol^{-1}]$) which could be clues indicating longer SCO chains in the mechanosynthesized compound.

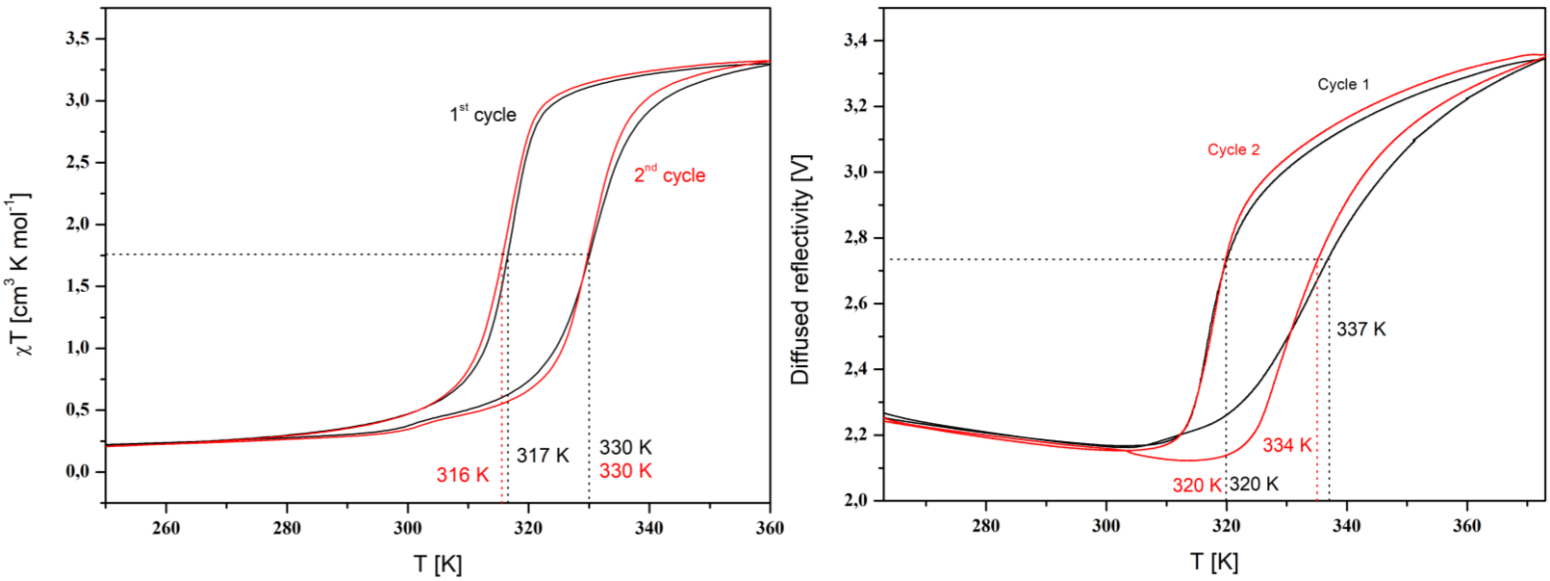

Figure 38 Left) SQUID magnetic measurement of the high T phase $[Fe(NH_2trz)_3]Br_2$ synthesized via mechanochemical synthesis, with a magnetic field = 1000 Oe Right) Opt. Refl. Measurement of the high T phase $[Fe(NH_2trz)_3]Br_2$ synthesized via mechanochemical synthesis, all at a scan rate of 2K/min

This method as the advantage of requiring (almost) no solvent, as well as being fast (the compound can be obtained with less than 5 min. of grinding) and requiring no heating. It is worth mentioning that this synthesis method can also be used on already synthesized compounds. That is, it is possible to use it to introduce reactants to an already formed coordination polymer. [93] This fact will be useful in a following section of this work concerning the association of SCO properties with fluorescence in Section 14.

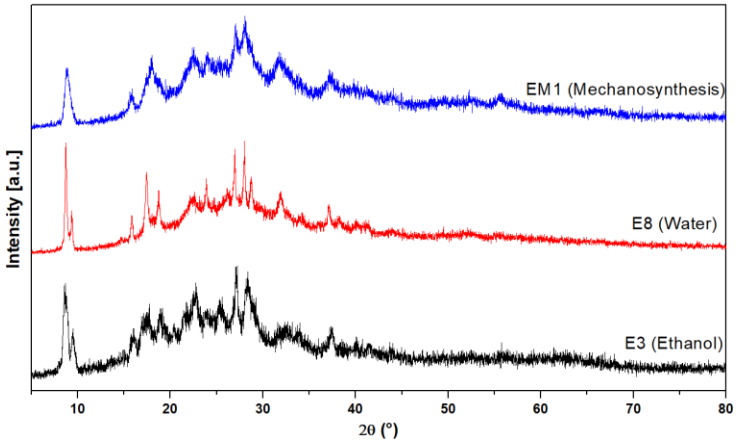

Figure 39 XRD diffractogram illustrating the poorer crystallinity of mechanosynthesized $[Fe(NH_2trz)_3]Br_2 \cdot nH_2O$ (blue) in contrast to conventional synthesis (red, black)

10.2.3 *In situ* synthesis

The success of the mechanochemical synthesis for the obtention of the target SCO compound (eg. $[Fe(NH_2trz)_3]Br_2 \cdot nH_2O$) prompted to undertake another test. Indeed, as explained in the previous section, a diffusion medium is required for the ionic exchange

between the Fe and triazole solids. In mechanochemical synthesis, that medium is water, either coming from hydrated Fe salts or added into the mix.

While the mechanochemical synthesis already presents advantages over conventional synthesis methods, it still requires a drying step after grinding, and then to be incorporated into the polyurethane dispersion.

A novel synthesis method, which is dubbed "*In situ*" synthesis, aims to use the polyurethane dispersion as exchange medium. Preliminary tests were conducted by introducing the iron salt and 4-aminotriazole solid into the liquid polymer and showed promising results upon grinding, as depicted on Figure 40. I believe this method could deserve further attention to determine whether it would ultimately be useable.

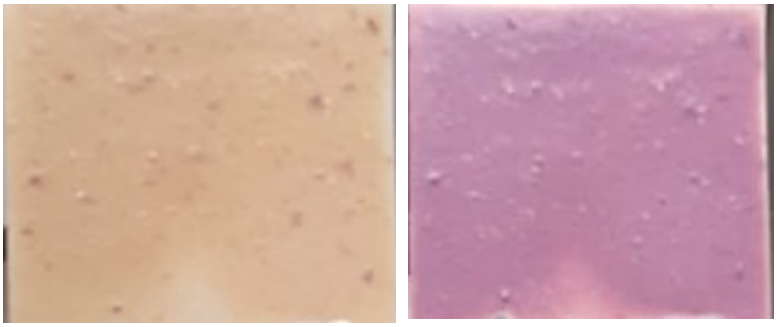

Figure 40 PU-[Fe(NH$_2$trz)$_3$]Br$_2$·nH$_2$O Hybrid obtained via In situ synthesis. (left) HS state (right) LS state

10.3 Fe(pyrazine)[Fe(CN)$_5$NO]

A quite recently discovered compound, which is not part of the triazole family, was also selected for trial due to its interesting low temperature properties. Indeed, as can be seen from Figure 43, it presents a 40 K wide hysteresis centred below room temperature. [88] The structure of this compound is displayed on Figure 41 and is composed of a 2D Fe^{II} nitroprusside network, with pyrazine molecules also involved in the coordination of the metal centres, thus linking the 2D sheets together, and forming a 3D nitroprusside network.

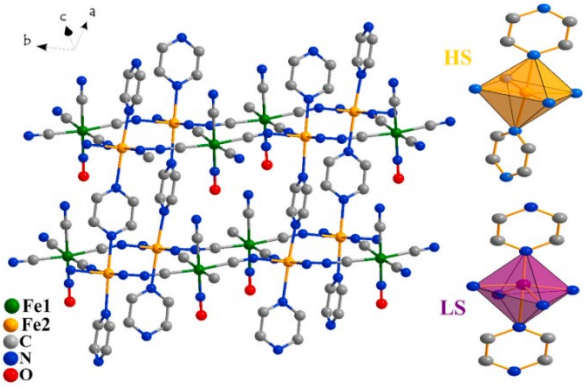

Figure 41 Atomic framework of Fe(pyrazine)[Fe(CN)$_5$NO] [88]

What is interesting about this compound is that the colours that are characteristic of the HS and LS states are not white and purple like for most Fe^{II} triazole compounds, but rather red in the LS state and orange in the HS state. This difference in colour is due to the metal-ligand charge transfer (MLCT) change of the iron centre during the SCO, as well as the MLCT of the nitroprusside $(Fe(CN)_5NO)^{2-}$ part of the molecule, as Sodium Nitroprusside is orange in powder form. [88] This means that it could be used in conjunction with a more traditional triazole chain (which is white and purple). This could be advantageous since a 2-compound system allows for simultaneous pressure and temperature determination, whereas a single-compound system only allows for pressure determination, by making a hypothesis on the temperature at which the pressure was applied. This is an aspect that will be discussed in Section 12.3. [88]

The compound was not obtained by following the procedure provided in the original article, but rather via another synthesis method graciously provided by the authors of that article. The synthesis involved dissolution and mixing of Sodium Nitroprusside and Mohr's salt in water to produce a precursor: $Fe[Fe(CN)_5NO].xH_2O$. Then, pyrazine dissolved in ethanol is introduced under strong stirring, in order to break the Fe-NC bonds between the 2D layers from the ferrous nitroprusside, and introduce pyrazine in the structure, producing the 3D coordination polymer $Fe(pyrazine)[Fe(CN)_5NO]$.

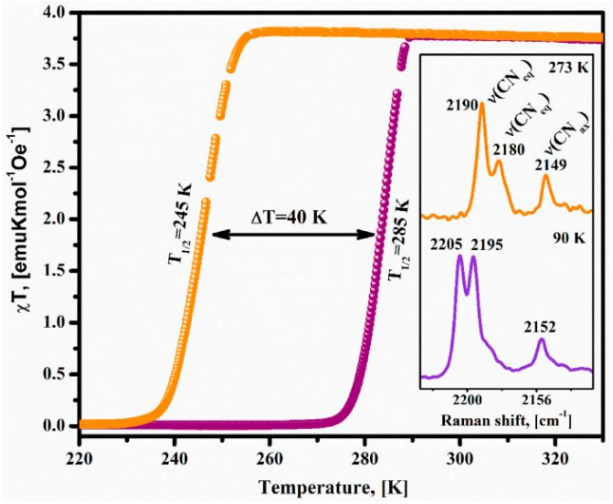

Figure 43 Magnetic properties of $Fe(pyrazine)[Fe(CN)_5NO]$ [88]

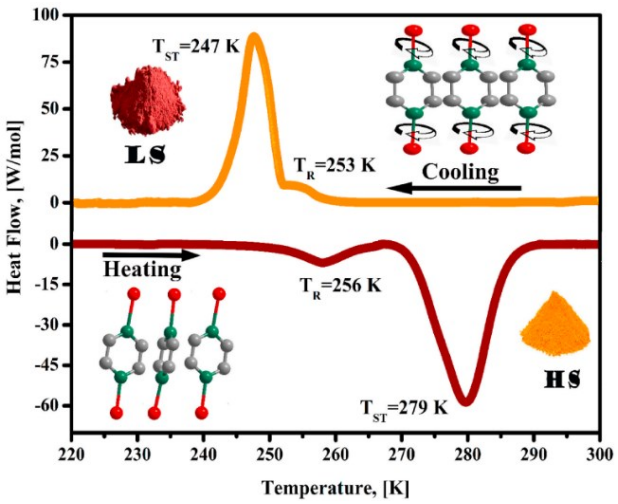

Figure 42 DSC of $Fe(pyrazine)[Fe(CN)_5NO]$ [88]

Confirmation of the resulting compound was done through by XRD measurements. After correction of the 2Θ values for the same λ source, the XRD diagram matches that from literature. (Figure 45, figures from the literature can be found in Annex 17.9)

FTIR measurements also lead to the conclusion that the compound obtained is identical to the one from the literature (Annex 17.9), as all the peaks are in correspondence. However, the presence of a 3400 cm^{-1} peak (as shown on Figure 44) in the synthesized compound

suggest that some $Fe[Fe(CN)_5NO]\cdot xH_2O$ is still present. Thus, the time of reaction was lengthened in order to make sure to completely convert the precursor.

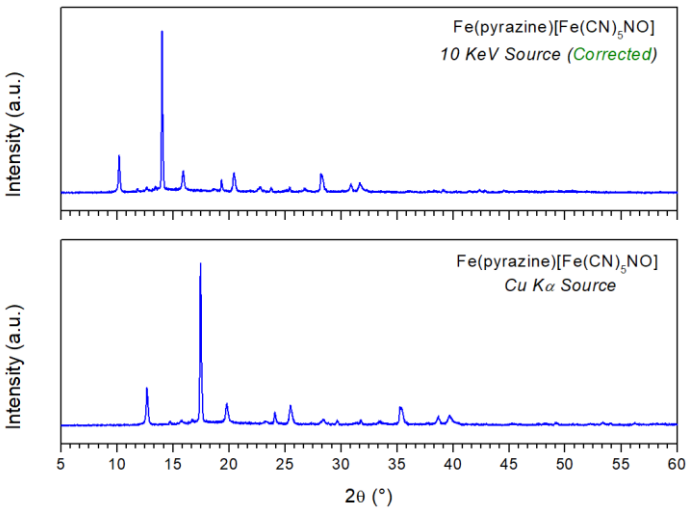

Figure 45 Left : XRD data from synthesized Fe(pyrazine)[Fe(CN)5NO]

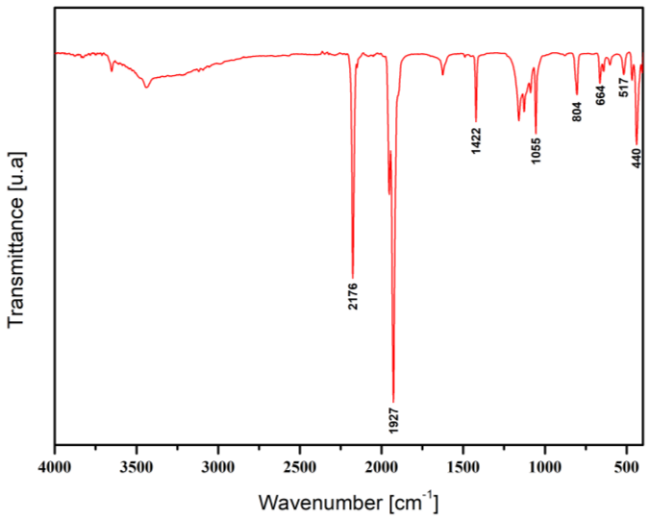

Figure 44 FTIR data for synthesized Fe(pyrazine)[Fe(CN)5NO

To further check the validity of the synthesized compound, Mossbauer measurements were conducted.

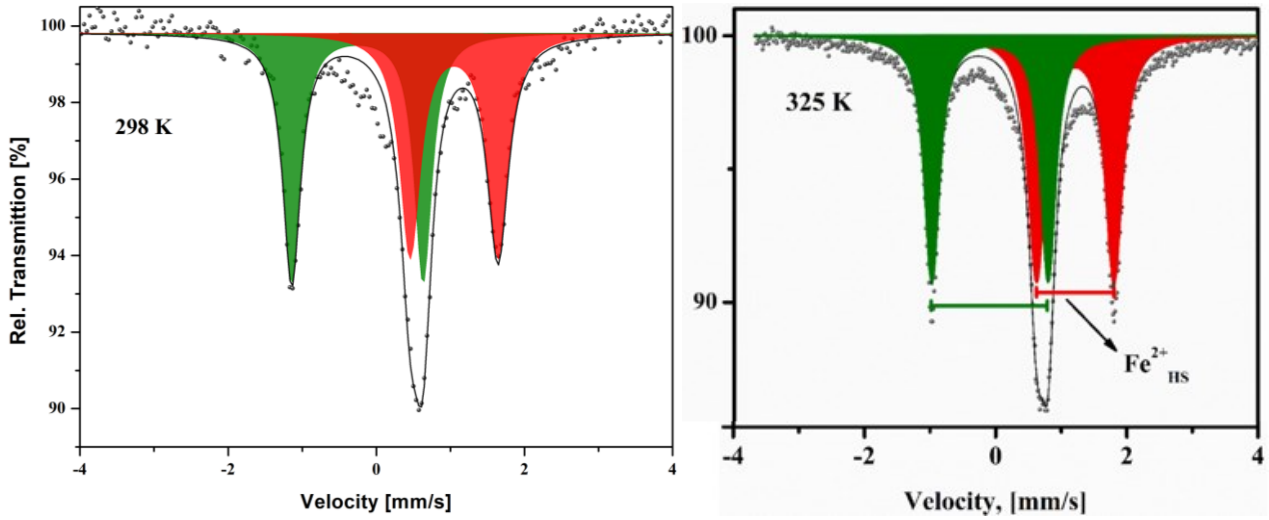

Figure 46 Mössbauer measurements at Left) 298 K *Right) 325 K, from literature [88]*

The obtained result is similar to the literature (Figure 46). These new measurements shown on Table 3 only differ by the isomer shift values, which are shifted by ~0.25 mm/s to lower values. Nevertheless, it can be concluded that the compound obtained is similar, because these isomer shift values can be explained by the fact that the measurements were made at different temperatures (298K vs. 325K), which will lower the isomer shift. More importantly, the article used sodium nitroprusside as calibration reference whereas the Mössbauer apparatus in the CMOL laboratory uses regular iron foil (α-Fe). Indeed, there is

about a 0.257 mm/s difference between the two references, which roughly corresponds to the observed difference. [88,94]

Table 3 Mössbauer parameters for Fe(pyrazine)[Fe(CN)$_5$NO] synthesized in this work (reference = Iron foil), and [88](SNP)

Current work 298 K				**Research article [88] 325 K**				
δ [mm/s]	ΔE_Q [mm/s]	Γ [mm/s]	A (%)	δ [mm/s]	ΔE_Q [mm/s]	Γ [mm/s]	A (%)	Assignment
-0.255	1.776	0.145	49	-0.09	1.776	0.28	50	[Fe(CN)$_5$NO], LS
1.05	1.185	0.17	51	1.212	1.181	0.31	50	Fe(NC)$_4$(Pyr)$_2$, HS

11. Powder pressure tests

Since part of this work will focus on [Fe(NH$_2$trz)$_3$]Br$_2$·nH$_2$O, the first important test to carry out is to check that they indeed present piezochromic properties at room temperature. A rudimentary check was conducted, by simply applying pressure by hand, the result being displayed on Figure 47.

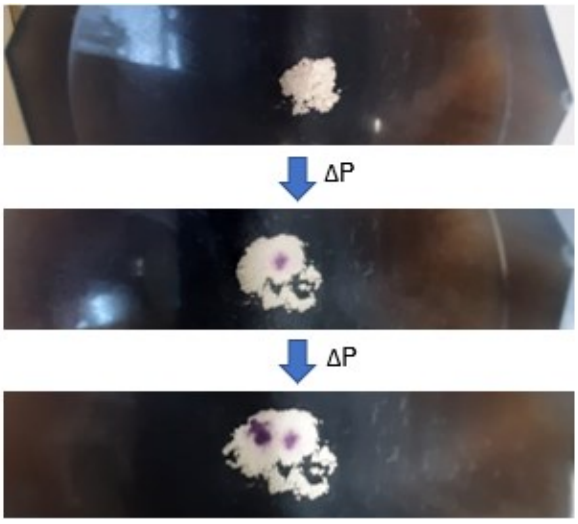

Figure 47 Test establishing the presence of piezochromic properties of [Fe(NH$_2$trz)$_3$]Br$_2$.nH$_2$O at room temperature

There is indeed a change of colour, thus a switch from HS to LS, upon application of a pressure. It is also important to note that this colour switch is stable at room temperature.

The piezochromic properties of this compound are confirmed, and they are ready to be tested in a hybrid SCO/PU material.

12. Hybrid material

12.1 $Fe(NH_2trz)_3]Br_2.nH_2O$-PU hybrid : First trials

As discussed previously, the hybrid coating material can be produced by either incorporating the SCO compound inside the polyurethane dispersion, or via *In situ* synthesis, where the SCO compound is directly synthesized inside the dispersion. Here is discussed the results obtained via the first production method, but the same principles probably also apply with the *In situ* method.

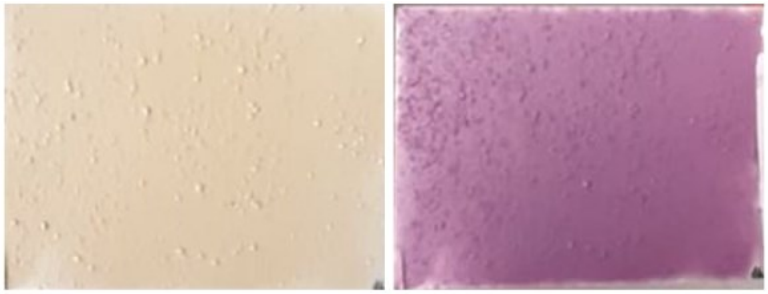

Figure 48 Thermochromic properties of the first hybrid coating tests. Coating at room temperature in the HS state (left) and LS state (right)

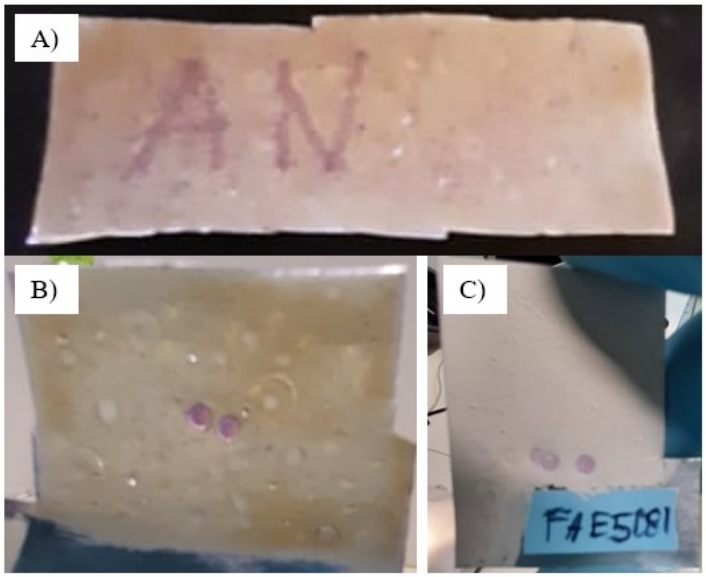

Figure 49 Piezochromic properties of the first hybrid coating tests, a,b) 15% w/w of SCO compound $[Fe(NH_2trz)_3]Br_2 \cdot nH_2O$ c) 30% w/w of $[Fe(NH_2trz)_3]Br_2 \cdot nH_2O$, 5% w/w of TiO_2 added for whiteness.

The first results worthy of mention is via the incorporation of 15-30 % *w/w* of $[Fe(NH_2trz)_3]Br_2 \cdot nH_2O$ into the polyurethane dispersions (**D8** and **D9**, EDA-extended), followed by subsequent application on an aluminium sheet. This constituted the first trial for

a hybrid material, represented on Figure 48 and Figure 49, exhibiting both piezo- and thermochromic properties around room temperature, which meant the hysteretic behaviour of $[Fe(NH_2trz)_3]Br_2{\cdot}nH_2O$ was conserved after incorporation. Figure 49a shows that the piezochromic properties of $[Fe(NH_2trz)_3]Br_2{\cdot}nH_2O$ are sensitive enough to respond to low pressure, which indicates that its threshold pressure is probably small, and makes this material suitable for pressure-inscription. Figure 49b shows the piezochromic properties of the coating, but also the reversibility. Indeed, many impacts can be seen on the coating, which come from previous tests and are now completely in the HS state, which demonstrates the total reversibility of the technology. Figure 49c is an attempt at obtaining a more aesthetic (thus more practical for real-world use) version of this same coating, by incorporating additional TiO_2, which is a common additive in paints and coatings. [95]

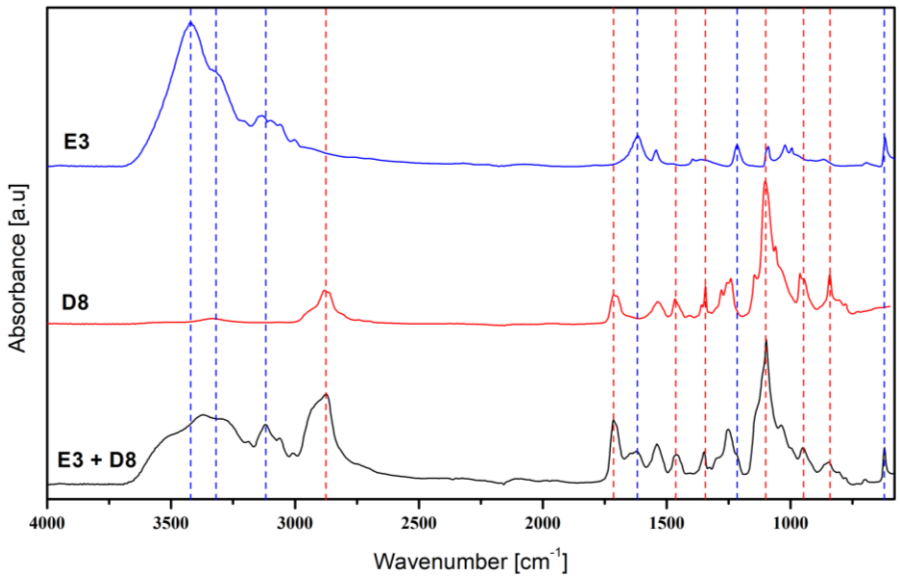

Figure 50 FTIR spectra of $[Fe(NH_2trz)_3]Br_2{\cdot}nH_2O$ (E3), PU dispersion (D8), and the hybrid coating (E3 + D8). Blue dotted lines correspond to peaks attributed to the SCO compound; Red dotted lines are peaks attributed to the PU polymer.

FTIR measurements were conducted on these hybrid coatings, to confirm the incorporation of the SCO compounds into the synthesis. Indeed, Figure 50 illustrates the presence of both $[Fe(NH_2trz)_3]Br_2{\cdot}nH_2O$ (**E3**) and the WBPU (**D8**) characteristic peaks in the hybrid material. Since no abnormal peaks appeared in the hybrid compound, it can safely be assumed that both the SCO compound and the PU remain largely unchanged. One important information that these measurements reveal is that the SCO compound $[Fe(NH_2trz)_3]Br_2{\cdot}nH_2O$ retains at least part of its water in the dried hybrid coating, as evident by the presence of ~3300 cm^{-1} peaks for the hybrid. This is of capital interest since this means we can expect the compound to retain its favorable room-temperature properties, which are linked to this uncoordinated water.

Perhaps the most important result from this first test is the complete, almost instant reversibility of the color change (so the spin state change) induced by the applied pressure.

This is done by simply heating the coating above the higher spin state switch temperature ($T_{1/2}\uparrow \sim 310$ K, Figure 49). This property has been tested through multiple cycles without discernable fatigability of the material, demonstrating the conditional reversibility of the material. All these beneficial properties clearly demonstrate the usefulness of this technology in pressure sensing, but applications can be thought of in many other fields.

Attempts at mapping the behaviour of the hybrid has been made via optical reflectivity and SQUID magnetic measurements, between -10 and 80 °C at a rate of 2°C/min. The results of the optical reflectivity measurements are displayed on Figure 51. These reveal the presence of both the hydrated form, $[Fe(NH_2trz)_3]Br_2 \cdot 1.5H_2O$, with a room temperature hysteresis and the non-hydrated form at higher temperatures. While on the first cycle the high T phase hysteresis is in good accordance with the magnetic measurements for the compound presented in Section 10.1, there seems to be a shortening of the hysteresis on the second cycle. Although, this could be a result of the combination of the PU+SCO in the sample, which might induce effects other than the SCO modifying the reflective intensity. A similar shortening can be observed for the room temperature phase, with the hysteresis width for the second cycle in clear accordance with the DSC (Figure 35) measurements realized on $[Fe(NH_2trz)_3]Br_2 \cdot 1.5H_2O$.

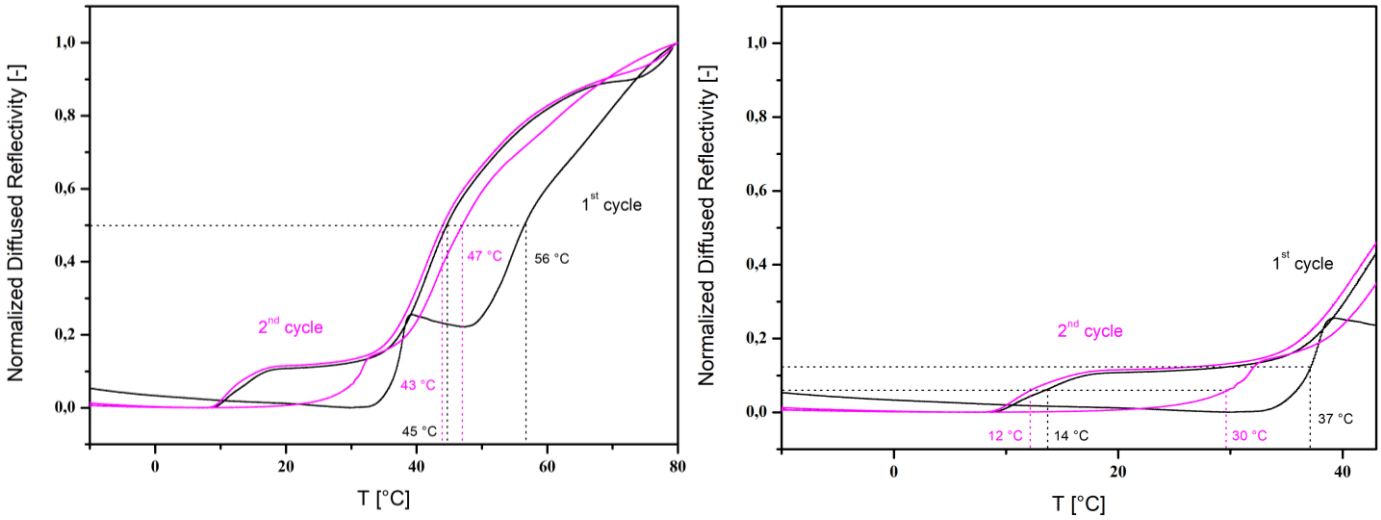

Figure 51 Optical reflectivity measurements on $[Fe(NH_2trz)_3]Br_2$-PU hybrid between -10°C and 80°C at a rate of 2°C/min.

Although the optical reflectivity measurements reveal the presence of the high T phase, which would indicate that the coating would always be partially purple (LS) at room temperature, even when cooling down from higher temperatures, the coatings can be completely white at room temperature, as has been shown on Figure 48 for example. The simplest explanation for this is that the hydrated form is only found at the surface of the SCO particles, while the rest of the compound is in the non-hydrated form. This would explain why the SQUID magnetic measurements (Figure 52) of this hybrid compound is not able to map the room temperature hysteresis, while the FTIR measurements (Figure 50) confirmed

the retaining of part of the compound' water in the hybrid coating. Indeed, measuring the optical reflectivity (effectively measuring the colour change) with respect to temperature favours the signal of surface metal centres, while the magnetic measurements which measure the magnetic behaviour over the entire sample will not favour the surface because it only makes up a tiny fraction of the entire mass of the compound.

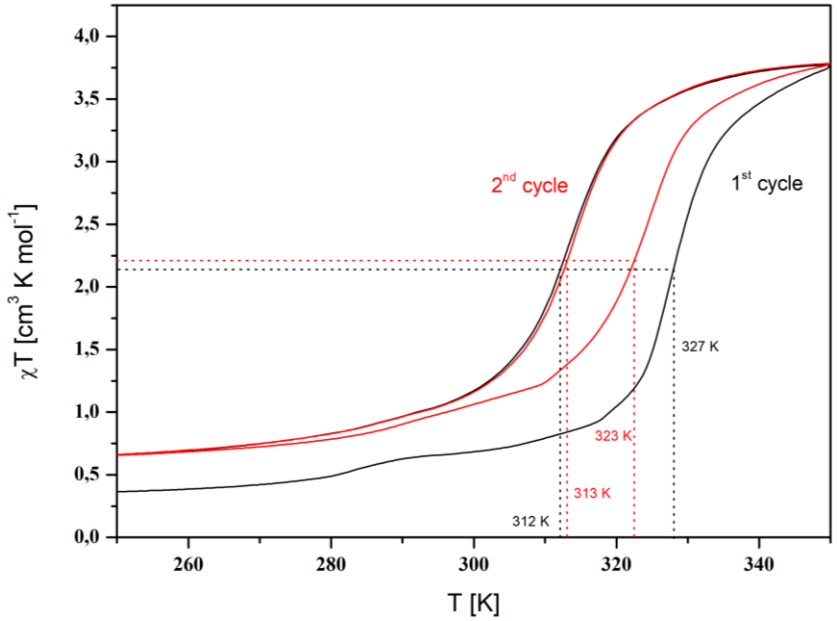

Figure 52 SQUID magnetic measurements on [Fe(NH₂trz)₃]Br₂-PU hybrid between -10°C and 80°C at a rate of 2°C/min, under a magnetic field of 1000 Oe

Macroscopically, it is possible to observe some interaction between the polyurethane and the compound. Indeed, it is clearly visible on Figure 49 that the coatings can present a yellowish colour in the HS state, and the need for TiO_2 to obtain a white coating. However, both the isolated compound in the HS state and the polyurethane dispersion are white before mixing (see Figure 53). This points to the presence of SCO-polyurethane chemical interactions.

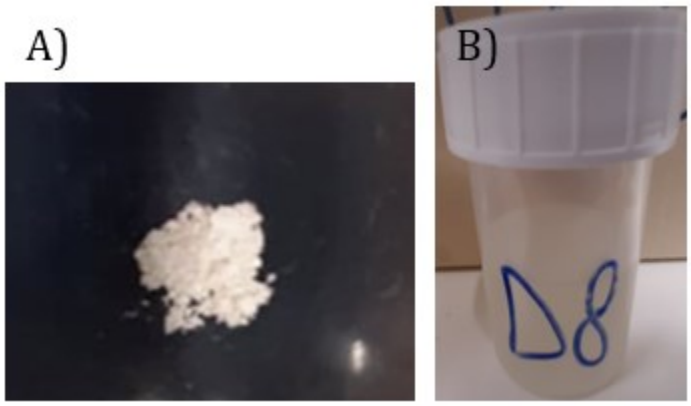

Figure 53 a) SCO powder in the HS state b) Polyurethane dispersion prior to incorporation into the hybrid coating

The first, most obvious credible hypothesis for these interactions was that the Fe^{II} centres were being oxidised into Fe^{III}. This idea was comforted by the effect of ascorbic acid. Indeed, when ascorbic acid was introduced at the same time as the SCO compound in the polyurethane dispersion, the hybrid retained its white colour, as is made clear on Figure 54a. However, as the coating started drying (Figure 54b), the effect of ascorbic acid started to faint.

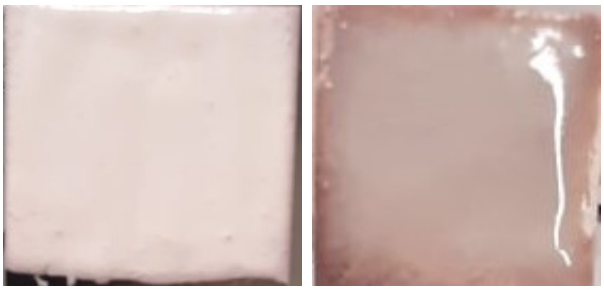

Figure 54 a) SCO + ascorbic acid, wet b) SCO + ascorbic acid, drying

To try to figure out the cause of these interactions, experiments were conducted by observing the effect of each of the polyurethane components on the SCO compounds. They were each separately mixed with the compounds, and the presence or absence of observed interactions are recorded in the following table:

Table 4 Summary of the presence of interactions for the different components of the polyurethane dispersion

Component	***Interaction***
Diisocyanate	NO interaction
DMPA	NO interaction
PEG	NO interaction
Triethylamine (TEA)	Definite interaction
Ethylenediamine (EDA)	Definite interaction

These tests revealed the effects of both TEA, which is used as neutralizer and ethylenediamine, a common chain extender. Both molecules are aminated, and SCO complexes with ethylenediamine as ligand have already been studied. [96] This led to the second hypothesis regarding the SCO-PU interactions: the replacement of current SCO ligands and complexation of Fe^{II} by either TEA or EDA.

To confirm this hypothesis, both Mössbauer and FTIR measurements were used. Unfortunately, it was not possible to confirm the presence of these interactions via Mössbauer, which does not necessarily equate to their absence since it is possible that the method might not be sensitive enough to detect them. Still, Mössbauer was useful because it

confirmed the absence of Fe^{III} sites like the one seen on Figure 33, thereby negating the oxidation hypothesis, as seen on Figure 55.

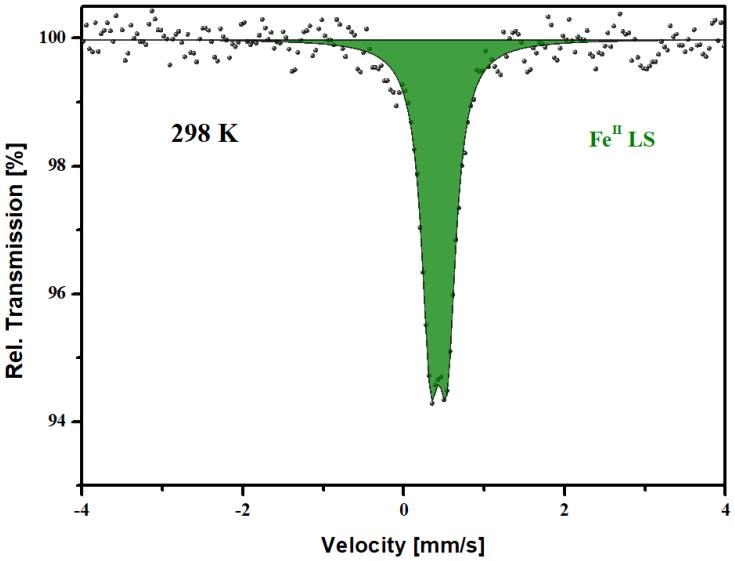

Figure 55 Mössbauer measurement of $[Fe(NH_2trz)_3].Br_2.1.5H_2O$ into the PU polymer (hybrid)

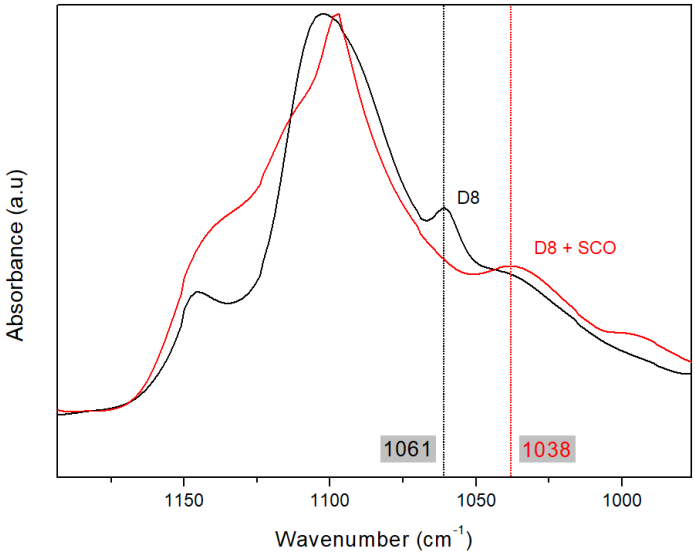

Figure 56 FTIR spectra of PU (black) and PU+$[Fe(NH_2trz)_3].Br_2.1.5H_2O$ (red)

However, FTIR measurements could be able to reveal the interactions (Figure 56). Indeed, by comparing the spectra of the polyurethane coating and the hybrid PU+SCO material, we observe a shift of a 1061 cm^{-1} peak to lower wavenumber in the hybrid. This peak can be attributed to a C-N stretch mode of TEA. [97] Thus, the shift could be explained by the fact that coordination of TEA via N to Fe^{II} would reduce the electronic density around the C-N bond, thereby reducing the force constant and lowering the vibration frequency. This represents the first concrete evidence of these interactions.

The first and easiest way to try and solve this issue is to synthesize a polyurethane dispersion with less EDA, therefore reducing the chain extension ratio. For this test, the chain extension ratio was reduced to 90%, instead of 100%. However, the deleterious effect was still very much present. This means that either the SCO compounds were interacting with the EDA in the polyurethane chains, or that there is still free EDA leftover (that has not reacted with the polymer chains), even at low chain extension ratios (which is unlikely considering the disappearance of the isocyanate peak of the PU IR spectrum). This could also point to the possible predominance of TEA for these effects.

The second attempt at solving this issue involves an acid other than ascorbic acid. Indeed, the addition of ascorbic acid into the polymer was shown to have a beneficial effect, at least until the coating dried. Since oxidation as an interaction was ruled out, it was hypothesized that its high acidity allowed for the protonation of the leftover EDA and TEA molecules, which were then no longer able to interact with the iron centres due to the

delocalization of their electronic density into the newly formed N-H bonds. DMPA (Dimethylol propionic acid) was selected for trials because of its correspondence of pKa with ascorbic acid (4.68 and 4.17 respectively). Also, due to its presence in the polyurethane chains, it was hypothesized that it might work better than ascorbic acid.

So, DMPA was introduced in the hybrid material at the same time as the SCO compound. It returned results similar than with ascorbic acid for the wet coating. However, when the coating dried, DMPA seemed to maintain the beneficial effect and the deleterious interaction was thwarted (SCO behaviour was retained, as depicted on Figure 57). This confirmed that acidity was indeed the property of interest, which further confirmed the EDA/TEA coordination theory.

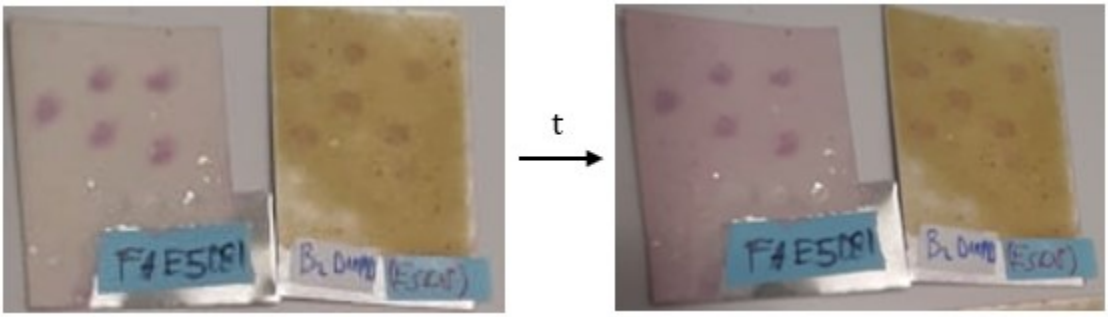

Figure 57 [Fe(NH$_2$trz)$_3$]Br$_2$·nH$_2$O coating with DMPA (on the right of images), hysteresis at room temperature is better conserved compared to the -DMPA coating (FAE5D81) (purple dots demonstrate the piezochromism of the coatings)

However, polyurethane coatings work best when they are neutral, so the addition of acid produces worse mechanical and chemical resistance properties, as well as a yellowing of the polymer. Moreover, the quantity of DMPA to add are small (< 1mg for a gram of hybrid material), which leaves a lot of room for experimental variation.

To avoid this problem, an attempt was made to introduce DMPA in the synthesis of the SCO compound, instead of during synthesis of the hybrid SCO/PU. This was done by replacing ascorbic acid with DMPA. Indeed, as a reminder, ascorbic acid is added to avoid oxidation of iron centres during the synthesis. Although the mode of action of ascorbic acid is complex, the property that makes this possible is once again acidity. [98] DMPA could then have the same effect, with the bonus of maintaining SCO properties in the hybrid. This attempt was successful, with the obtention of better coating performances (although still not ideal) and less experimental variability (Figure 58).

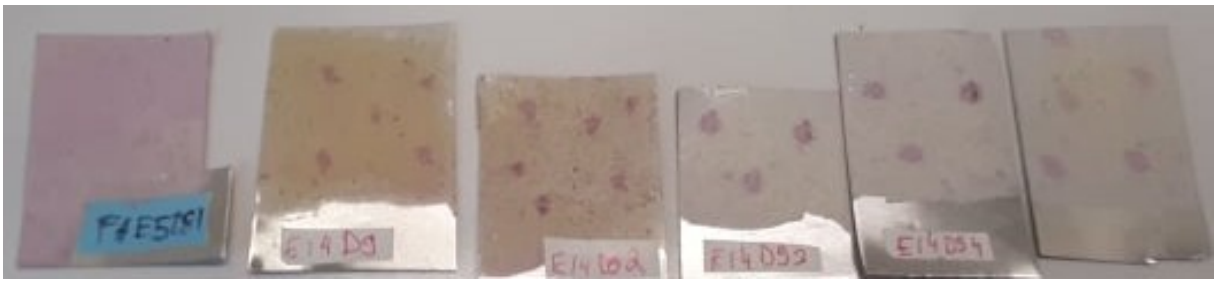

Figure 58 Comparison of thermochromic properties of $[Fe(NH_2trz)_3]Br_2 \cdot nH_2O$ coatings -DMPA in the SCO synthesis (coating 1 from left to right), +DMPA into synthesis (coatings 2-3), +DMPA + TiO_2 (coatings 4-6). Purple dots demonstrate the piezochromism of these compounds. Coating 1 has a thinner hysteresis and partially reverts to the LS state (purple) at room temperature.

To completely avoid the addition of any compounds in the SCO/PU hybrid, the fourth solution tested was to replace the chain extender (EDA) with a molecule that would not interact with the SCO compound (WBPU **D13,** see Table 1). In addition, the amount of TEA added into the synthesis of the polyurethane dispersion was reduced to 90% neutralization instead of 100%. As a replacement for EDA, 1,4-Butanediol (BDL) was selected due to its similarities with EDA, with simply the amine functions replaced by alcohol functions. It is also a known chain extender. [99]

This attempt was successful, with the obtention of pristine white coatings (Figure 59). It is relevant to note that this completely confirms the role of EDA and TEA in the degradation of the SCO compound, and that it is not the result of oxidation of the iron centres.

Figure 59 Result with Butanediol PU polymer for $[Fe(NH_2trz)_3]Br_2 \cdot nH_2O$

Finally, TEA had to be dealt with. This was more complicated, since it is difficult to find non-aminated bases of similar pKa which return good coating properties. Indeed, TEA is almost exclusively used in literature. [61] A few articles have reported the use of NaOH as neutralizer, returning worse coating properties (mainly adhesive properties). [100] A test was done (WBPU **D14**, see Table 1), and the obtained coating did indeed have worse coating properties, but the SCO compound also reacted strongly with the NaOH, possibly via coordination of OH^-. This option was then discarded. Another possible solution is to replace the base neutralizer with an acid neutralizer such as acetic acid. Obviously, this would then require using a base as internal emulsifier instead of DMPA. Once again, it is difficult to find

a non-aminated base which returns good coating properties. Still, it is interesting to test this option, since it is possible that the amine function locked inside the polymer chain would be unable to interact with the Fe^{II} centres. For this purpose, MDEA (N-methyl diethanolamine) was selected.

Unfortunately, poor results were obtained and a definite interaction with the SCO compound was observed, very similar to the EDA/TEA interactions. Since in this case the only aminated compound present (MDEA) is inside the polymer chain, it can be concluded that the SCO compound is indeed capable of interacting with amines inside the polymer, and not just free molecules.

To conclude, EDA and TEA were shown to have an effect towards $[Fe(NH_2trz)_3]Br_2$, and while a suitable replacement for EDA was found in 1,4-Butanediol, no replacement was found for TEA. However, these interactions indicate that when combining 4-amino-1,2,4-triazole SCO compounds with polyurethane (and perhaps other polymers), aminated compounds should be avoided.

To better understand the interactions between the SCO compound and the polymer, SEM and AFM imaging and DSC measurements of the prepared coatings have been conducted.

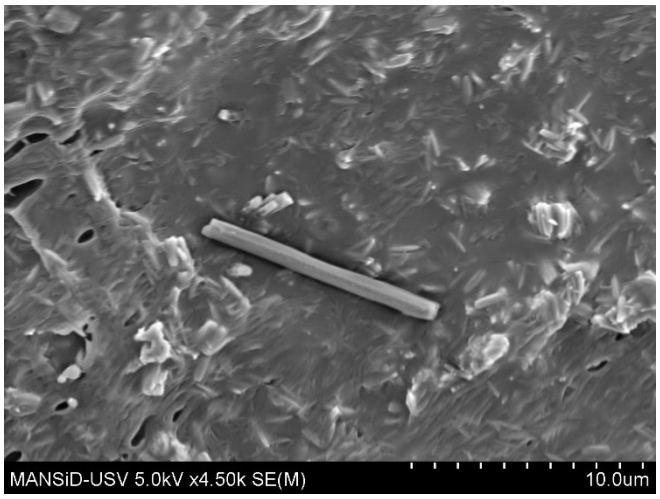

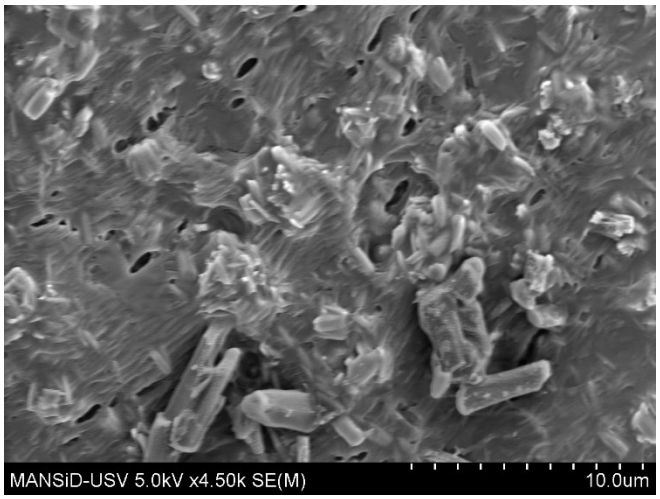

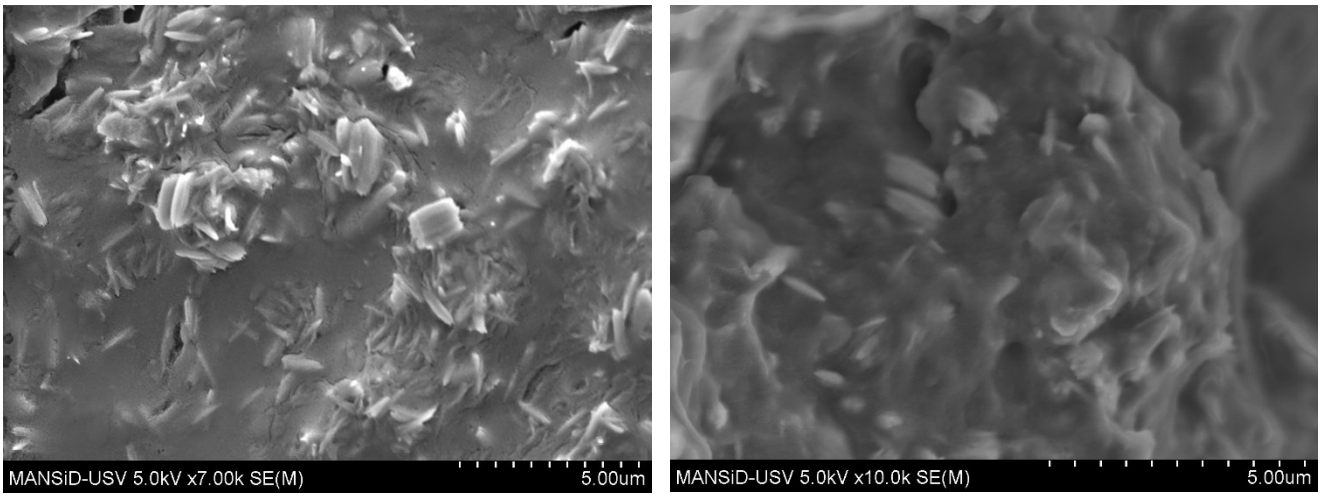

Figure 60 Scanning electron microscopy images of the [Fe(NH$_2$trz)$_3$]Br$_2$-PU hybrid

The scanning electron microscopy images on Figure 60 reveal an unstructured material comprised of mostly rice-shaped SCO particles with a mean length of about 1.22 µm, dispersed in the polyurethane polymer, with a sporadic dispersion of bigger particles up to 5-10 µm long. This distribution of particle size (visible on Figure 68) is very similar to the one described in the only article in the literature describing an aminotriazole compound [Fe(NH$_2$trz)$_3$](BF$_4$)$_2$ in a polyurethane matrix (polyurethane D6). [50] This is in stark contrast with the previous finding on the simple polyurethane polymer which displayed semi-crystalline spherulites structures. Thus, it can be concluded that the presence of [Fe(NH$_2$trz)$_3$]Br$_2$·nH$_2$O disrupts the micro-ordering of the polymeric chains. This could be expected to worsen the mechanical properties of the hybrid material. Even though no rigorous study of the mechanical properties has been conducted in this work, their worsening can indeed already be appreciated, with the observation that the hybrid material is less hard and less rigid.

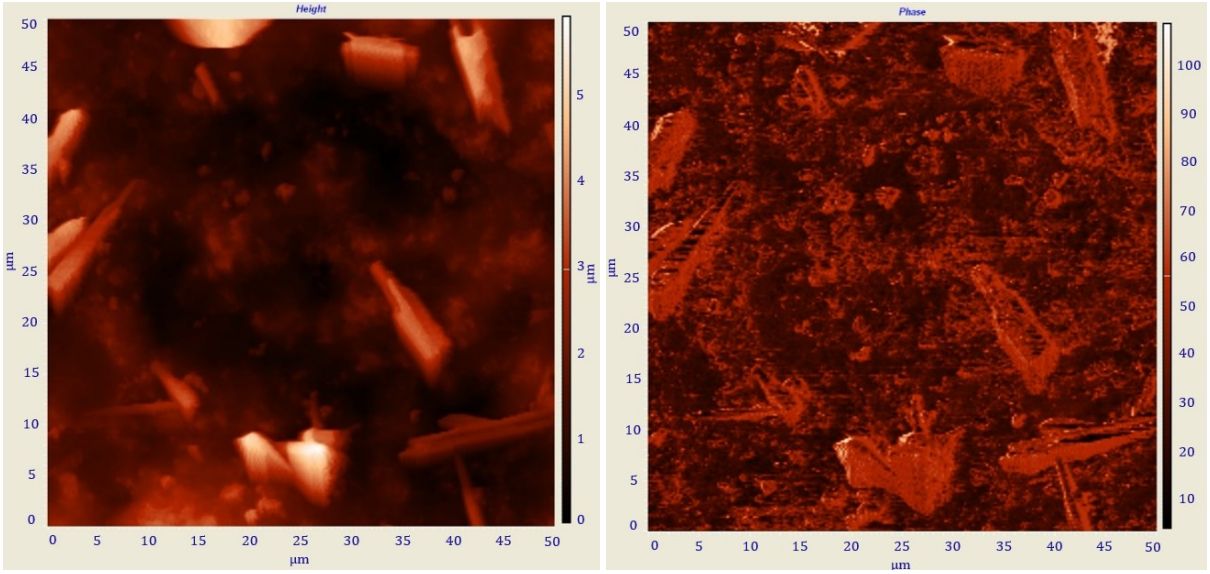

Figure 61 AFM tapping mode Left) height and Right) phase images of the [Fe(NH$_2$trz)$_3$]Br$_2$-PU hybrid

AFM height images on the same coating (Figure 61) once again reveal the same particles as in SEM. AFM phase images also indicate a loss of structure in the polymer, with the disappearance of the contrasted structures which were visible on Figure 27.

DSC measurements of the prepared coatings were conducted. However, since the melting temperature of the polymer soft segment more or less corresponded to the SCO transition temperatures (and the SCO compound makes up only about 15% of the total mass), it is difficult to separate the polymer SS melting and the SCO behaviour. Still, the DSC measurement can be found in Annex 17.10. One interesting comment is that the presence of the SCO compound does seem to affect the melting and crystallization temperatures of the soft segment, as well as reducing the heat of melting $\Delta H_m^{ss} = -55.18\, J.g^{-1}$ and crystallization $\Delta H_c^{ss} = 48.9\, J.g^{-1}$. This indeed supports the hypothesis that the SCO compound reduces the crystallinity of the SS (PEG) microdomains of the polymer (especially since $\Delta H_{LS \rightarrow HS}$ might be confounded in the ΔH_m^{ss} presented above), resulting in de-structurization.

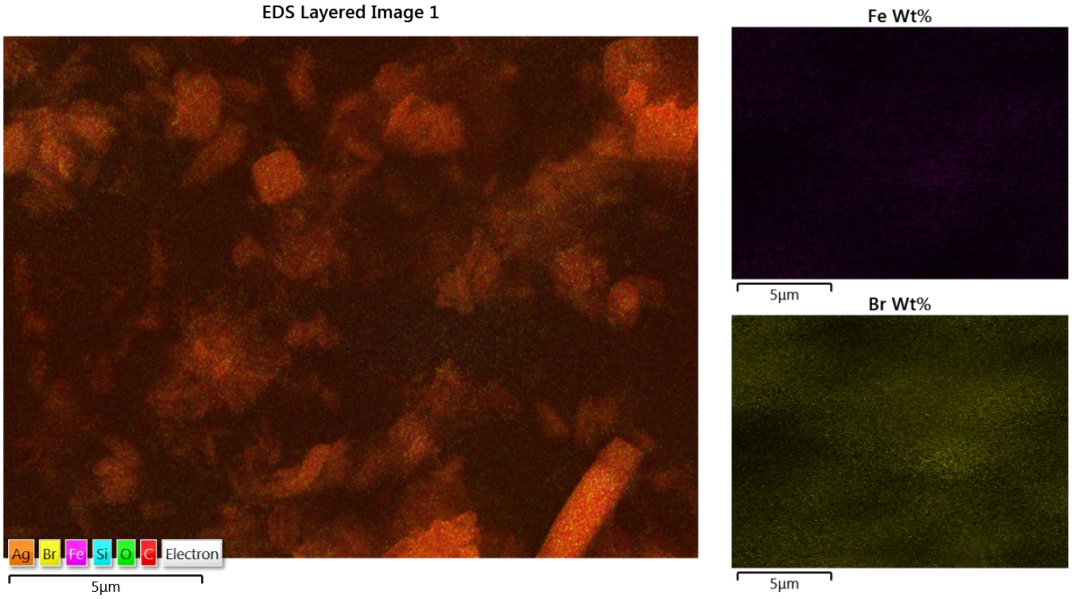

Figure 62 Left) EDX layered elemental images Right) EDX Fe and Br elemental images of the [Fe(NH₂trz)₃]Br₂·nH₂O-PU coating surface

The final analysis conducted on this hybrid material are Energy Dispersive X-Ray analyses. Multiple images were taken, which can be found on Annex 17.11, and only one image will be presented here (Figure 62). As you can see on Figure 62, the Fe and Br content is very poorly correlated to the SCO particles. This could mean two things: it is possible that the EDX analysis (which can probe up to microns deep) images particles which can be found deeper than the particles visible on the surface. The second possibility is that there would be partial dissolution of the SCO particles (which is possible since in the liquid state the polymer is comprised of 60-70 w% H_2O), freeing either singular polymeric chains or Fe^{II} ions. This

idea is supported by the appearance of the rice-shaped particles as well as their variation in size according to the polymer composition (an aspect which is explored later, see Figure 68).

The weight percentage of the different elements found in the polymer are displayed on Figure 63. In these, all elements are expected, except for silicon, which is presumed to be a surface contaminant. Silver comes from the conducting layer deposited to image the polymer in SEM.

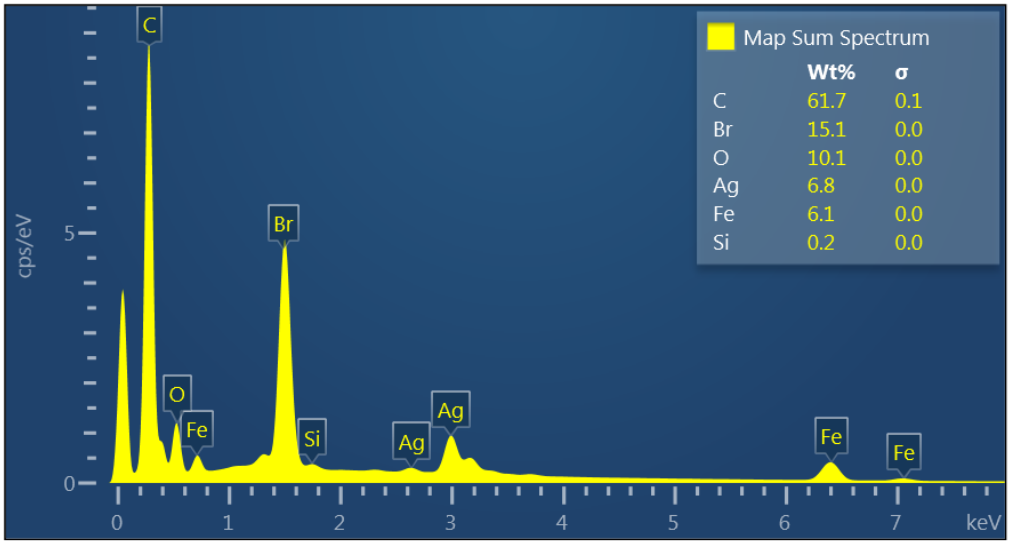

Figure 63 EDX Elemental analysis of $[Fe(NH_2trz)_3]Br_2 \cdot nH_2O$-PU coating surface

However, some of these percentages present a discrepancy from the theoretical value. Indeed, looking at $[Fe(NH_2trz)_3]Br_2 \cdot nH_2O$, the theoretical Br w% should be 2.856 times greater than Fe. However, here EDX results provide a ratio $\frac{w\%_{Br}}{w\%_{Fe}} = \frac{15.1}{6.1} = 2.475$. Thus, there seems to be a lack of Br (or excess of Fe) which cannot be explained by a lack of accuracy of the technique, as the discrepancy is too large.

Nevertheless, one conclusion that can be drawn from the hybrid characterization is that the observed macroscopic worsening of the polymer mechanical properties, upon incorporation of $[Fe(NH_2trz)_3]Br_2 \cdot nH_2O$, can be attributed to the microscopic de-structurization of the semi-crystalline ordering inside the polymer. Since these arrangements arise from weak interchain interactions (e.g. Van der Waals interactions between PEG chains), this hypothesis is reasonable. Knowing this, one possible solution to improve the mechanical properties is to introduce covalent interchain interactions to improve the cohesion of the polymer network. One possibility that has already been described in the literature is to use UV-cured polymers. [61,61,64,65,101] The idea is to replace the common chain extender (which is usually bivalent) by a UV-responsive trivalent molecule. The molecule that was selected for trials in this work is Pentaerythritol triacrylate (PETA). Upon exposure to UV light (and addition of a photoinitiator, Irgacure 2959), the production of radicals on the

acrylate functions at the end of the polymer chains induce a covalent crosslinking, which usually results in improved mechanical properties. A basic scheme illustrating this principle can be found on Figure 64.

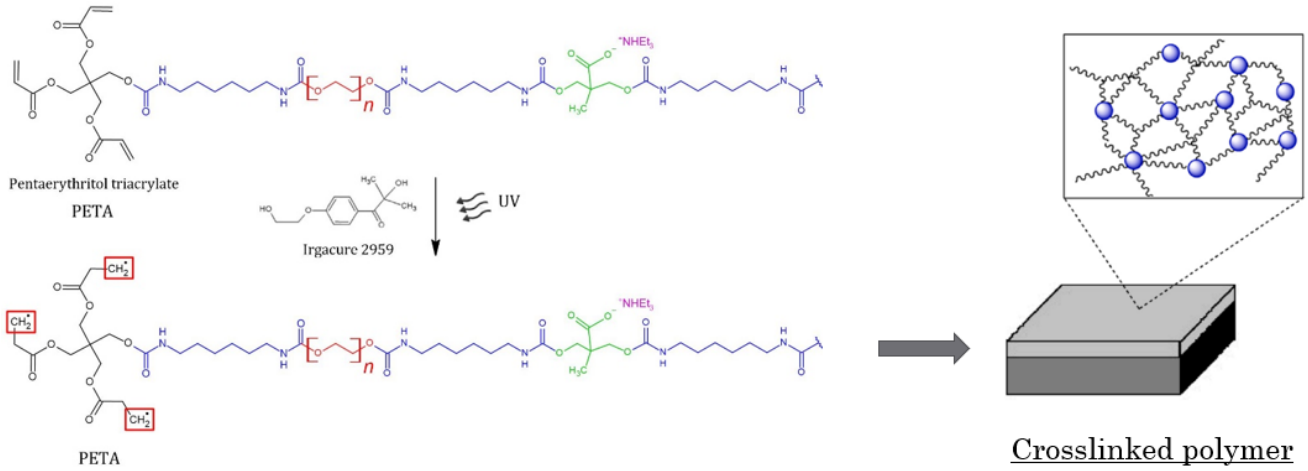

Figure 64 Illustration of the principle of UV-cured polyurethane coatings

In accordance with the literature, the photoinitiator quantity introduced equated to 3% of the solid weight inside the aqueous polymer dispersion. The PETA quantity was selected to completely react with 100% of the excess isocyanate groups (since NCO/OH > 1). The inclusion of PETA at the end of the polymer chains was confirmed since the typical isocyanate IR peak of 2270 cm^{-1} is not present on the FTIR measurement, visible on Figure 65. UV-curing was realized on coatings for 1h and 24h, to see the effect of UV exposure. There was no significant mechanical difference between the two exposure times, and a significant discoloring was observed with longer exposures (Figure 65), so 1h exposure was considered sufficient. This discoloring might not indicate a degradation or interaction of the SCO compound, since yellowing of polyurethanes under UV light is a known phenomenon. [102]

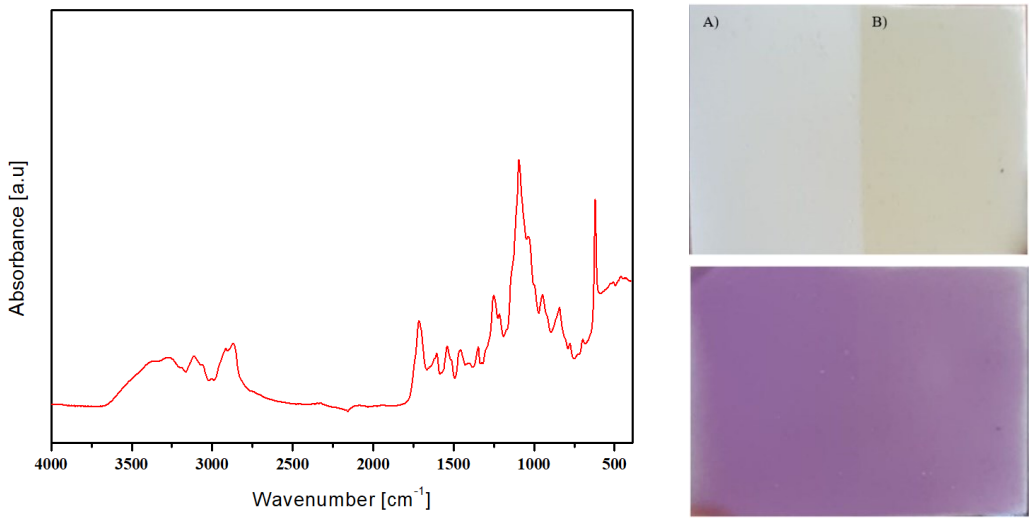

Figure 65 Left) FTIR spectrum of the UV-Coating + SCO compound Right) Room temperature photographs of UV-Coating- SCO compound hybrid in the LS state and in the HS state (A = no exposure, B = under UV lamp for 24h)

While no extended mechanical property studies were realized on the coatings, a simple pencil scratch test was conducted to assess the hardness of the coatings pre- and post-curing. These measurements were conducted following the ASTM D3363 standard for pencil hardness tests. [103] The hardness scale is provided on Figure 66.

Figure 66 Pencil hardness scale for determining the hardness of coatings

The result returned a hardness of 3-4B pre-curing and H-2H post curing, which indicates a clear improvement, and that UV-cured polymers potentially represent a solution to provide application-ready SCO-PU coatings. Moreover, the coatings displayed thermochromic bistability at room temperature. Indeed, the coating on Figure 65 LS and HS state were both photographed at room temperature. However, attempt at showing piezochromic properties of these coatings failed, which is unexpected if the room temperature is indeed within the thermal hysteresis of the compound. One possibility is that the polymer rigidity increase due to crosslinking was too great, making it no longer possible to switch spin state via hand-applied pressure. It is possible that the polymer bears too much of the load applied, resulting in the need for higher pressures to obtain a piezochromic effect. This is interesting since it means that in a hybrid material, the threshold pressure for spin state switch will not only depend on the thermodynamics of the SCO compound but also the mechanical properties of the polymer, which opens development opportunities.

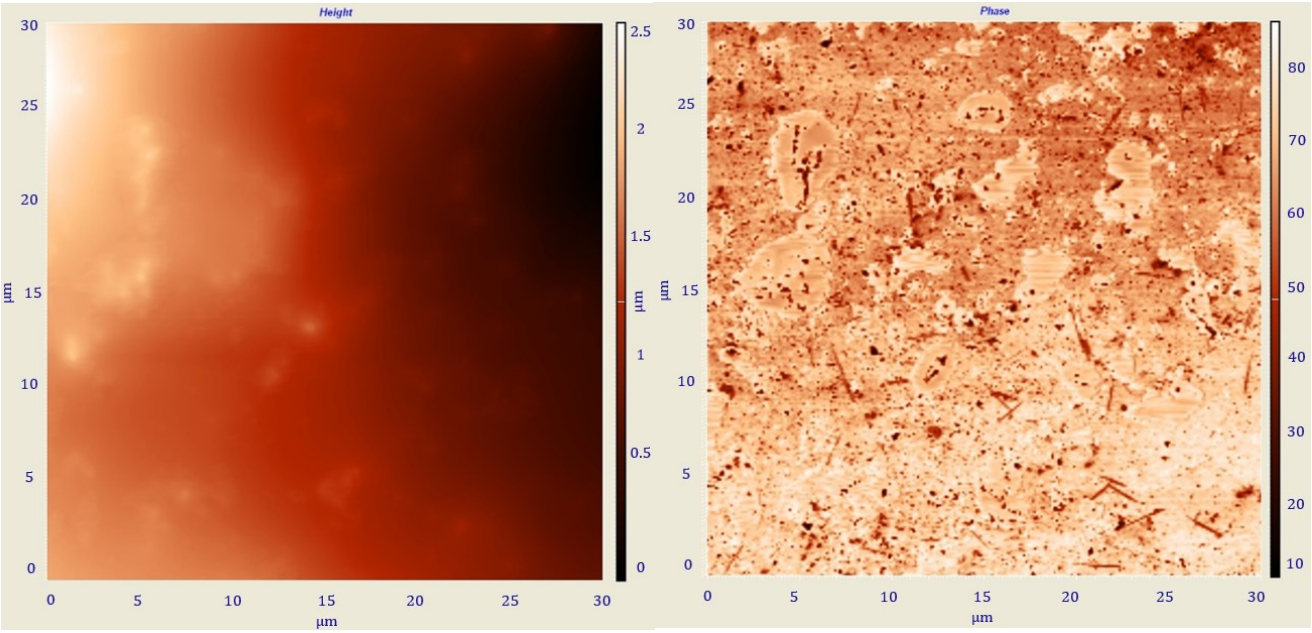

Figure 67 AFM tapping images of [Fe(NH$_2$trz)$_3$]Br$_2$-UVPU in Left) Height mode Right) Phase mode

Once again, AFM height and phase images in tapping mode of the UV-PU-SCO hybrid were recorded. While the phase image on Figure 67 once again reveals the rice-shaped particles under the surface of the polymer, it shows no discernable structure, and the height images reveal a very smooth surface. So, once again $[Fe(NH_2trz)_3]Br_2 \cdot nH_2O$ seems to perturb the polymer semi-crystalline structure. All the recorded images can be found in Annex 17.12.

Another attempt at trying to improve the mechanical properties of the polymer was done by simply reducing the PEG chain length (from 1450g/mol to 600 g/mol) and increasing the NCO/OH ratio, which essentially amounts to increasing the amount of hard segment (diisocyanate) in the polymer, thereby hopefully increasing the rigidity of the polymer (**D15**: see Table 1). This indeed produced an improvement in the mechanical properties. However, the change in chemical environment seemed to have greatly affected the behaviour of the SCO compound. To investigate the reason for this change, scanning electron microscopy images as well as magnetic measurements were carried out.

The SEM images, visible on Figure 69, revealed a surface like that of Figure 60, although the SCO particles seemed to protrude less from the surface. Also, rather than only rice-shaped particles, multiple morphologies can be observed, for example sheets and cubic particles. All the images can be found on Annex 17.13.

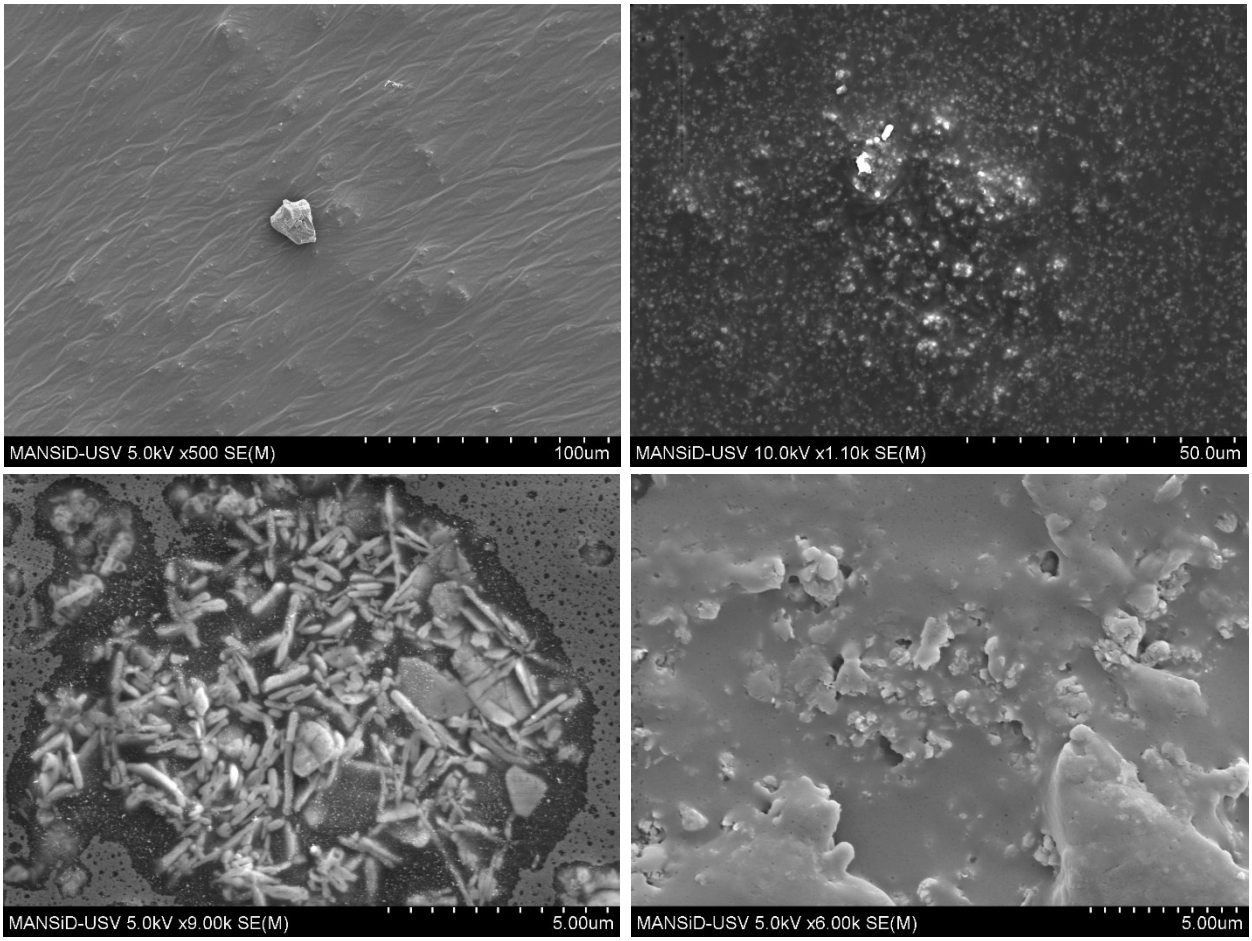

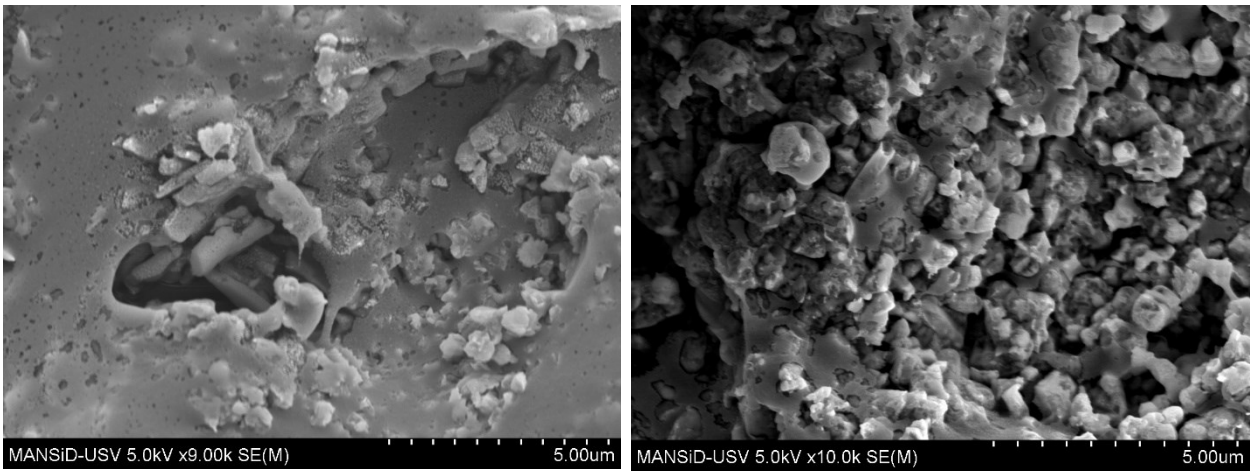

Figure 69 SEM images of the [Fe(NH$_2$trz)$_3$]Br$_2$-PU (600g/mol) hybrid

The SEM images allowed to estimate the SCO particle size distribution, which is displayed on Figure 68 for both the short- and long-PEG polymers. These distributions clearly show that the SCO particles seem to be smaller in the short-PEG polymer (D15). It is believed that this is reflected in the SCO magnetic properties, which are displayed on the same Figure 68. Indeed, as already mentioned in Section 6.2, reducing SCO particles size below the micrometer range (nanoparticles) usually results in a loss of cooperativity accompanied by a shortening of the hysteresis width, which is observed in this case. This thinning is also

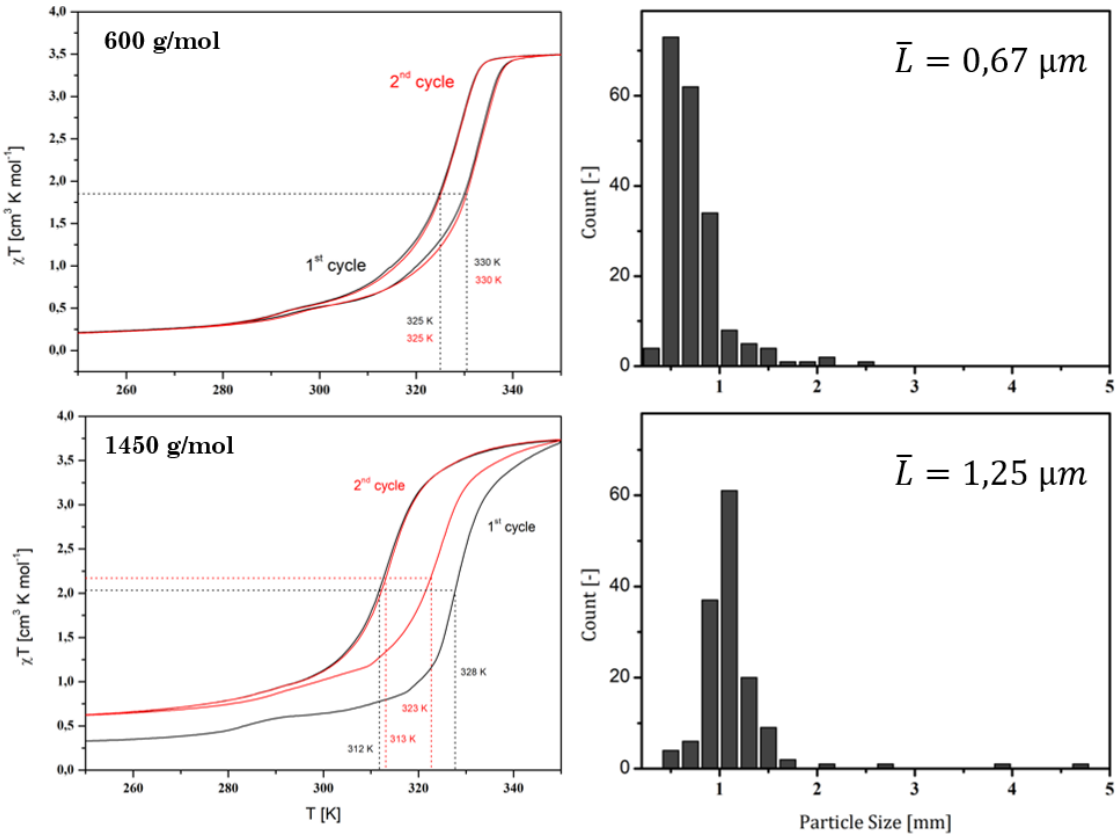

Figure 68 Left) SQUID magnetic measurements for the [Fe(NH$_2$trz)$_3$]Br$_2$-PU hybrid between -10°C and 80°C at a rate of 2°C/min for the two different polymers Right) Particle size distribution for the two different polymers

consistent for $[Fe(NH_2trz)_3]Br_2$, according to the literature. [83] It is interesting to remark that in **D15**, although the SCO particles are smaller (from which we could infer a reduced chain length), the residual HS fraction at low temperatures is smaller than in other softer polymers. This could be explained if the polymer exerted a constraint (called positive pressure effect) on the SCO compound, thereby disfavoring the HS state, an effect which has been reported when SCO compounds are inserted into rigid structures. [104]

12.2 Fe(pyrazine)[Fe(CN)$_5$NO]-PU hybrid : Second trials

It is interesting to note that, contrary to the triazole compounds tested previously, Fe(pyrazine)[Fe(CN)$_5$NO] is quite stable in the PU matrix and retains its SCO properties. As is visible on Figure 70, clear thermochromic properties are displayed by the hybrid SCO-PU coating.

It is also interesting to note that Fe(pyrazine)[Fe(CN)$_5$NO] does not disturb the semi-crystalline spherulitic structures that were visible on the simple polyurethane coating. Indeed, AFM height measurements in tapping mode of the SCO-PU hybrid visible on Figure 71 reveal the microscopic ordering with spherulites of mean diameter of 20 µm.

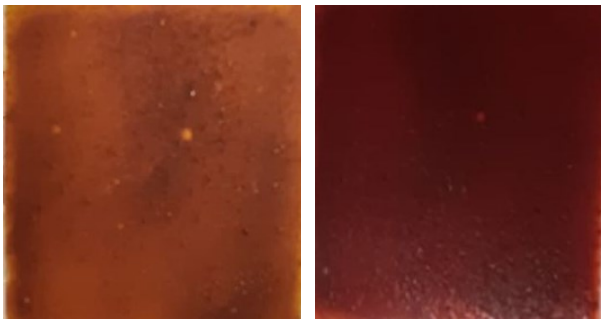

Figure 70 Fe(pyrazine)[Fe(CN)$_5$NO]-PU hybrid, in the HS state (left) and LS state (right)

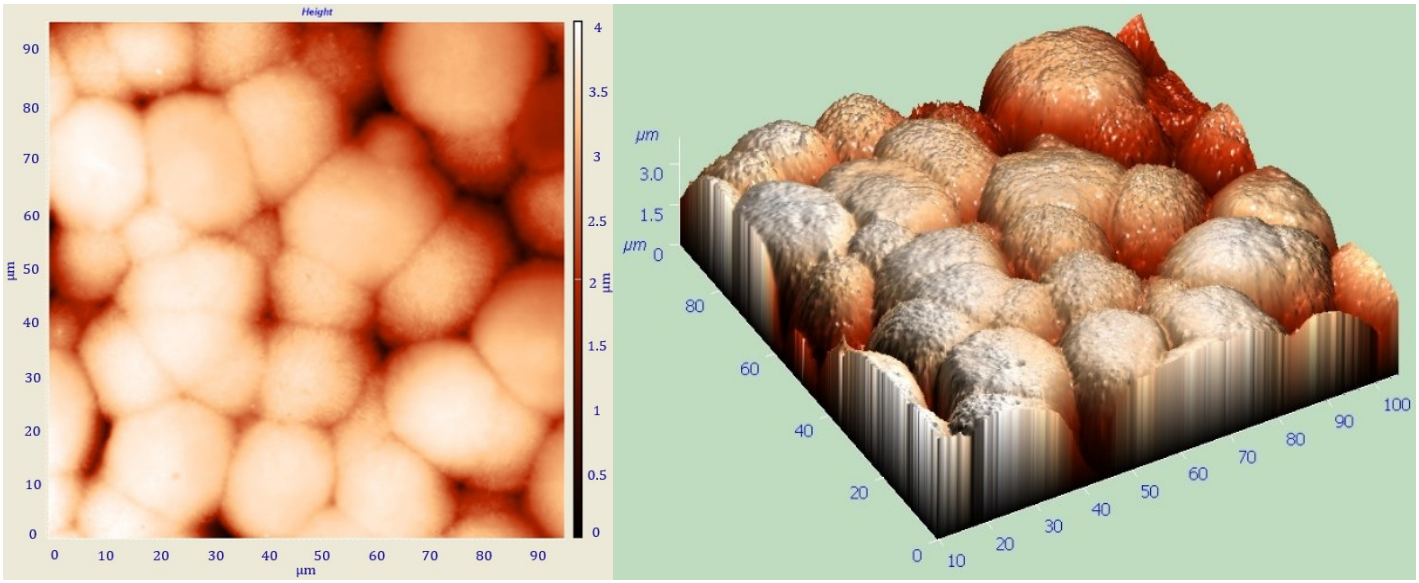

Figure 71 AFM tapping mode height images of the Fe(pyrazine)[Fe(CN)$_5$NO]-PU hybrid Left) 2D Right) 3D

A zoom on part of this image shows how well preserved these structures are, with even the individual crystalline lamellae being observable (Figure 72). All the recorded images can be found in Annex 17.14.

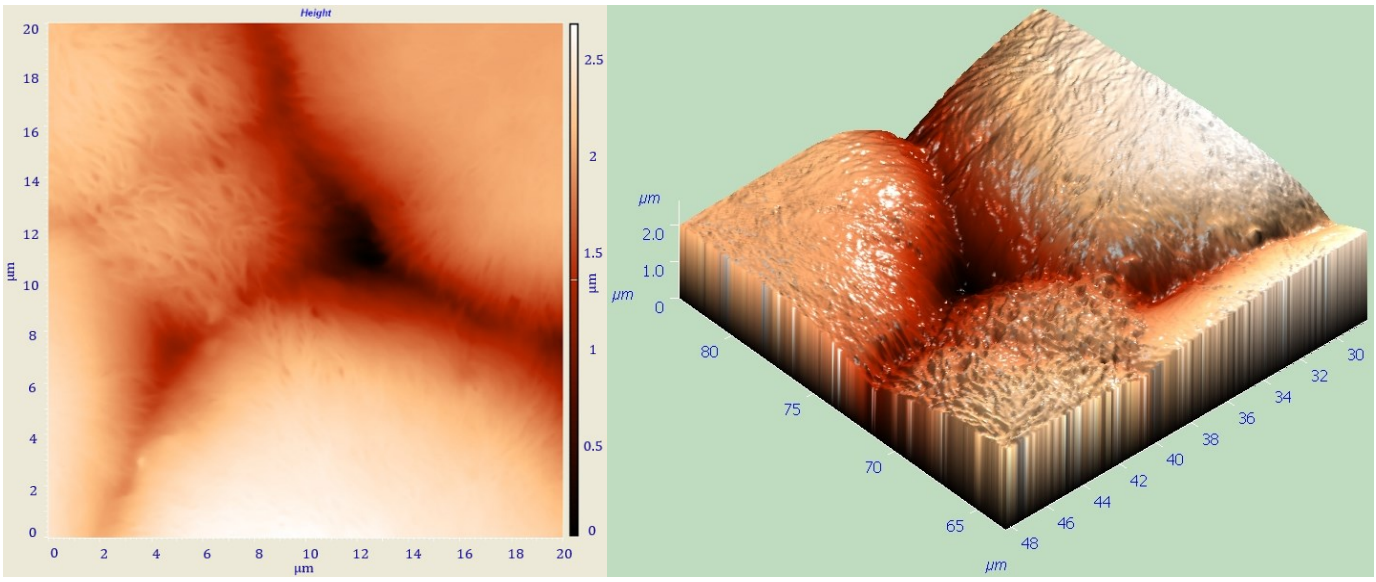

Figure 72 AFM tapping mode height images of the Fe(pyrazine)[Fe(CN)$_5$NO]-PU hybrid Left) 2D Right) 3D

The piezochromic properties of these coatings were not assessable in this work for two reasons. The thermal region of bistability meant that any trials would have to be done at low temperatures (at a maximum of 0°C) and the thermodynamics of the sample indicated that a pressure of 46 MPa would have been required, which was not feasible with our makeshift setup.

12.3 Fe(pyrazine)[Fe(CN)$_5$NO]- [Fe(NH$_2$trz)$_3$]Br$_2$-PU Hybrid

The successful Fe(pyrazine)[Fe(CN)$_5$NO]-PU hybridization as well as the compatibility of [Fe(NH$_2$trz)$_3$]Br$_2$·nH$_2$O in the polymer prompted an evaluation of the feasibility of working with these two families together, to develop a technology not only capable of determining the pressure of a specific impact, but also the temperature at which that impact occurred. Indeed, while Fe(pyrazine)[Fe(CN)$_5$NO] and [Fe(NH$_2$trz)$_3$]Br$_2$·nH$_2$O share no (or just a very small) overlap of their hysteresis, Fe(pyrazine)[Fe(CN)$_5$NO] is very similar to many Hofmann-type MOFs with SCO properties [105–113], with some having room temperature properties (overlapping hysteresis with [Fe(NH$_2$trz)$_3$]Br$_2$·nH$_2$O)[108,112–114]. Notably, the very similar (but much more expensive, limiting its use in this work) compound [Fe(pyrazine)Pt(CN)$_4$] presents an almost identical hysteretic SCO behaviour as [Fe(NH$_2$trz)$_3$]Br$_2$·nH$_2$O, as can be seen on Figure 73, and the same color pattern as Fe(pyrazine)[Fe(CN)$_5$NO].

Thus, it was decided to use Fe(pyrazine)[Fe(CN)$_5$NO] as a representative compound of a bigger family in conjunction with [Fe(NH$_2$trz)$_3$]Br$_2$·nH$_2$O in a single coating, to evaluate whether the individual transitions of the compounds were discernable.

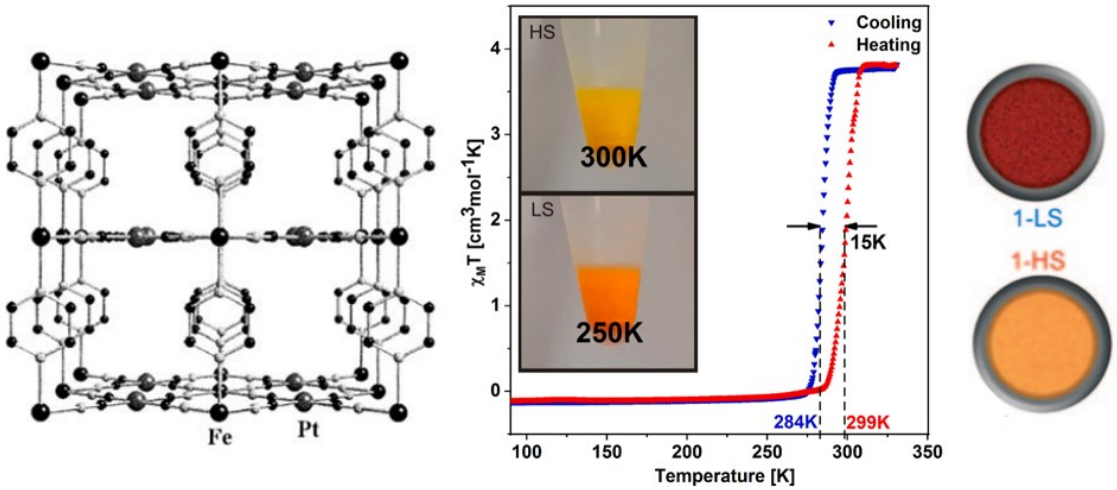

Figure 73 Left) Structure of [Fe(pyrazine)Pt(CN)$_4$], revealing the similarities to Fe(pyrazine)[Fe(CN)$_5$NO], Middle) SCO magnetic measurements for [Fe(pyrazine)Pt(CN)$_4$], Right) LS and HS color change for [Fe(pyrazine)Pt(CN)$_4$] [105,108,110,112]

Indeed, it is well known and has been demonstrated in this work that the SCO phenomenon is dependent on pressure but also temperature. So, one can attempt at estimating the pressure felt by a SCO compound by mapping the transition, but that estimate will only be precise if one knows the precise temperature at which the pressure was applied. In contrast, when using two SCO compounds with different properties (for example different $\frac{\Delta V_{HS\rightarrow LS}}{\Delta S_{HS\rightarrow LS}}$ parameters), the set of final conditions (x% HS→LS state switch for SCO-1 and y% for SCO-2) after an impact event provides a unique (P,T) solution. In other words, one can predict P using one SCO compound **only** by making an assumption on T, while using two SCO compounds leaves no room for speculation for both P and T. For further information on this, the concept paper from Jureschi, Garcia, Rotaru *et al.* [18] (which treats gradual SCO compounds, not hysteretic) as well as the article from Blanco-Gutierrez *et al.* [6] (which provides a theoretical demonstration by modelling fictitious piezochromic compounds) are interesting reads.

However, this is only feasible if the actual spin state switch information of the two compounds can be separated. This is the reason why such technology is not possible when using two triazole-family SCO compounds, since their HS and LS states have the same colour and are indistinguishable. However, since the states from the [Fe(NH$_2$trz)$_3$]Br$_2$·nH$_2$O and Fe(pyrazine)[Fe(CN)$_5$NO] families are of different colour, it should be possible to distinguish them. Multiple tests were conducted, the best of which consisted of grinding a mixture of [Fe(NH$_2$trz)$_3$]Br$_2$·nH$_2$O and Fe(pyrazine)[Fe(CN)$_5$NO] powders together at an 80/20 ratio, then incorporating it in the polyurethane polymer to produce a coating. As is visible on Figure

74, the LS-LS, HS-LS and HS-HS states are all distinguishable. More precise study of such coatings (recording absorption spectra for example) as well as measurements based on pressure would provide a more precise overview, but it can already be said that this attempt was at least successful at demonstrating the potential of such SCO-SCO-PU hybrids for simultaneous P and T determination.

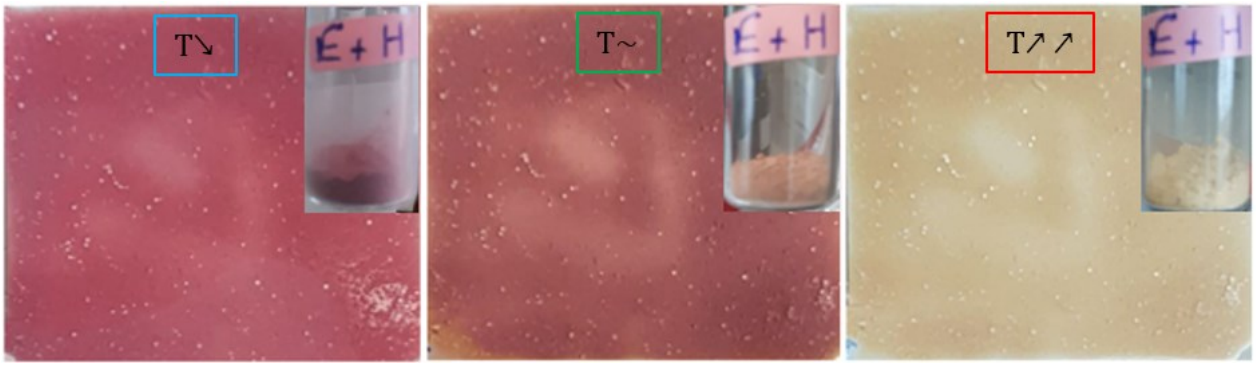

Figure 74 $[Fe(NH_2trz)_3]Br_2 \cdot nH_2O$/Fe(pyrazine)$[Fe(CN)_5NO]$/PU hybrid in the LS/LS state (Left), LS/HS state (Middle), HS/HS state (Right) Inset images correspond to the same states for the power mixture

12.4 Hybrid material: conclusion

To conclude the assessment of a SCO-PU material, both thermochromic and piezochromic properties of these have been demonstrated at room temperature. This assessment showed that the morphology of SCO particles as well as their properties are dependent on the polymer chemical composition. The triazole SCO compound family, one of the most studied for practical applications, showed a few shortcomings, mainly interactions with aminated compound present as part of the polyurethane and a negative effect on the microscopic ordering of the polymer. Although, it has been shown in this work that most of these shortcomings may be corrected by finding alternative PU formulations (without amines) and ways to improve the mechanical properties (e.g. UV-curing). Preliminary attempts at using UV-cured polymers seem to confirm that the mechanical properties of the polymer will also affect the SCO phenomenon, which can provide further tuning. Moreover, the study of Fe(pyrazine)$[Fe(CN)_5NO]$-PU coatings revealed that these shortcomings are not incumbent on all SCO compounds, and that pluri-SCO hybrid materials, which have (to my knowledge) never been attempted in the literature, are an exciting opportunity to obtain different aesthetics (colors) for practical applications and most importantly, to develop materials capable of storing information about both pressure and temperature at the same time.

13. Piezochromic properties : Machine learning

In today's world, where the complexity as well as the sheer number of tasks involved in a technology is ever increasing, automation is shaping up to be a vital component in future technologies. With that in mind, the following section explores the utilization of the developed piezochromic properties of our coatings to train different machine learning algorithms, with the aim of providing proof of concepts for **impact detection** automation and **impact pressure** determination based on the response of the SCO-PU coatings. The $[Fe(NH_2trz)_3]Br_2 \cdot nH_2O$-PU hybrids were used for this study because of their room temperature properties and their low threshold pressure, which rendered testing easier.

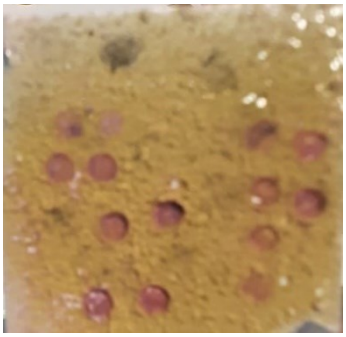

Figure 75 Coating used for the different machine learning models

Firstly, to develop an impact detection algorithm, several classification models were trained on the RGB data of the image displayed on Figure 75, on which multiple spots were affected by different pressure impacts, resulting in a color change to purple.

Secondly, to evaluate the pressure prediction power of such a device, the same image was used, where specific pressures ranging from 0 to 15 MPa were applied in certain regions of the coating, leading to a switch from HS to LS state, the intensity of which depended on the pressure. The tested pressures were limited since a makeshift pressure application device was used. Then, RGB color intensity were recorded for every pressure test, and have been used to develop multiple prediction models.

13.1 Impact detection

For impact detection, the Python "OpenCV" package was used to read and treat image data in conjunction with the R "caret" package to train different machine learning algorithm on that data. [115,116] The Python and R code used in this section can be found in Annex 17.15. The data used to evaluate the model performance is comprised of images of three coatings of different composition, to evaluate the model versatility.

Three different machine learning algorithms were tested: "k-NN", "Random Forest" and "Logistic Classification". Additionally, an ensemble was constructed by returning for each pixel the prediction of the majority of the three models. A summary of the results of the three models as well as the ensemble is displayed on Figure 76, for the three different coatings displayed on Figure 77. Based on these results, since the ensemble of the three models returns the best overall accuracy, it was selected to attempt to map pressure impacts.

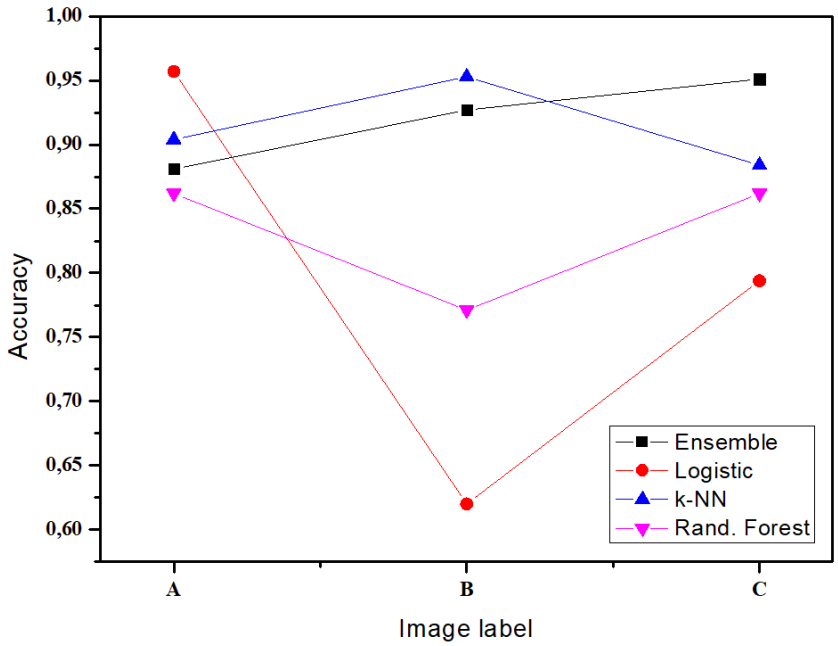

Figure 76 Accuracy of predicted impacts for 3 machine learning models and an ensemble of these 3 models, for 3 different images (A,B,C) labelled as described on Figure 77

It is interesting to note that the algorithm was trained on a separate coating (Figure 75) and tested on coatings with different compositions (Figure 77) but returned mostly accurate predictions. However, Figure 77a clearly shows an artifact at the center of the image (which could be due to a gradient of luminosity) while Figure 77c only has partial recognition, which means the algorithm can still see some improvement. Since the model was trained on a single image, it is possible that simply feeding it more training data would be enough to drastically improve the results.

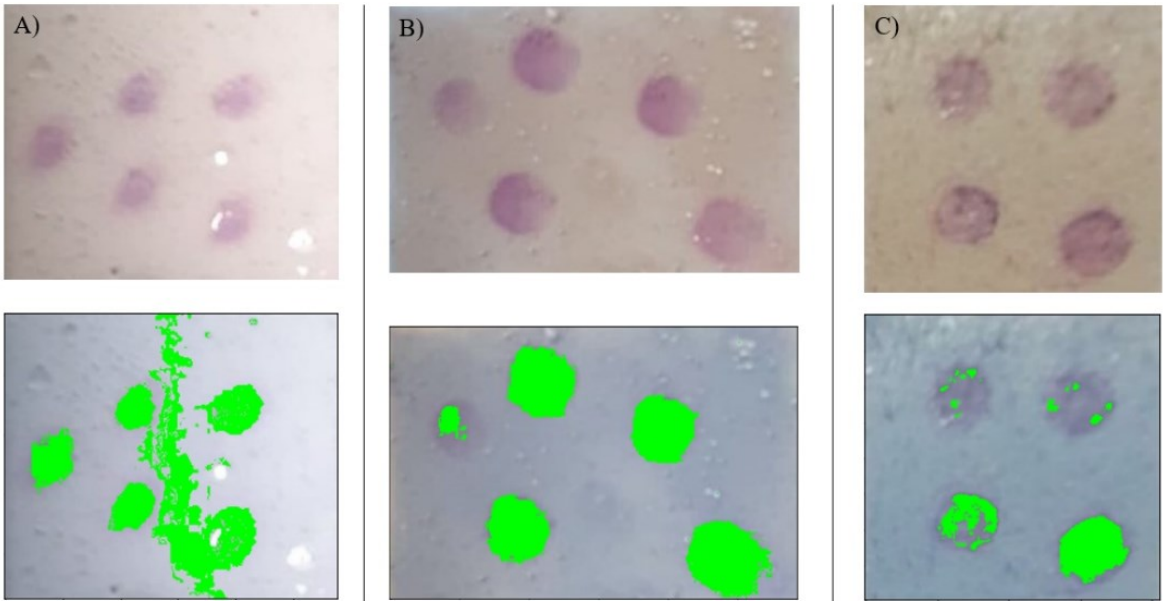

Figure 77 Impact detection for $[Fe(NH_2trz)_3]Br_2 \cdot nH_2O$/PU coatings based on the ensemble model trained on RGB data for A) SCO + TiO_2 B) SCO C) SCO-Fluorescence coatings. Top: different coatings with piezochromic properties displayed. Bottom: predictions

In order to understand the reason for the appearance of artifacts, it is interesting to investigate in more detail the decision-making reasoning of the algorithm. Indeed, rather than trying to predict impact pressure by classification into a binary system (impact or no impact), it is instead possible to map the likeliness that an impact did occur as predicted by the same models. The best results, obtained using a k-NN model, are displayed on Figure 78. By looking at Figure 78a, it is evident that the right half of the image is described as having a higher probability of having been impacted. When looking at Figure 77a, one can see that the right side of the image is more lit. Thus, it is reasonable to conclude that the artifacts are due to the influence of lighting on the RGB values of pixels.

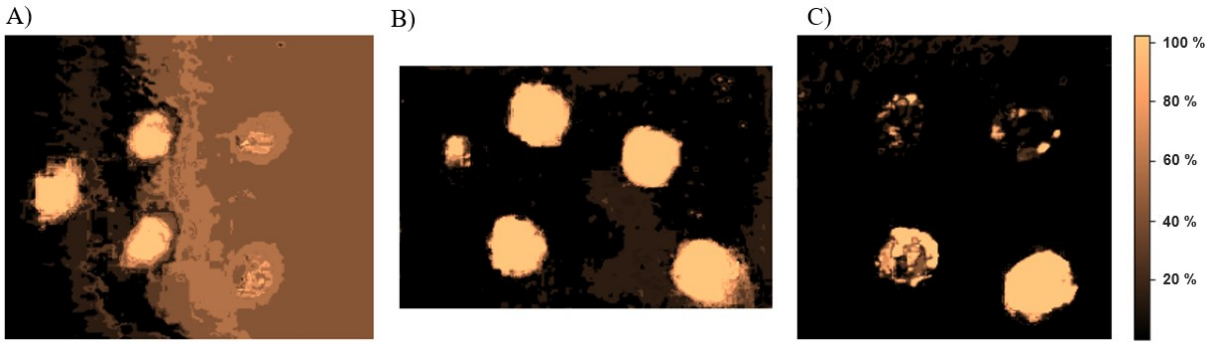

Figure 78 Probability of impact predicted by a k-NN model on the same test

To avoid the formation of artifacts from this issue, one possible solution is to work with normalized RGB values ((R,G,B) → (R,G,B)/S ; S = R+G+B). This method allows to reduce the impact of lighting on the outcome. Indeed, in RGB code R,G and B values range from 0 to 255 and the color white is (255,255,255). Thus, if an area is more lit, it is probable that the R,G and B values would also increase. By normalizing the data on S (which also increases with luminosity since S = R+G+B) it is possible to compare more meaningfully the brighter and darker parts of an image. However, one must be careful when using normalized values due to information loss. Indeed, a normalized image can be represented by only two values (for example R' and G') since the third component is now a linear combination of the other two (B' = 1 – R' – G', it carries no additional information). Thus, it could lead to poorer impact detection. Fortunately, in this case, while the technique did remove lighting artifacts, it also allowed for a better impact detection, as can be seen with the final results on Figure 79.

It is a good time to mention the virtues of simple impact detection and its dependance on the thermodynamics of SCO compounds. With a good understanding of the thermodynamics of the compound used, simple impact detection can already give an indication of the pressure applied. Indeed, the Clapeyron equation (Eq. (13)) already mentioned previously allows to calculate the threshold pressure at which a compound will start to switch spin states. For Fe(pyrazine)[Fe(CN)$_5$NO], the experimental values from literature (ΔV = 5.53 10^{-5} $m^3.mol^{-1}$, ΔS = 48.06 $J.(mol.K)^{-1}$, $T_{HS \rightarrow LS} = 245\ K$) permit us to

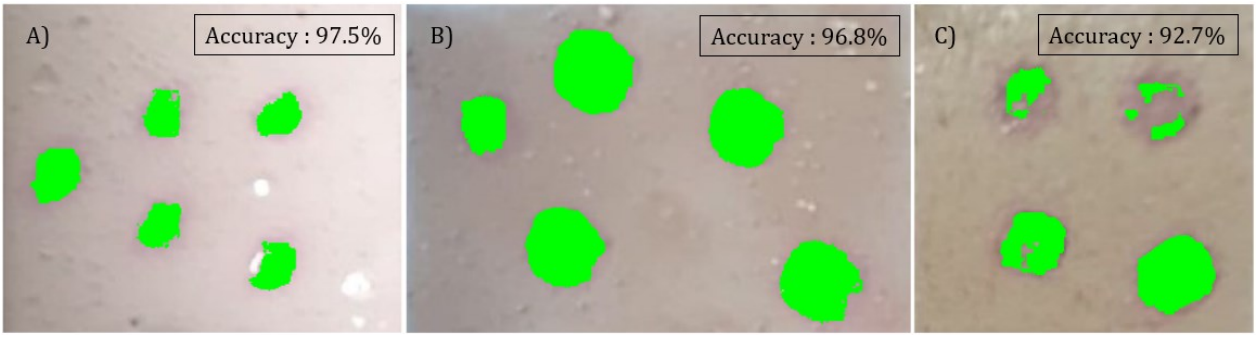

Figure 79 Impact detection for $[Fe(NH_2trz)_3]Br_2 \cdot nH_2O$-PU coatings based on an ensemble of three machine learning algorithms trained on normalized RGB data for A) SCO + TiO_2 B) SCO C) SCO-Fluorescence coatings. Green pixels represent the pixels considered as impacted by the model

conclude that a threshold pressure of 46 MPa is required. [88] For $[Fe(NH_2trz)_3]Br_2 \cdot nH_2O$, the experimental values are not available, but the current tests showed that it will switch at pressure as low as ~4 MPa, as will be shown in the next section. Finally, the previously mentioned $[Fe(hyetrz)_3]I_2 \cdot H_2O$ has been shown to switch at a minimum of 30 MPa. [17] These values which are already very different demonstrate that for dedicated applications, a careful selection of the SCO compound used, based not only on the stability properties (hysteresis position and width), but also on the piezo response could be sufficient for certain applications. Indeed, if the SCO compound is chosen (and/or the polymer matrix is selected to modulate the SCO compound response to pressure) so that the threshold pressure corresponds to the impact pressure for which an intervention is need (repairs or check-up…), then there is no need for an impact pressure determination model such as the ones presented in the following section.

13.2 Impact pressure determination

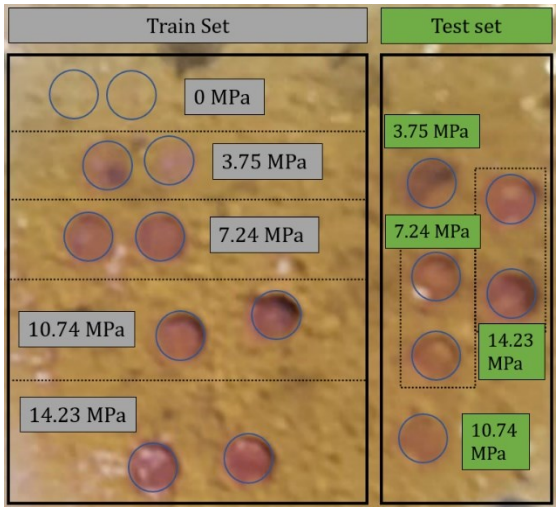

Figure 80 SCO-PU coating with a train set (left) of experimental points and a test set (right) for pressure models

To observe whether the coatings' response differs based on pressure, and whether it is possible to predict the pressure, several models were trained on the coating of Figure 80. The pressures applied on this coating were produced using an iron rod, upon which a platform was fixed. Then, weights were placed on that platform to produce the pressure. Knowing the mass added (and thus the force F), as well as the cross-section (S) of the iron rod, one can calculate the pressure applied since $P = \frac{F}{S}$.

On a sidenote, already one interesting thing to note is that as is displayed on Figure 80, $[Fe(NH_2trz)_3]Br_2 \cdot nH_2O$ already starts switching from HS to LS at 3.75 MPa. While more extensive measurements should be made to accurately determine the threshold pressure of $[Fe(NH_2trz)_3]Br_2 \cdot nH_2O$, this measurement already allows a minimum estimate of $\Delta V_{HS \to LS}$. Indeed, using Clapeyron equation (Eq. (13)) with $P_{thr} = 3.75\ MPa$ and the experimental value of $\Delta S_{HS \to LS} = 71.47\ [J.(K.mol)^{-1}]$, one can compute the minimal value of $\Delta V_{HS \to LS}$ to be $-2.7423 * 10^{-4}\ \frac{m^3}{mol}$ or $-455.53\ Å^3$ per Fe^{II} centres. While this is probably not the real value of the volume change, it provides a lower limit to $\Delta V_{HS \to LS}$ since it can be reasonably assumed that the real value cannot be lower than the one calculated here.

The data gathered and used to train the models is obtained from reading the color of the coating in RGB codification (R = red, G = green and B = blue, from 0 (min) to 255 (max)). Already, by only looking at the training data displayed on Figure 81, we see that there is a clear response of the color (here the green intensity) based on the pressure applied and that that response is somewhat linear for a range of pressure. Then, a slight curve is observed for higher pressure, but it should be said that this curve could be due to numerous things (coating inhomogeneity, difference in lighting etc.) other than the base response of the SCO compound. Nevertheless, this test shows that the piezochromic response of the $[Fe(NH_2trz)_3]Br_2$-PU coatings is of good enough quality to justify an attempt at developing pressure prediction models based on it.

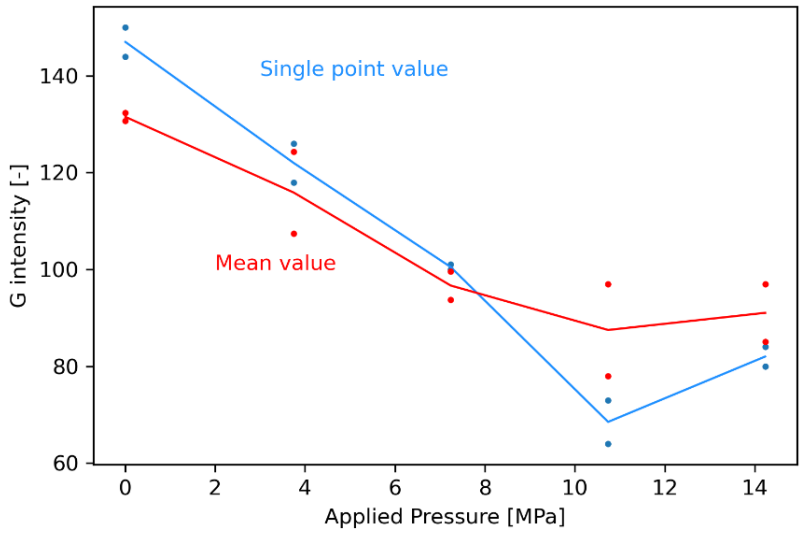

Figure 81 G intensity response to applied pressure as obtained from Figure 80, selected RGB values in blue and mean RGB values over the whole impact in red

To train as well as to test the generated models, the points where the RGB value will be evaluated must be defined. One possibility is to select one pixel value arbitrarily within the circles drawn by the pressure applicator. Another possibility is to automate the process. In that case, the mean RGB values over the whole impacts were obtained using, the **imageio** library of the **Python** programming language. [115] Finally, one can map the predicted pressure over the entire image and display it, which can be useful for trying to display the asymmetry of an impact.

Different statistical models can be used. In this case, four models have been tested: standard linear, k-NN, Random Forest and polynomial regression models. A brief explanation of these models can be found in Annexes 17.17 and 17.18. These models were once again generated using the **caret** package of the R programming language. [116]

For the first methodology (arbitrary choice of the points), while the linear and polynomial (second degree) models returned poor results both the k-NN and Random Forest fared much better (Table 5). Although the k-NN model returned good performances, especially for the root mean square error (RMSE), it was decided to exclude it for the rest of this work. The reason for this is the setup of the experiment as well as the few numbers of datapoints. Indeed, a further study of the k-NN models revealed that k = 1 would return the best performances. However, keeping in mind that the pressure applied for the test set were identical to the pressures used to train the algorithm, and that a k = 1 k-NN algorithm returns a prediction equal to the closest point of the train set, one could understand how a k = 1 algorithm could return almost no error. In fact, in real situations where the pressure would not match the train set pressures, this algorithm would surely fair much worse. In this way, the setup of the experiment is flawed and skews the results towards k-NN models. While nothing is said of the real performance of k-NN models for a piezo-predictive purpose, they cannot be evaluated in this work.

Table 5 Performance indicators for the different statistical models tested

Models	*Lack of Precision (mean % error)*	*RMSE [MPa]*
Linear model	33.7	2.94
Polynomial model (degree 2) + interactions	32.7	4.439
k-NN regression model (k=3)	25.61	1.842
Random Forest model (Rf)	23.68	2.02

Further adjustments can be made to improve upon the statistical models. Three variables were used for the models, namely R, G and B. However, it is possible that some of these are confounding variables, which does not bring much to the predictive power of the

model. To test this, each combination of variables was tested (RG, RB, BG, R, G, B and (R+G+B)/3 = mean). The best results from these tests are displayed on Table 6.

Table 6 Performance indicators comparing effect of the different variables

Models	*Lack of Precision (mean % error)*	*RMSE [MPa]*
Rf model (G and B)	22.33	1.878
Rf model (G and R)	17.78	1.802
Rf model (G)	14.20	1.821
Polynomial regression degree 4 (G)	17.71	1.602

The conclusion is that the best model only makes use of the G variable. This is not surprising, considering that purple (combination of red and blue) is the opposite color to green. With that in mind it is easy to understand how the green parameter is better able to discriminate the affected regions, and it would probably be confirmed by mapping the absorptivity of the LS state. On the other hand, it is unclear whether a random forest or a polynomial model would be optimal. The more adopted performance indicator, the root mean square error (RMSE) is smaller for the polynomial model. However, the mean % error is better for the Random Forest model. Further study with a bigger dataset would be required to make an educated decision. Nevertheless, the two models are displayed on Figure 82 along with the test and train datapoints in magenta and blue respectively.

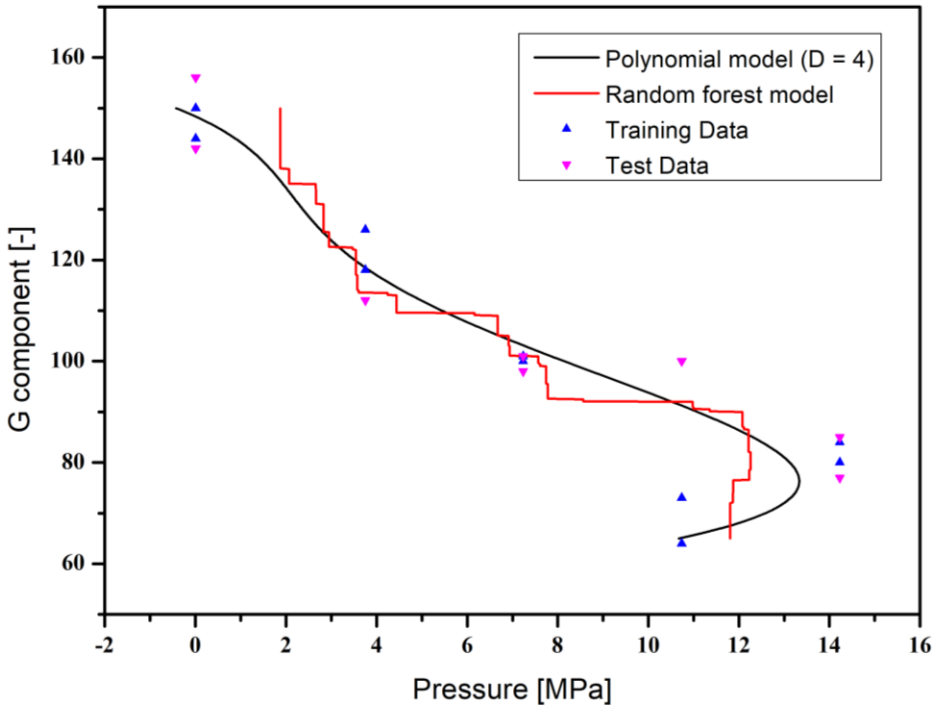

Figure 82 G intensity response to applied pressure, lines represent the prediction models generated, triangles the (training and test) image data

Although these results are already a strong indicator of the feasibility of impact and pressure determination, it is important to mention the experimental limitations that might weaken the conclusions drawn for the models tested. Indeed, the coating used to derive this model was far from homogeneous. The data collection is also somewhat subjected to experimental variations: the rudimentary setup used for pressure application can lead to uncertainties regarding the actual pressure applied, and the choice of point at which RGB color is sampled inside the affected region can be arbitrary (even though Figure 81 shows the same trend for the points selected and the average over the whole impact). Finally, the experimental limitations made it difficult to take datapoints at pressures different than the pressures used in the training set. To better evaluate the quality of the models, a more diverse set of datapoint for testing should be taken. Further tests using dedicated pressure devices could be viable solutions for the improvement of predictive models. Also, measurements other than RGB could be done to attempt a higher precision, for example absorptivity measurements.

To conclude, these results represent the first step in the elaboration of a pressure prediction model based on the response from a SCO-PU hybrid coating. While the quality of the prediction is still to be improved, the results obtained from this simple experimental setup show great promise and clearly demonstrate the realistic prospect of pressure quantification through optical measurements of our hybrid material.

13.3 Pressure Map – combination of impact detection and pressure determination

Using the best statistical model from the previous section, it is possible to predict the pressure applied over the entire coating, and representing it as a pressure map, as depicted on Figure 84. This method has not only the advantage of providing an overview of the entire studied coating, but also of displaying the areas that might be more affected by impacts. Indeed, measuring the impact pressure from a single point or from the average over the entire impact provides a single pressure value, which might not necessarily be the highest pressure felt during the impact. Using a pressure map to provide an estimate for each pixel of the image could better indicate whether the substrate under the coating is at risk of being damaged.

However, this map is very noisy, with a lot of areas which were not impacted that still record (low) pressures. It can then be difficult to distinguish the real impacted areas from the noise. One possibility to remedy this is simply to combine the two models which were trained in this work. This way, impact detection would first be done on the image, then the pressure would be predicted by the second model only for the regions which were considered as impacted. This is done on Figure 83, which as you can see provides a much clearer picture

while keeping what is interesting about the pressure map (mapping different pressures for a single impact).

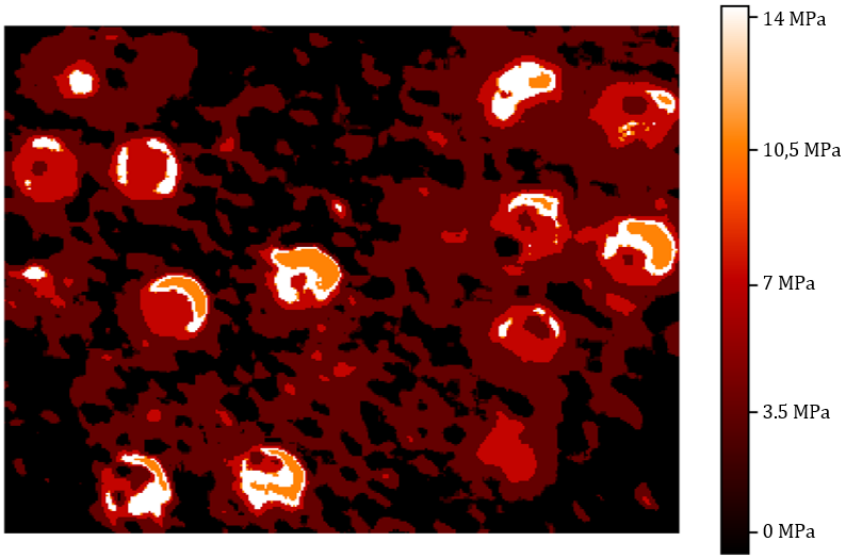

Figure 84 Pressure map over the entire coating

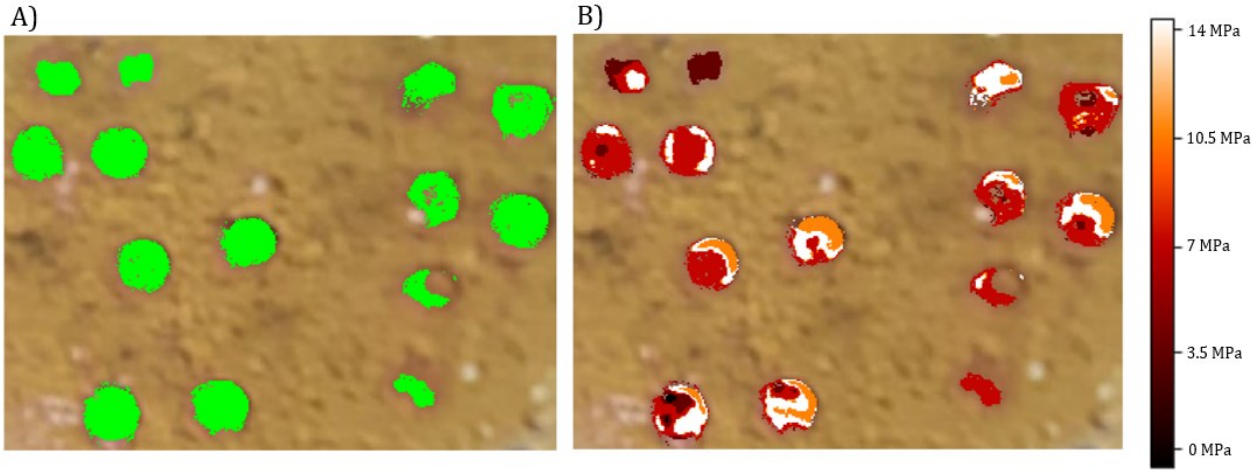

Figure 83 Combination of pressure and impact detection models to provide pressure estimates only on impacted areas

14. Coupling SCO crossover with fluorescence

For the detection and quantification of impact pressures, one must be able to measure a signal that can be translated into the pressure information. For piezochromic compounds, this is usually done via RGB or Visible light absorbance measurements; the intensity of which can be correlated to the pressure intensity, as has just been demonstrated in the machine learning models presented.

Another interesting possibility would be to couple fluorescence and spin-crossover. A fluorescent response could then be modulated by the spin transition, and the spin state switch could then be quantified by measuring the difference in fluorescence from HS and LS state, rather than the difference in colour. [79,117]

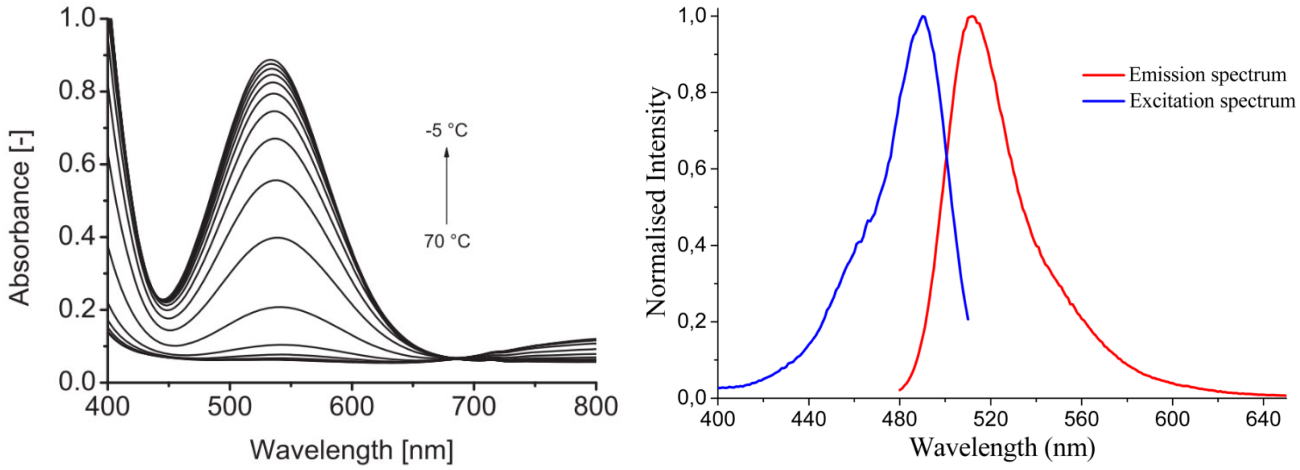

Figure 85 Absorbance of an example SCO compound for the LS state (-5°C) and the HS state (70 °C) (left) excitation and emission spectra of a fluorophore (right). Here, the emission peak corresponds to the maximum absorption peak of the LS state. [74,112]

As explained previously in Section 6.2, the LS state of most Fe^{II} compounds absorbs around 550 nm, while the HS state only (barely) absorbs in the NIR region. Thus, the basic principle used to combine fluorescence with SCO behaviour is to associate the SCO compound with a fluorophore that has an emission or excitation maximum wavelength that corresponds to the maximum absorption peak of the LS state of the spin-crossover complex (see Figure 85).[47] This results in the quenching of the fluorescence in the LS state, while the fluorescent compound is still active in the HS state. Based on the general absorption peak of SCO compounds, several fluorophores have been selected for trials, and their results are displayed in the following section.

There are three ways a fluorophore can be incorporated into the hybrid material. These fluorophores can be incorporated into the SCO compounds directly into the SCO synthesis, where it could modify their properties (ex : reduction of cooperativity, coordination…)[45,47], but it could lead to tighter interactions between the fluorophore and the SCO, so better quenching in the LS state. The other possibility is to introduce the fluorophore in the SCO + polymer hybrid. This method is easier, as one does not need to be mindful of any modification of the SCO properties, but the quenching in the LS could be expected to be poorer if either the SCO compound or the fluorophore is poorly dispersed in the polymer. On the other hand, several well-known mechanisms could overall decrease the fluorescence intensity independently of the spin state (excimer formation or static quenching, SCO-fluorophore interactions…). [118] Finally, the fluorophore can be incorporated into the polymer synthesis, so that it rests inside the polymer chain. This is the most desirable incorporation method,

since it less susceptible to perturb the spin transition, while also stabilizing the fluorescence. In the next steps of this work, it will be prioritized whenever possible.

Multiple fluorescent molecules that have excitation or emission peaks corresponding to the maximum absorption wavelength of the LS state have been tested and have also been included in the polymer chain whenever possible. While more fluorophores have been tested (Coumarin, Coumarin 6, Eosin Y …), only the best results are presented here, which were obtained with Fluorescein, Rhodamin and related compounds.

14.1 Fluorescein

Perhaps the most famous and used fluorescent compound that was tested is fluorescein. Once again, the emission wavelength of this compound matches the absorption wavelength of our SCO compound ($[Fe(NH_2trz)_3]Br_2$) in the LS state (~530-550 nm) (Figure 86). We can then expect a lower fluorescence behaviour of a SCO-PU-Fluorophore hybrid in the LS state.

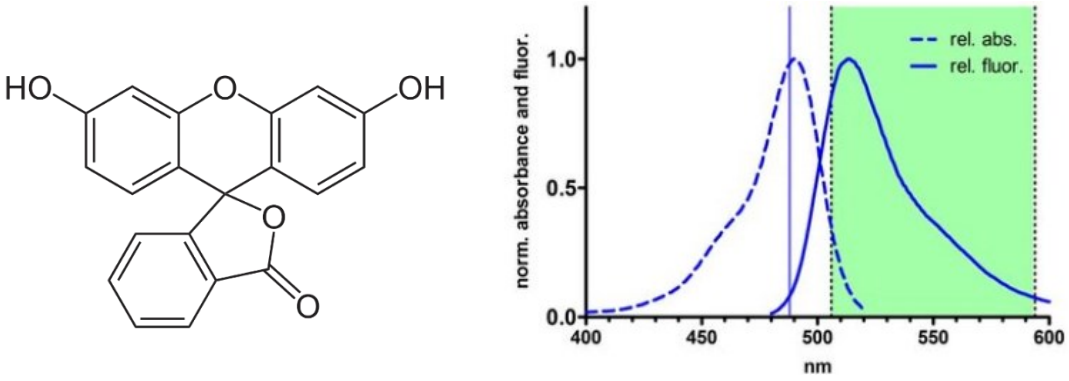

Figure 86 Left) Fluorescein chemical structure Right) Fluorescein absorption (dotted line) and emission (full line) spectra [119]

A first attempt, which is shown on Figure 87, is indeed promising, with a clear response and modulation of the fluorescent behaviour with the application of a pressure. This attempt was made by introducing the fluorescent molecule directly into the SCO-PU hybrid, and not during the SCO compound or polymer syntheses. However, the fluorescence intensity of the coating showed instability over time, with a gradual quenching, leading to an almost null intensity after a few hours.

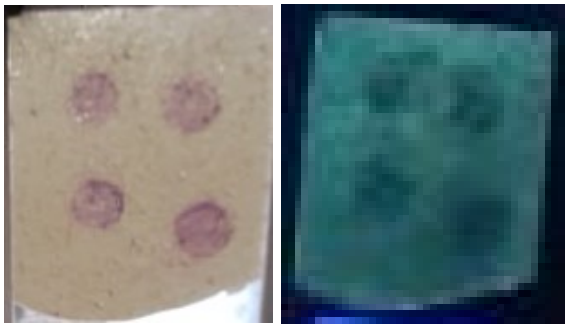

Figure 87 $[Fe(NH_2trz)_3]Br_2{\cdot}nH_2O$-PU hybrid (left) piezochromic behaviour (right) "piezofluorescent" behaviour

The first hypothesis for this fluorescence quenching was that, as a "free molecule", fluorescein is able to form excimers, which are dimers of the excited form of the fluorophore. These dimers have a lifetime of the order of the second, which means that the excited electrons have plenty of time to relax in non-radiative ways. On the other hand, a regular fluorophore has an excited lifetime of $\sim 10^{-8}$ seconds. Thus, these excimers have a much lower probability of fluorescing. [120]

To prevent their formation, the incorporation of fluorescein (and derivative) into the polyurethane polymer chains, which creates steric constraints between fluorophore molecules, was explored as a possible solution. For this purpose, both fluorescein and fluorescein isothiocyanate were selected for their two reactive hydroxyl groups (which allows their incorporation into the polymeric chain), as well as their proven performance in polyurethane coatings. [120] With this in mind, the fluorescent polymers where synthesized by adding the fluorescent molecules at the beginning of the polymer synthesis (in the HDI, PGE and DMPA mixture).

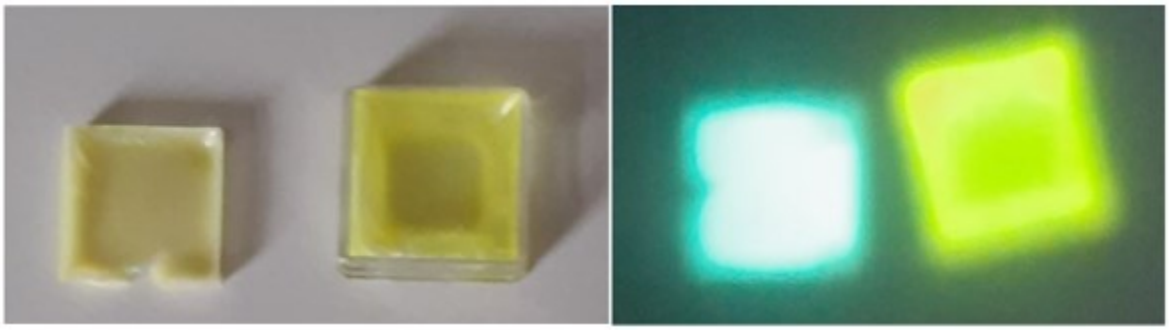

Figure 88 Fluorescent polymer obtained with Fluorescein isothiocyanate (left) and Fluorescein (right)

The resulting standalone PU coatings displayed better fluorescent properties (see Figure 88). This method was indeed successful at preventing excimer formation (self-quenching). [120] However, the fluorescence intensity once again diminished after adding the SCO compound, which meant that a specific interaction with the compound was taking place, and further solutions needed to be found. Still, the overall mechanical, fluorescent and stability properties of these polymers were superior to the "free fluorophore" coatings mentioned previously, so this technique was preferred for the remainder of this work. Although the properties of these coatings provide us with a clue that the fluorescent molecules were indeed included in the polymer chains, no conclusive evidence was able to be obtained. The main reason for this is the very small quantities of fluorophores added to produce these polymers (in the realm of ‰ in weight), below the sensitivity of traditional investigation techniques. As expected, FTIR spectra were identical to bare PU spectra as already presented in Section 9.3. These spectra can be found in Annex 17.19 and 17.20.

At this stage, the obvious conclusion is that $[Fe(NH_2trz)_3]Br_2$ interacts with the incorporated fluorescein, by quenching its fluorescence. Since research already identified halides as fluorescence quenchers [121], the focus was initially on the Br^- ion present in the SCO compound. To test whether it was the culprit, a $FeBr_2$ salt was added into the fluorescent polymer, and an immediate stark nullification of the fluorescence was observed. However, the same test conducted with $ZnBr_2$ showed no such quenching. The problematic conclusion of this result was that Br^- is not responsible for the fluorescence quenching, but rather Fe^{II}. This meant that a part of the Fe^{II} ions inside the coordination polymer must be released when in contact with the polymer. Indeed, this is an issue since it would have been easy to replace the counter-ion used by one that does not interact with fluorescein (for example, p-toluenesulfonate). [47] However, it is impossible to replace Fe^{II} since it is essential for the SCO mechanism. Nevertheless, a solution may have been found. Indeed, the main hypothesis as to how it is possible that the Fe^{II} inside the SCO compound is capable of reaching and interacting with the fluorophore is as follows: as the polymer dispersion in liquid form is composed of 60-70 w% of water, it is entirely possible that part of the SCO compound is completely solubilized, freeing Fe^{II} ions into the polymer. Indeed, the fluorescein content of the polymer is minimal compared to the amount of SCO compound added. About 50 mg (0.1 mmol) of SCO compound is added to 0.5g of liquid polymer (10% SCO in weight), a quantity that contains about 0.08 mg (0.2 µmol) of fluorescein. In these conditions, even if only 2‰ of the iron compound were dissolved it would be enough to quench all the fluorescein at a 1:1 ratio. Another clue pointing to this is the fact that in some coatings (e.g. Figure 52), the residual HS fraction increased, indicating that there might have been a shortening of the SCO chains. A graphic illustration of this hypothesis is displayed on Figure 89a.

With this hypothesis in mind, two precautions were made to try to prevent the liberation of Fe^{II} ions, with varying results. Firstly, only polymers with a minimal water content (60%) were used, for obvious reasons.

The second precaution involves $ZnBr_2$ and recalls a technique mentioned previously: the mechanochemical synthesis of the SCO compound. The idea is to prevent the liberation of Fe^{II} ions by capping off the ends of the Fe-NH_2Triazole chains with Zn-NH_2Triazole (illustrated on Figure 89b). Indeed, it has already been demonstrated by researchers (Section 7.1) and in this work (see Annex 17.7) that Zn^{II} can produce the same coordination complex structure (such as presented in Annex 17.7) as Fe^{II}, due to the two ions' similar radius, [32] and that Zn^{II} doesn't have the same quenching properties as Fe^{II}. Zn^{II} centres can then form a sort of copolymer with Fe^{II} centres. Here, the copolymer obtained would not be random (like in the literature, resulting in a loss of cooperativity) but rather a block copolymer composed of 3 blocks : a central Fe^{II} block surrounded by two Zn^{II} blocks (no loss of cooperativity). With such a compound realised, one could expect that the partial dissolution of the compound in

the fluorescent polymer would only free Zn^{II} ions, thereby protecting the fluorescence. To obtain such a compound, $[Fe(NH_2trz)_3]Br_2$ was added into a mortar in addition to a $ZnBr_2$ salt and NH_2trz in solid form. The three solids were ground using a pestle with a drop of water to provide the proper diffusion medium, just as described in Section 10.2.2.

While it is difficult to confirm that this hypothesis is correct, it is possible to confirm that the Zn^{II} centres are not included inside the polymer chain and forming a random copolymer such as the ones described in literature, via magnetic measurements. Indeed, as Figure 90 displays, there is no shortening of the hysteresis width, or reduction of the transition temperatures which would be expected behaviours if iron centres were diluted by zinc centres.

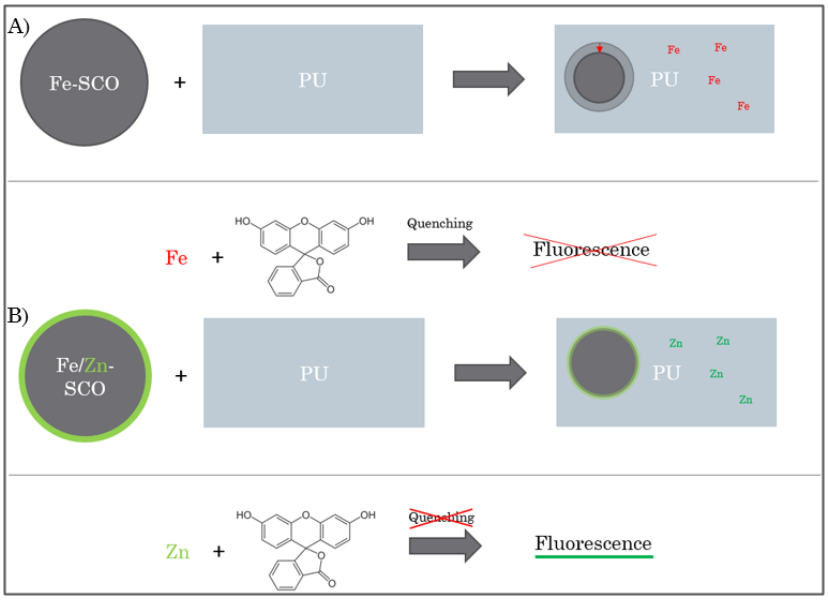

Figure 89 Illustration of the proposed fluorescence quenching mechanism as well as the proposed quenching prevention mechanism

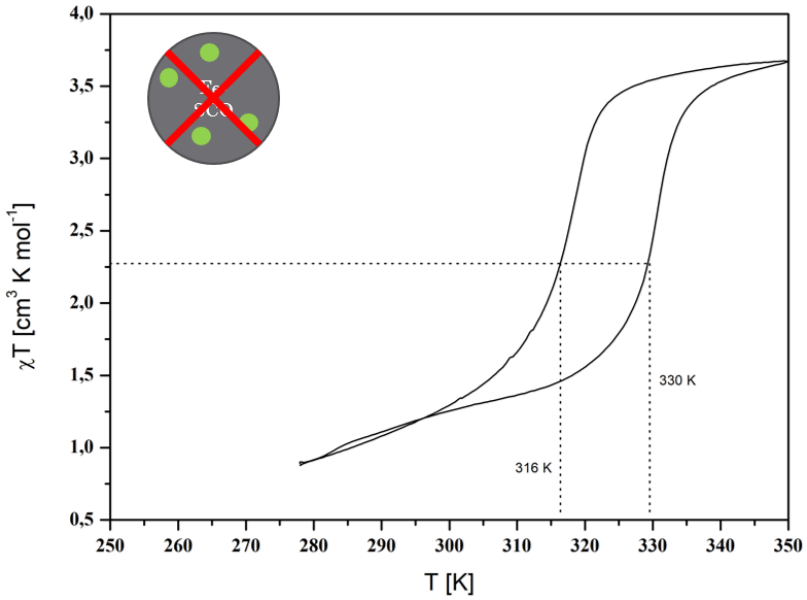

Figure 90 SQUID magnetic data of Zn-mechanochemicalsynthesis-modified $[Fe(NH_2trz)_3]Br_2.nH_2O$ recorded at a rate of 2K/min in a 1000 Oe field

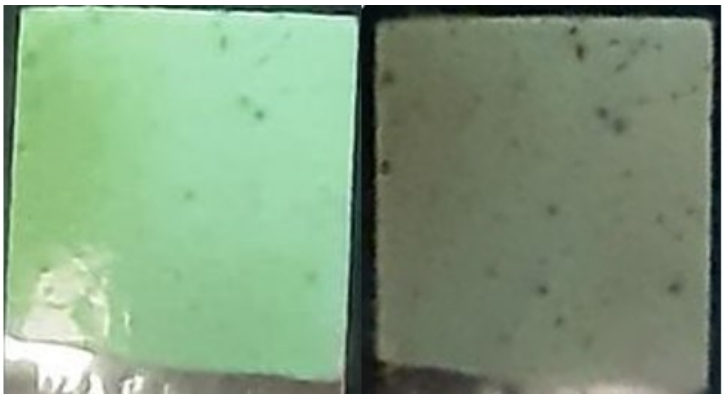

Figure 91 Fluorescent coating in the HS state (left) and in the LS state (right)

This final precaution did indeed allow to avoid the fluorescence quenching by iron ions, as the coating of Figure 91 shows. The LS state of $[Fe(NH_2trz)_3]Br_2$ does indeed quench the fluorescence, while the HS state does not, and these properties are retained even as the coating completely dries. Image analysis using the ImageJ software [122] measures a decrease in fluorescence from HS → LS of 26%.

This however does not confirm the hypothesis posed for the third precaution. Indeed, the solution behaved as expected but it is possible that another mechanism is in effect. One possibility that was brought up is that the NH_2trz molecules introduced are able to capture the released Fe^{II} ions. However, tests with only NH_2trz returned a quenching of the fluorescence. This means that the combination of NH_2trz and $ZnBr_2$ has an active role in maintaining the fluorescence properties.

While these coatings present excellent fluorescence properties, other properties expected of coatings are lacklustre (tackiness, rigidity, chemical stability…). One way to try to remedy these shortcomings is simply to produce a blend of already established polyurethanes (such as **D13**, presented in this work) and the fluorescent polyurethane. A trial was done with a 50/50% mix of both polyurethane as well as $[Fe(NH_2trz)_3]Br_2$ as SCO compound and is presented on Figure 92. This trial did indeed provide better coatings. However, this only acts as a temporary fix and further testing and tuning for a standalone fluorescent polymer would be necessary to obtain the best performances.

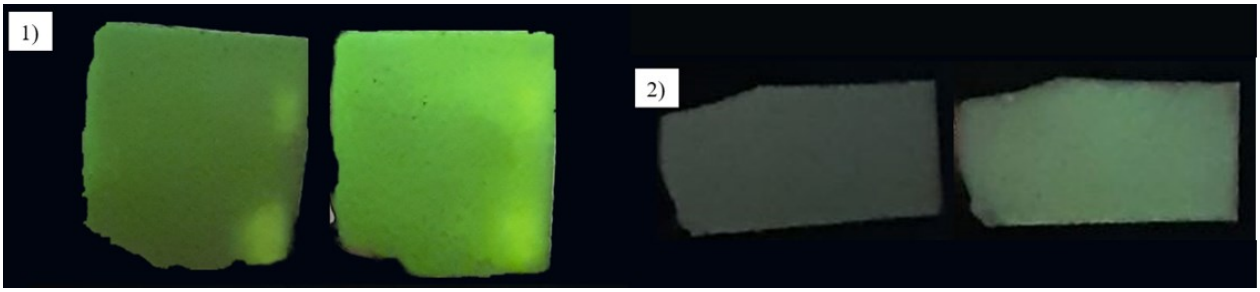

Figure 92 Standard PU/Fluorescent PU 50/50% mixture with 10% (wt) of $[Fe(NH_2trz)_3]Br_2$ in the LS state (left) and HS state (right). 1) corresponds to the Fluorescein polymer, 2) to the Fluorescein isothiocyanate polymer

For reference, these polyurethane polymers contained 0.2 ‰w of fluorescein and were combined with 10-15% (weight) of SCO compound. With these ratios, basic fluorescence intensity measurements using the ImageJ software [122] reveal a quenching of 35% of the mean fluorescence over the entire coating for the fluorescein polymer, and 42% for the fluorescein isothiocyanate polymer. It is observed that this quenching is obviously very dependent on the quantity of SCO introduced. An interesting follow-up would be to search for the optimal ratio to obtain the maximum contrast between HS and LS phases.

14.2 Rhodamin 6G and Rhodamin B

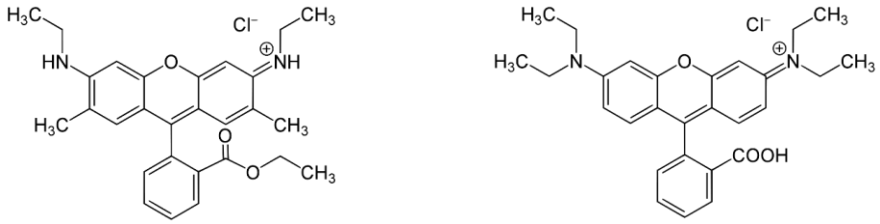

Figure 93 Rhodamin 6G (left) and Rhodamin B (right)

Rhodamin 6G and Rhodamin B are other fluorescent molecules that were considered for trials. Once again, the possibility of incorporating the molecule in the coordination sphere of the SCO compound was discarded in order to conserve the desired spin transition. Several trials were conducted by simply incorporating the fluorophores in the SCO-PU hybrid. Similarly to fluorescein, these trials indeed demonstrated the quenching capabilities of $[Fe(NH_2trz)_3]Br_2 \cdot nH_2O$ in the LS state, as shown on Figure 94.

However, once again a great diminishing of the fluorescence intensity (even in the HS state) is observed after complete drying of the coating. Without too much repetition, the same precautions as for fluorescein were taken. Namely, these are the incorporation of the fluorophore into the polymer chain, the minimization of the water content and the use of Zn-aminotriazole to avoid the liberation of Fe^{II} ions.

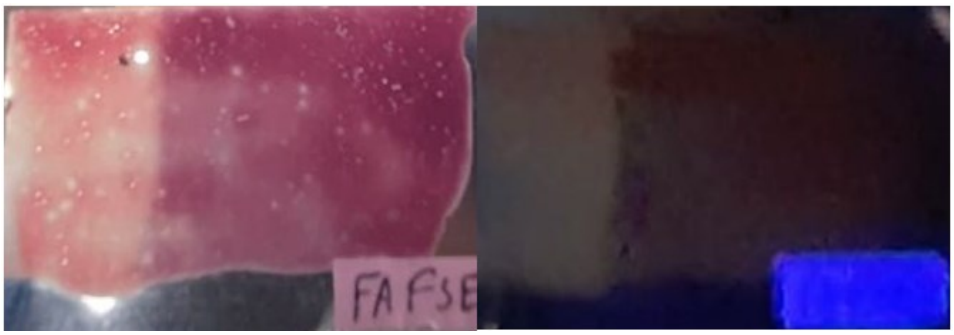

Figure 94 Preliminary trial of Rhodamin B-$[Fe(NH_2trz)_3]Br_2.nH_2O$ fluorescent coating Left) under visible light Right) under UV light. HS state and the bistability are demonstrated by the clearer part of the coating

To be able to incorporate the fluorophore, Rhodamin 6G needs to be modified to increase its content in reactive groups, as depicted on Figure 95. [123] FTIR measurements (Figure 95) were able to confirm the synthesis of the Rhodamin derivative and the complete conversion of Rhodamin 6G via the disappearance of the 1716 cm^{-1} peak and the appearance of a 1678 cm^{-1} peak attesting to the shift of this -C=O peak corresponding to the change from an ester function to an amide function in the final product. [123]

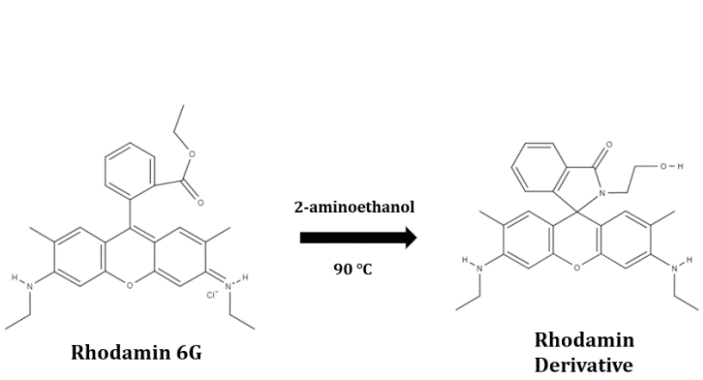

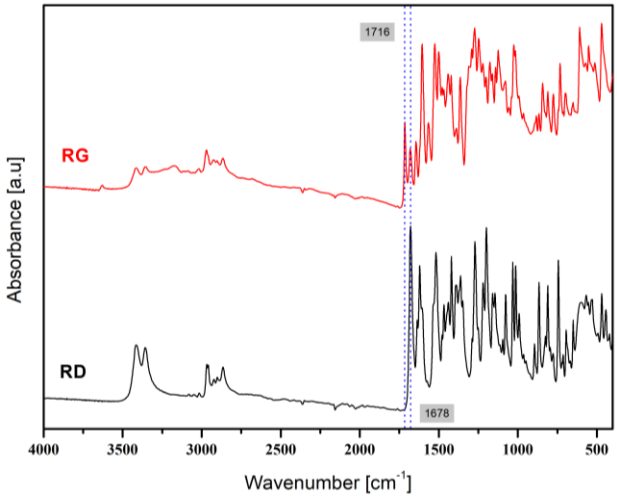

Figure 95 Left) Reaction scheme to obtain the Rhodamin derivative Right) FTIR spectra of rhodamin 6G (RG) and rodamine derivate (RD)

The advantage of this molecule is that it presents three reactive groups (2 -NH, 1 -OH) which allows it to be used a cross-linking agent, thus improving the mechanical resistance of the polymer in addition to providing fluorescent properties. It is easily incorporable into the chain by adding it into the synthesis at the same time as the diisocyanate. Here, the quantities of fluorescent agent added are significantly greater than for the fluorescein case (2-4 %w), but FTIR measurements were still not sensitive enough to confirm the inclusion the polymer chain. However, Figure 97 demonstrates the fluorescent properties of the coating.

The incorporation of $[Fe(NH_2trz)_3]Br_2 \cdot nH_2O$ produced even better result than fluorescein polymers, as is visible on Figure 96.

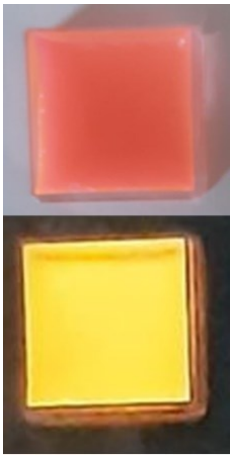

Figure 97 Rhodamine derivative fluorescent polymer Up) under visible light Down) under UV light

Figure 96 Rodamine derivative-SCO fluorescent coating in the LS state (left) and HS state (right). Inset images are the same coating under normal light

In comparison to the fluorescein coating, analysis of the fluorescence intensity shows a 70% drop when in the LS state. This is indeed one example of a fact that has become clear throughout my trials which is that in general Rhodamin B, Rhodamin 6G and the Rhodamin derivative seemed to be less sensitive to $[Fe(NH_2trz)_3]Br_2 \cdot nH_2O$ than the fluorescein species.

In the end, SCO-fluorescence coupling was successful, but not without its challenges. It was possible to couple the fluorescence of several compounds from the well-known fluorescein and rhodamine families, with $[Fe(NH_2trz)_3]Br_2$, provided that fluorescent molecules were protected from the quenching effect of Fe^{II} ions. Thus, this work highlights the feasibility and opportunity that this technology represents, while also providing what I believe to be its main hurdle to overcome, Fe^{II} quenching. While this work attempts to solve the issue by shielding the Fe^{II} centres, other possibilities could include using non water-soluble SCO compounds or non water-based polymer matrices.

15. Conclusion

To conclude, I believe this work has demonstrated the potential of hysteretic SCO compounds for piezochromic technologies. They have demonstrated their superiority over other traditional classes of piezochromic compounds thanks to the combination of their **bistability** (memory effect) and **conditional reversibility**. Their potential has also been demonstrated inside a polymer matrix, with clear thermo- and piezochromic properties and compatibility with coating applications.

The WBPU matrix proved compatible with the tested SCO compounds. Although not without interaction between the two components, as for aminotriazole compounds, results from this work indicate that the composition of the polymer can drastically affect the SCO properties, and that aminated compounds should be avoided in the polyurethane formulation to avoid a yellowing of the hybrid material. A perturbation of the semi-crystalline structure of the polymer has also been observed when in contact with an aminotriazole SCO compound, which seemed to lead to worsened mechanical properties. Nevertheless, the use of covalent crosslinking via UV-cured polymer techniques has been proposed and tested as possible solution to improve these properties, with good results.

The synthesis method for the SCO compound also seemed to influence the behaviour inside the matrix. Especially for $[Fe(NH_2trz)_3]Br_2$, for which the solvent mix used affected not only the SCO properties, but also the dispersivity inside the polymer matrix. However, this is only true for the classical synthesis of the compound. Two other synthesis methods, which have their own advantages, have also been presented: the mechanochemical synthesis, which is nearly solvent free and the newly described *In situ* synthesis directly inside the polymer,

which allows to avoid costly steps such as drying or the use of solvent in the SCO compound synthesis.

The other tested compound, Fe(pyrazine)[$Fe(CN)_5NO$], presented much better compatibility with the WBPU matrix, as evidenced by the retaining of the microscopic ordering of the polymer-SCO hybrid and its good mechanical properties. Its SCO-chromic properties, which differ from the triazole SCO compound family, also opens the way for bi-SCO coatings capable of both precise pressure and temperature determination.

About pressure determination, this work has demonstrated the relationship between pressure and the color change intensity in the $[Fe(NH_2trz)_3]Br_2$-PU coatings as well as several machine learning models that provide a good prediction of the pressure applied based on the impact color. But this was not the only models generated. Indeed, an attempt at impact detection automation returned good result, after normalizing the data fed to the model. While impact detection could already be sufficient for some applications (with good knowledge of the SCO compound used), it can also be associated to pressure determination, to be able to map the heterogeneity of impacts without having to sort out the noise returned by the pressure prediction models.

Finally, providing another property for evaluation than color for the hybrid coatings was attempted. For this, coupling of SCO properties with fluorescein- and rhodamin-derived polymers returned the best results, although avoiding the quenching effect of Fe^{II} was necessary. It was indeed possible to couple the two phenomena, even though some challenges remain, such as the improvement of the mechanical properties of the coatings as well as their stability over time.

16. References

(1) *AMA Sensorik und Messtechnik -Quarterreports 2021*. https://www.ama-sensorik.de/en/association/sector-information/quarterreports-2021/ (accessed 2022-05-26).

(2) Liu, C.; Harley, J. B.; Bergés, M.; Greve, D. W.; Oppenheim, I. J. Robust Ultrasonic Damage Detection under Complex Environmental Conditions Using Singular Value Decomposition. *Ultrasonics* **2015**, *58*, 75–86. https://doi.org/10.1016/j.ultras.2014.12.005.

(3) Wang, Y.; Ke, H.; Shi, J.; Gao, B.; Tian, G. Impact Damage Detection and Characterization Using Eddy Current Pulsed Thermography. In *2016 IEEE Far East NDT New Technology & Application Forum (FENDT)*; IEEE: Nan Chang, China, 2016; pp 223–226. https://doi.org/10.1109/FENDT.2016.7992029.

(4) Seeboth, A.; Loetzsch, D.; Ruhmann, R. Piezochromic Polymer Materials Displaying Pressure Changes in Bar-Ranges. *Am. J. Mater. Sci.* **2012**, *1* (2), 139–142. https://doi.org/10.5923/j.materials.20110102.23.

(5) Harms, N. C.; Kim, H.-S.; Clune, A. J.; Smith, K. A.; O'Neal, K. R.; Haglund, A. V.; Mandrus, D. G.; Liu, Z.; Haule, K.; Vanderbilt, D.; Musfeldt, J. L. Piezochromism in the Magnetic Chalcogenide $MnPS_3$. *Npj Quantum Mater.* **2020**, *5* (1), 56. https://doi.org/10.1038/s41535-020-00259-5.

(6) Blanco-Gutierrez, V.; Cornu, L.; Demourgues, A.; Gaudon, M. $CoMoO_4/CuMo_{0.9}W_{0.1}O_4$ Mixture as an Efficient Piezochromic Sensor to Detect Temperature/Pressure Shock Parameters. *ACS Appl. Mater. Interfaces* **2015**, *7* (13), 7112–7117. https://doi.org/10.1021/am508652h.

(7) Morelle, Q.; Senani, S.; Nicole, L.; Gaudon, M.; Rozes, L.; Le Bourhis, E. Hybrid Piezochromic Coatings for Impact Detection on Composite Substrates for Aeronautic. *Mater. Lett.* **2019**, *253*, 140–143. https://doi.org/10.1016/j.matlet.2019.06.045.

(8) *Smart Intelligent Aircraft Structures (SARISTU)*; Wölcken, P. C., Papadopoulos, M., Eds.; Springer International Publishing: Cham, 2016. https://doi.org/10.1007/978-3-319-22413-8.

(9) Feltham, H. L. C.; Barltrop, A. S.; Brooker, S. Spin Crossover in Iron(II) Complexes of 3,4,5-Tri-Substituted-1,2,4-Triazole (Rdpt), 3,5-Di-Substituted-1,2,4-Triazolate (Dpt −), and Related Ligands. *Coord. Chem. Rev.* **2017**, *344*, 26–53. https://doi.org/10.1016/j.ccr.2016.10.006.

(10) Ridier, K.; Molnár, G.; Salmon, L.; Nicolazzi, W.; Bousseksou, A. Hysteresis, Nucleation and Growth Phenomena in Spin-Crossover Solids. *Solid State Sci.* **2017**, *74*, A1–A22. https://doi.org/10.1016/j.solidstatesciences.2017.10.014.

(11) Kahn, O. Spin-Crossover Molecular Materials. *Curr. Opin. Solid State Mater. Sci.* **1996**, *1* (4), 547–554. https://doi.org/10.1016/S1359-0286(96)80070-2.

(12) Garcia, Y.; Niel, V.; Muñoz, M. C.; Real, J. A. Spin Crossover in 1D, 2D and 3D Polymeric Fe(II) Networks. In *Spin Crossover in Transition Metal Compounds I*; Gütlich, P., Goodwin, H. A., Eds.; Topics in Current Chemistry; Springer Berlin Heidelberg: Berlin, Heidelberg, 2004; Vol. 233, pp 229–257. https://doi.org/10.1007/b95408.

(13) Senthil Kumar, K.; Ruben, M. Emerging Trends in Spin Crossover (SCO) Based Functional Materials and Devices. *Coord. Chem. Rev.* **2017**, *346*, 176–205. https://doi.org/10.1016/j.ccr.2017.03.024.

(14) Bousseksou, A.; Molnár, G.; Tuchagues, J.-P.; Menéndez, N.; Codjovi, É.; Varret, F. Triggering the Spin-Crossover of Fe(Phen)2(NCS)2 by a Pressure Pulse. Pressure and Magnetic Field Induce 'Mirror Effects.' *Comptes Rendus Chim.* **2003**, *6* (3), 329–335. https://doi.org/10.1016/S1631-0748(03)00042-0.

(15) Boukheddaden, K.; Ritti, M. H.; Bouchez, G.; Sy, M.; Dîrtu, M. M.; Parlier, M.; Linares, J.; Garcia, Y. Quantitative Contact Pressure Sensor Based on Spin Crossover Mechanism for Civil

Security Applications. *J. Phys. Chem. C* **2018**, *122* (14), 7597–7604. https://doi.org/10.1021/acs.jpcc.8b00778.
(16) Linares, J.; Codjovi, E.; Garcia, Y. Pressure and Temperature Spin Crossover Sensors with Optical Detection. *Sensors* **2012**, *12* (4), 4479–4492. https://doi.org/10.3390/s120404479.
(17) Jureschi, C.; Linares, J.; Rotaru, A.; Ritti, M.; Parlier, M.; Dîrtu, M.; Wolff, M.; Garcia, Y. Pressure Sensor via Optical Detection Based on a 1D Spin Transition Coordination Polymer. *Sensors* **2015**, *15* (2), 2388–2398. https://doi.org/10.3390/s150202388.
(18) Jureschi, C.-M.; Linares, J.; Boulmaali, A.; Dahoo, P.; Rotaru, A.; Garcia, Y. Pressure and Temperature Sensors Using Two Spin Crossover Materials. *Sensors* **2016**, *16* (2), 187. https://doi.org/10.3390/s16020187.
(19) Gütlich, P.; Garcia, Y. Spin Crossover Systems. In *Reference Module in Chemistry, Molecular Sciences and Chemical Engineering*; Elsevier, 2015; p B9780124095472114000. https://doi.org/10.1016/B978-0-12-409547-2.11373-3.
(20) Griffith, J. S.; Orgel, L. E. Ligand-Field Theory. *Q. Rev. Chem. Soc.* **1957**, *11* (4), 381. https://doi.org/10.1039/qr9571100381.
(21) Attwood, M.; Turner, S. S. Back to Back 2,6-Bis(Pyrazol-1-Yl)Pyridine and 2,2′:6′,2″-Terpyridine Ligands: Untapped Potential for Spin Crossover Research and Beyond. *Coord. Chem. Rev.* **2017**, *353*, 247–277. https://doi.org/10.1016/j.ccr.2017.09.025.
(22) Gütlich, P.; Hauser, A.; Spiering, H. Thermal and Optical Switching of Iron(II) Complexes. *Angew. Chem. Int. Ed. Engl.* **1994**, *33* (20), 2024–2054. https://doi.org/10.1002/anie.199420241.
(23) von Ranke, P. J. A Microscopic Refrigeration Process Triggered through Spin-Crossover Mechanism. *Appl. Phys. Lett.* **2017**, *110* (18), 181909. https://doi.org/10.1063/1.4982792.
(24) Etrillard, C. Synthèse de nanoparticules à transition de spin et étude des propriétés, application en électronique moléculaire. 210.
(25) Craig, G. A.; Roubeau, O.; Aromí, G. Spin State Switching in 2,6-Bis(Pyrazol-3-Yl)Pyridine (3-Bpp) Based Fe(II) Complexes. *Coord. Chem. Rev.* **2014**, *269*, 13–31. https://doi.org/10.1016/j.ccr.2014.02.002.
(26) Capes, L. Adressage optique des matériaux à transition de spin du Fe(II). 231.
(27) Nicolazzi, W.; Bousseksou, A. Thermodynamical Aspects of the Spin Crossover Phenomenon. *Comptes Rendus Chim.* **2018**, *21* (12), 1060–1074. https://doi.org/10.1016/j.crci.2018.10.003.
(28) Borshch, S. A. Theoretical Approaches for Spin-Crossover Phenomenon in Transition-Metal Complexes. In *Comprehensive Inorganic Chemistry II*; Elsevier, 2013; pp 469–480. https://doi.org/10.1016/B978-0-08-097774-4.00921-9.
(29) Forestier, T. Synthèse de Nanoparticules à Transition de Spin En Milieu Confiné. 185.
(30) Miller, E. J. S.; Drillon, M. Magnetism: Molecules to Materials IV. **2002**, 491.
(31) Slichter, C. P.; Drickamer, H. G. Pressure-Induced Electronic Changes in Compounds of Iron. *J. Chem. Phys.* **1972**, *56* (5), 2142–2160. https://doi.org/10.1063/1.1677511.
(32) Gütlich, P.; Gaspar, A. B.; Garcia, Y. Spin State Switching in Iron Coordination Compounds. *Beilstein J. Org. Chem.* **2013**, *9*, 342–391. https://doi.org/10.3762/bjoc.9.39.
(33) Sorai, M.; Ensling, J.; Hasselbach, K. M.; Gütlich, P. Mössbauer Effect Study on Low-Spin 1A1 ⇌ High Spin 5T2 Transition in [Fe(2-Pic)3]Cl2. *Chem. Phys.* **1977**, *20* (2), 197–208. https://doi.org/10.1016/0301-0104(77)85023-4.
(34) Gutlich, P.; Ksenofontov, V.; Gaspar, A. Pressure Effect Studies on Spin Crossover Systems. *Coord. Chem. Rev.* **2005**, *249* (17–18), 1811–1829. https://doi.org/10.1016/j.ccr.2005.01.022.
(35) Dîrtu, M. M.; Neuhausen, C.; Naik, A. D.; Rotaru, A.; Spinu, L.; Garcia, Y. Insights into the Origin of Cooperative Effects in the Spin Transition of $[Fe(NH_2Trz)_3](NO_3)_2$: The Role of

Supramolecular Interactions Evidenced in the Crystal Structure of $[Cu(NH_2Trz)_3](NO_3)_2 \cdot H_2O$. *Inorg. Chem.* **2010**, *49* (12), 5723–5736. https://doi.org/10.1021/ic100667f.
(36) Ksenofontov, V.; Gaspar, A. B.; Niel, V.; Reiman, S.; Real, J. A.; Gütlich, P. On the Nature of the Plateau in Two-Step Dinuclear Spin-Crossover Complexes. *Chem. - Eur. J.* **2004**, *10* (5), 1291–1298. https://doi.org/10.1002/chem.200305275.
(37) Garcia, Y.; Adarsh, N. N.; Naik, A. D. Crystal Engineering of Fe^{II} Spin Crossover Coordination Polymers Derived from Triazole or Tetrazole Ligands. *CHIMIA* **2013**, *67* (6), 411. https://doi.org/10.2533/chimia.2013.411.
(38) Miller, R. G.; Narayanaswamy, S.; Tallon, J. L.; Brooker, S. Spin Crossover with Thermal Hysteresis in Cobalt(II) Complexes and the Importance of Scan Rate. *New J. Chem.* **2014**, *38* (5), 1932. https://doi.org/10.1039/c3nj01451g.
(39) Drath, O.; Boskovic, C. Switchable Cobalt Coordination Polymers: Spin Crossover and Valence Tautomerism. *Coord. Chem. Rev.* **2018**, *375*, 256–266. https://doi.org/10.1016/j.ccr.2017.11.025.
(40) Hayami, S.; Komatsu, Y.; Shimizu, T.; Kamihata, H.; Lee, Y. H. Spin-Crossover in Cobalt(II) Compounds Containing Terpyridine and Its Derivatives. *Coord. Chem. Rev.* **2011**, *255* (17–18), 1981–1990. https://doi.org/10.1016/j.ccr.2011.05.016.
(41) Zhao, S.-Z.; Qin, C.-Y.; Wang, S.; Yamashita, M.; Li, Y.-H.; Huang, W. Structure–Function Correlations in Mononuclear Manganese(III) Spin Crossover Systems with a Big Conjugated Hexadentate Schiff-Base Ligand. *Dalton Trans.* **2020**, *49* (14), 4293–4305. https://doi.org/10.1039/C9DT04882K.
(42) Harding, D. J.; Harding, P.; Phonsri, W. Spin Crossover in Iron(III) Complexes. *Coord. Chem. Rev.* **2016**, *313*, 38–61. https://doi.org/10.1016/j.ccr.2016.01.006.
(43) Olguín, J. Unusual Metal Centres/Coordination Spheres in Spin Crossover Compounds. *Coord. Chem. Rev.* **2020**, *407*, 213148. https://doi.org/10.1016/j.ccr.2019.213148.
(44) Garcia, Y.; Gütlich, P. Thermal Spin Crossover in Mn(II), Mn(III), Cr(II) and Co(III) Coordination Compounds. In *Spin Crossover in Transition Metal Compounds II*; Topics in Current Chemistry; Springer Berlin Heidelberg: Berlin, Heidelberg, 2004; Vol. 234, pp 49–62. https://doi.org/10.1007/b95412.
(45) Garcia, Y.; Robert, F.; Naik, A. D.; Zhou, G.; Tinant, B.; Robeyns, K.; Michotte, S.; Piraux, L. Spin Transition Charted in a Fluorophore-Tagged Thermochromic Dinuclear Iron(II) Complex. *J. Am. Chem. Soc.* **2011**, *133* (40), 15850–15853. https://doi.org/10.1021/ja205974q.
(46) Wang, C.-F.; Li, R.-F.; Chen, X.-Y.; Wei, R.-J.; Zheng, L.-S.; Tao, J. Synergetic Spin Crossover and Fluorescence in One-Dimensional Hybrid Complexes. *Angew. Chem. Int. Ed.* **2015**, *54* (5), 1574–1577. https://doi.org/10.1002/anie.201410454.
(47) Salmon, L.; Molnár, G.; Zitouni, D.; Quintero, C.; Bergaud, C.; Micheau, J.-C.; Bousseksou, A. A Novel Approach for Fluorescent Thermometry and Thermal Imaging Purposes Using Spin Crossover Nanoparticles. *J. Mater. Chem.* **2010**, *20* (26), 5499. https://doi.org/10.1039/c0jm00631a.
(48) Liu, N.; Zhao, Y.; Kang, M.; Wang, J.; Wang, X.; Feng, Y.; Yin, N.; Li, Q. The Effects of the Molecular Weight and Structure of Polycarbonatediols on the Properties of Waterborne Polyurethanes. *Prog. Org. Coat.* **2015**, *82*, 46–56. https://doi.org/10.1016/j.porgcoat.2015.01.015.
(49) Bierwagen, G.; Brown, R.; Battocchi, D.; Hayes, S. Active Metal-Based Corrosion Protective Coating Systems for Aircraft Requiring No-Chromate Pretreatment. *Prog. Org. Coat.* **2010**, *67* (2), 195–208. https://doi.org/10.1016/j.porgcoat.2009.10.009.
(50) Lapresta-Fernández, A.; Cuéllar, M. P.; Herrera, J. M.; Salinas-Castillo, A.; Pegalajar, M. del C.; Titos-Padilla, S.; Colacio, E.; Capitán-Vallvey, L. F. Particle Tuning and Modulation of the Magnetic/Colour Synergy in Fe(II) Spin Crossover-Polymer Nanocomposites in a

Thermochromic Sensor Array. *J Mater Chem C* **2014**, *2* (35), 7292–7303. https://doi.org/10.1039/C4TC00969J.
(51) Dick, F. D. Solvent Neurotoxicity. *Occup. Environ. Med.* **2006**, *63* (3), 221–226. https://doi.org/10.1136/oem.2005.022400.
(52) Madbouly, S. A. Waterborne Polyurethane Dispersions and Thin Films: Biodegradation and Antimicrobial Behaviors. *Molecules* **2021**, *26* (4), 961. https://doi.org/10.3390/molecules26040961.
(53) Nikalin, D. M.; Serdtselyubova, A. S.; Merkulova, Yu. I.; Kozlova, A. A. Waterborne Polyurethane Paints and Varnishes for Metal Surfaces: Patent Review. *Russ. J. Gen. Chem.* **2021**, *91* (3), 540–545. https://doi.org/10.1134/S1070363221030233.
(54) Santamaria-Echart, A.; Fernandes, I.; Barreiro, F.; Corcuera, M. A.; Eceiza, A. Advances in Waterborne Polyurethane and Polyurethane-Urea Dispersions and Their Eco-Friendly Derivatives: A Review. *Polymers* **2021**, *13* (3), 409. https://doi.org/10.3390/polym13030409.
(55) Honarkar, H. Waterborne Polyurethanes: A Review. *J. Dispers. Sci. Technol.* **2018**, *39* (4), 507–516. https://doi.org/10.1080/01932691.2017.1327818.
(56) Ikeda, M. Public Health Problems of Organic Solvents. *Toxicol. Lett.* **1992**, *64–65*, 191–201. https://doi.org/10.1016/0378-4274(92)90189-Q.
(57) *Aliphatic Diisocyanates (ADI)*. American Chemistry Council. https://www.americanchemistry.com/industry-groups/aliphatic-diisocyanates-adi/overview (accessed 2022-05-23).
(58) Huybrechts, J. T.; Tanghe, L. M. 2.1 VOC Solvent Borne 2K Clear Coats Based on Star Oligoethers. *Prog. Org. Coat.* **2007**, *58* (2–3), 217–226. https://doi.org/10.1016/j.porgcoat.2006.09.029.
(59) *Options for Polyurethane Chemistry*. https://www.adhesivesmag.com/articles/91695-options-for-polyurethane-chemistry (accessed 2022-05-23).
(60) Gopalakrishnan, S.; Fernando, T. L. Effect of Aliphatic Diisocyanates on the Properties of Cardanol-Based Polyurethanes. **2010**, 10.
(61) Dall Agnol, L.; Dias, F. T. G.; Ornaghi, H. L.; Sangermano, M.; Bianchi, O. UV-Curable Waterborne Polyurethane Coatings: A State-of-the-Art and Recent Advances Review. *Prog. Org. Coat.* **2021**, *154*, 106156. https://doi.org/10.1016/j.porgcoat.2021.106156.
(62) Kuok, A. M. E.; Sipaut, C. S.; Sundang, M. Synthesis and Characterisation of New Water-Based Polyurethane Dispersion via Solvent-Free Prepolymer Mixing Process. *J. Phys.* 11.
(63) Burchardt, B. Advances in Polyurethane Structural Adhesives. In *Advances in Structural Adhesive Bonding*; Elsevier, 2010; pp 35–65. https://doi.org/10.1533/9781845698058.1.35.
(64) Fang, Z. H.; Shang, J. J.; Huang, Y. X.; Wang, J.; Li, D. Q.; Liu, Z. Y. Preparation and Characterization of the Heat-Resistant UV Curable Waterborne Polyurethane Coating Modified by Bisphenol A. *Express Polym. Lett.* **2010**, *4* (11), 704–711. https://doi.org/10.3144/expresspolymlett.2010.85.
(65) Zhou, X. Q.; Cao, Y. M.; Tian, J. L. Synthesis and Properties of Waterborne UV Polyurethane. *Adv. Mater. Res.* **2011**, *311–313*, 1087–1092. https://doi.org/10.4028/www.scientific.net/AMR.311-313.1087.
(66) Rao, L.; Zhou, H.; Li, T.; Li, C.; Duan, Y. Y. Polyethylene Glycol-Containing Polyurethane Hydrogel Coatings for Improving the Biocompatibility of Neural Electrodes. *Acta Biomater.* **2012**, *8* (6), 2233–2242. https://doi.org/10.1016/j.actbio.2012.03.001.
(67) Mumtaz, F.; Zuber, M.; Zia, K. M.; Jamil, T.; Hussain, R. Synthesis and Properties of Aqueous Polyurethane Dispersions: Influence of Molecular Weight of Polyethylene Glycol. *Korean J. Chem. Eng.* **2013**, *30* (12), 2259–2263. https://doi.org/10.1007/s11814-013-0166-9.
(68) Pérez Das Dores, A.; Llorente, O.; Martin, L.; González, A.; Irusta, L. Polydimethylsiloxane Containing Waterborne Hydrophobic Polyurethane Coatings with Good Adhesion to Metals:

Synthesis and Characterization. *Prog. Org. Coat.* **2022**, *162*, 106564. https://doi.org/10.1016/j.porgcoat.2021.106564.
(69) Kapatel, P. Flame Retardant Waterborne Polyurethanes: Synthesis, Characterization, and Evaluation of Different Properties. *Biointerface Res. Appl. Chem.* **2021**, *12* (3), 3198–3214. https://doi.org/10.33263/BRIAC123.31983214.
(70) Madbouly, S. A.; Otaigbe, J. U. Recent Advances in Synthesis, Characterization and Rheological Properties of Polyurethanes and POSS/Polyurethane Nanocomposites Dispersions and Films. *Prog. Polym. Sci.* **2009**, *34* (12), 1283–1332. https://doi.org/10.1016/j.progpolymsci.2009.08.002.
(71) Ebrahimi, M. V.; Barikani, M.; Mohammad, S.; Mohaghegh, S. Synthesis and Properties of Ionic Polyurethane Dispersions: Influence of Polyol Molecular Weight. *Iran. Polym. J.* **2006**, *15* (4), 9.
(72) Wang, X.; Cui, Y.; Wang, Y.; Ban, T.; Zhang, Y.; Zhang, J.; Zhu, X. Preparation and Characteristics of Crosslinked Fluorinated Acrylate Modified Waterborne Polyurethane for Metal Protection Coating. *Prog. Org. Coat.* **2021**, *158*, 106371. https://doi.org/10.1016/j.porgcoat.2021.106371.
(73) Yu, C.; Xie, Q.; Bao, Y.; Shan, G.; Pan, P. Crystalline and Spherulitic Morphology of Polymers Crystallized in Confined Systems. *Crystals* **2017**, *7* (5), 147. https://doi.org/10.3390/cryst7050147.
(74) Waletzko, R. S.; Korley, L. T. J.; Pate, B. D.; Thomas, E. L.; Hammond, P. T. Role of Increased Crystallinity in Deformation-Induced Structure of Segmented Thermoplastic Polyurethane Elastomers with PEO and PEO−PPO−PEO Soft Segments and HDI Hard Segments. *Macromolecules* **2009**, *42* (6), 2041–2053. https://doi.org/10.1021/ma8022052.
(75) Sundararajan, S.; Kumar, A.; Chakraborty, B. C.; Samui, A. B.; Kulkarni, P. S. Poly(Ethylene Glycol) (PEG)-Modified Epoxy Phase-Change Polymer with Dual Properties of Thermal Storage and Vibration Damping. *Sustain. Energy Fuels* **2018**, *2* (3), 688–697. https://doi.org/10.1039/C7SE00552K.
(76) Mondal, S.; Martin, D. Hydrolytic Degradation of Segmented Polyurethane Copolymers for Biomedical Applications. *Polym. Degrad. Stab.* **2012**, *97* (8), 1553–1561. https://doi.org/10.1016/j.polymdegradstab.2012.04.008.
(77) Yang, Z.; Wu, G. Effects of Soft Segment Characteristics on the Properties of Biodegradable Amphiphilic Waterborne Polyurethane Prepared by a Green Process. *J. Mater. Sci.* **2020**, *55* (7), 3139–3156. https://doi.org/10.1007/s10853-019-04237-6.
(78) Cheng, B.-X.; Gao, W.-C.; Ren, X.-M.; Ouyang, X.-Y.; Zhao, Y.; Zhao, H.; Wu, W.; Huang, C.-X.; Liu, Y.; Liu, X.-Y.; Li, H.-N.; Li, R. K. Y. A Review of Microphase Separation of Polyurethane: Characterization and Applications. *Polym. Test.* **2022**, *107*, 107489. https://doi.org/10.1016/j.polymertesting.2022.107489.
(79) Bräunlich, I.; Sánchez-Ferrer, A.; Bauer, M.; Schepper, R.; Knüsel, P.; Dshemuchadse, J.; Mezzenga, R.; Caseri, W. Polynuclear Iron(II)–Aminotriazole Spincrossover Complexes (Polymers) In Solution. *Inorg. Chem.* **2014**, *53* (7), 3546–3557. https://doi.org/10.1021/ic403035u.
(80) Vallée, A.; Train, C.; Roux, C. Synthesis and Properties of a Thermochromic Spin Crossover Fe ^{II} Complex: An Undergraduate Coordination Chemistry Laboratory Experiment. *J. Chem. Educ.* **2013**, *90* (8), 1071–1076. https://doi.org/10.1021/ed4000487.
(81) Lavrenova, L. G.; Shakirova, O. G.; Ikorskii, V. N.; Varnek, V. A.; Sheludyakova, L. A.; Larionov, S. V. 1A1 5T2 Spin Transition in New Thermochromic Iron(II) Complexes with 1,2,4-Triazole and 4-Amino-1,2,4-Triazole. **2003**, *29* (1), 6.
(82) Mader, D. Relation structure – propriétés de commutation dans les matériaux à transition de spin : effet de nanostructuration et de dilution du cation métallique. 327.

(83) Forestier, T.; Kaiba, A.; Pechev, S.; Denux, D.; Guionneau, P.; Etrillard, C.; Daro, N.; Freysz, E.; Létard, J.-F. Nanoparticles of $[Fe(NH_2\text{-}Trz)_3]Br_2{\cdot}3H_2O$ (NH_2-Trz=2-Amino-1,2,4-Triazole) Prepared by the Reverse Micelle Technique: Influence of Particle and Coherent Domain Sizes on Spin-Crossover Properties. *Chem. - Eur. J.* **2009**, *15* (25), 6122–6130. https://doi.org/10.1002/chem.200900297.

(84) Fouché, O.; Degert, J.; Jonusauskas, G.; Daro, N.; Létard, J.-F.; Freysz, E. Mechanism for Optical Switching of the Spin Crossover $[Fe(NH_2\text{-}Trz)_3](Br)_2{\cdot}3H_2O$ Compound at Room Temperature. *Phys. Chem. Chem. Phys.* **2010**, *12* (12), 3044. https://doi.org/10.1039/b921984f.

(85) Gural'skiy, I. A.; Shylin, S. I.; Ksenofontov, V.; Tremel, W. Spin-State-Dependent Redox-Catalytic Activity of a Switchable Iron(II) Complex. *Eur. J. Inorg. Chem.* **2017**, *2017* (24), 3125–3131. https://doi.org/10.1002/ejic.201700454.

(86) Kahn, O.; Codjovi, E. Iron (II) - 1,2,4,- Triazole Spin Transition Molecular Materials. *Philos. Trans. R. Soc. Lond. Ser. Math. Phys. Eng. Sci.* **1996**, *354* (1706), 359–379. https://doi.org/10.1098/rsta.1996.0012.

(87) Abdelmola, F.; Carlsson, L. A. State of Water in Void-Free and Void-Containing Epoxy Specimens. *J. Reinf. Plast. Compos.* **2019**, *38* (12), 556–566. https://doi.org/10.1177/0731684419833469.

(88) Plasencia, Y.; Avila, Y.; Rodríguez-Hernández, J.; Ávila, M.; Reguera, E. Thermally Induced Spin Transition in $Fe(Pyrazine)[Fe(CN)_5NO]$. *J. Phys. Chem. Solids* **2021**, *150*, 109843. https://doi.org/10.1016/j.jpcs.2020.109843.

(89) Suleimanov, I.; Costa, J. S.; Molnár, G.; Salmon, L.; Fritsky, I.; Bousseksou, A. Effect of Ligand Substitution in $[Fe(H\text{-}Trz)_2(Trz)]BF_4$ Spin Crossover Nanoparticles. *Fr.-Ukr. J. Chem.* **2015**, *3* (1), 66–72. https://doi.org/10.17721/fujcV3I1P66-72.

(90) *Molecule-Based Magnetic Materials: Theory, Techniques, and Applications*; Turnbull, M. M., Sugimoto, T., Thompson, L. K., Eds.; ACS Symposium Series; American Chemical Society: Washington, DC, 1996; Vol. 644. https://doi.org/10.1021/bk-1996-0644.

(91) van Koningsbruggen, P. J.; Garcia, Y.; Codjovi, E.; Lapouyade, R.; Kahn, O.; Fournès, L.; Rabardel, L. Non-Classical FeII Spin-Crossover Behaviour in Polymeric Iron(II) Compounds of Formula $[Fe(NH_2trz)_3]X_2xH_2O$ (NH_2trz=4-Amino-1,2,4-Triazole; X=derivatives of Naphthalene Sulfonate). *J. Mater. Chem.* **1997**, *7* (10), 2069–2075. https://doi.org/10.1039/a702690k.

(92) Askew, J. H.; Shepherd, H. J. Mechanochemical Synthesis of Cooperative Spin Crossover Materials. *Chem. Commun.* **2018**, *54* (2), 180–183. https://doi.org/10.1039/C7CC06651A.

(93) Askew, J. H.; Shepherd, H. J. Post-Synthetic Anion Exchange in Iron(II) 1,2,4-Triazole Based Spin Crossover Materials *via* Mechanochemistry. *Dalton Trans.* **2020**, *49* (9), 2966–2971. https://doi.org/10.1039/C9DT04700J.

(94) Wdowiak, T. J.; Klingelhöfer, G.; Wade, M. L.; Nuñez, J. I. Extracting Science from Mössbauer Spectroscopy on Mars: MÖSSBAUER SPECTROSCOPY ON MARS. *J. Geophys. Res. Planets* **2003**, *108* (E12). https://doi.org/10.1029/2003JE002071.

(95) Löf, D.; Hamieau, G.; Zalich, M.; Ducher, P.; Kynde, S.; Midtgaard, S. R.; Parasida, C. F.; Arleth, L.; Jensen, G. V. Dispersion State of TiO2 Pigment Particles Studied by Ultra-Small-Angle X-Ray Scattering Revealing Dependence on Dispersant but Limited Change during Drying of Paint Coating. *Prog. Org. Coat.* **2020**, *142*, 105590. https://doi.org/10.1016/j.porgcoat.2020.105590.

(96) Pham, D. N. K.; Roy, M.; Golen, J. A.; Manke, D. R. The First-Row Transition-Metal Series of Tris(Ethylenediamine) Diacetate Complexes $[M(En)_3](OAc)_2$(*M* Is Mn, Fe, Co, Ni, Cu, and Zn). *Acta Crystallogr. Sect. C Struct. Chem.* **2017**, *73* (6), 442–446. https://doi.org/10.1107/S2053229617006738.

(97) Shu, C.; Wen, Y.; Fang, H.; Huang, H.; Li, W. Synthesis of a Deep Eutectic Solvent Triethylamine/Salicylic Acid and Its Use for Extractive Denitrogenation. *IOP Conf. Ser. Earth Environ. Sci.* **2020**, *565* (1), 012099. https://doi.org/10.1088/1755-1315/565/1/012099.

(98) Keypour, H.; Silver, J.; Wilson, M. T.; Hamed, M. Y. Studies on the Reactions of Ferric Iron with Ascorbic Acid. A Study of Solution Chemistry Using Mössbauer Spectroscopy and Stopped-Flow Techniques. *Inorganica Chim. Acta* **1986**, *125* (2), 97–106. https://doi.org/10.1016/S0020-1693(00)82094-0.
(99) Sanchez-Adsuar, M. S.; Martín-Martínez, J. M. Influence of the Length of the Chain Extender on the Properties of Thermoplastic Polyurethanes. *J. Adhes. Sci. Technol.* **1997**, *11* (8), 1077–1087. https://doi.org/10.1163/156856197X00840.
(100) Yang, J.-E.; Lee, Y.-H.; Koo, Y.-S.; Jung, Y.-J.; Kim, H.-D. Preparation and Properties of Waterborne Poly(Urethane-Urea) Ionomers Effect of the Type of Neutralizing Agent. *Fibers Polym.* **2002**, *3* (3), 97–102. https://doi.org/10.1007/BF02892624.
(101) Liu, K.; Su, Z.; Miao, S.; Ma, G.; Zhang, S. UV-Curable Enzymatic Antibacterial Waterborne Polyurethane Coating. *Biochem. Eng. J.* **2016**, *113*, 107–113. https://doi.org/10.1016/j.bej.2016.06.004.
(102) Huh, J. H.; Kim, H. I.; Rahman, M. M.; Kim, H. D. Preparation and Properties of MDI/H $_{12}$ MDI-Based Water-Borne Poly(Urethane-Urea)s-Effects of MDI Content and Radiant Exposure. *J. Appl. Polym. Sci.* **2008**, *110* (6), 3655–3663. https://doi.org/10.1002/app.28876.
(103) *Standard Test Method for Film Hardness by Pencil Test*. https://www.astm.org/d3363-20.html (accessed 2022-05-17).
(104) Zhao, T.; Zhu, H.; Dong, M. The Nano-Confinement Effect on the SCO Behavior of $[Fe(NH_2trz)_3](NO_3)_2$ 1D Chains in MCM-41. **2020**, 8.
(105) Šalitroš, I.; Madhu, N. T.; Boča, R.; Pavlik, J.; Ruben, M. Room-Temperature Spin-Transition Iron Compounds. *Monatshefte Für Chem. - Chem. Mon.* **2009**, *140* (7), 695–733. https://doi.org/10.1007/s00706-009-0128-4.
(106) Muñoz, M. C.; Real, J. A. Thermo-, Piezo-, Photo- and Chemo-Switchable Spin Crossover Iron(II)-Metallocyanate Based Coordination Polymers. *Coord. Chem. Rev.* **2011**, *255* (17–18), 2068–2093. https://doi.org/10.1016/j.ccr.2011.02.004.
(107) Ni, Z.-P.; Liu, J.-L.; Hoque, Md. N.; Liu, W.; Li, J.-Y.; Chen, Y.-C.; Tong, M.-L. Recent Advances in Guest Effects on Spin-Crossover Behavior in Hofmann-Type Metal-Organic Frameworks. *Coord. Chem. Rev.* **2017**, *335*, 28–43. https://doi.org/10.1016/j.ccr.2016.12.002.
(108) Ohba, M.; Yoneda, K.; Agustí, G.; Muñoz, M. C.; Gaspar, A. B.; Real, J. A.; Yamasaki, M.; Ando, H.; Nakao, Y.; Sakaki, S.; Kitagawa, S. Bidirectional Chemo-Switching of Spin State in a Microporous Framework. *Angew. Chem. Int. Ed.* **2009**, *48* (26), 4767–4771. https://doi.org/10.1002/anie.200806039.
(109) Kosone, T.; Kitazawa, T. Guest-Dependent Spin Transition with Long Range Intermediate State for 2-Dimensional Hofmann-like Coordination Polymer. *Inorganica Chim. Acta* **2016**, *439*, 159–163. https://doi.org/10.1016/j.ica.2015.10.011.
(110) Kucheriv, O. I.; Fritsky, I. O.; Gural'skiy, I. A. Spin Crossover in Fe(II) Cyanometallic Frameworks. *Inorganica Chim. Acta* **2021**, *521*, 120303. https://doi.org/10.1016/j.ica.2021.120303.
(111) Yang, Y.; Shen, X.; Zhou, H.; Lang, L.; Zhu, G.; Ji, Z. Controlled Synthesis of [Fe(Pyridine)2Ni(CN)4] Nanostructures and Their Shape-Dependent Spin-Crossover Properties. *J. Magn. Magn. Mater.* **2020**, *496*, 165938. https://doi.org/10.1016/j.jmmm.2019.165938.
(112) Maskowicz, D.; Sawczak, M.; Ghosh, A. C.; Grochowska, K.; Jendrzejewski, R.; Rotaru, A.; Garcia, Y.; Śliwiński, G. Spin Crossover and Cooperativity in Nanocrystalline $[Fe(Pyrazine)Pt(CN)_4]$ Thin Films Deposited by Matrix-Assisted Laser Evaporation. *Appl. Surf. Sci.* **2021**, *541*, 148419. https://doi.org/10.1016/j.apsusc.2020.148419.
(113) Muñoz Lara, F. J.; Gaspar, A. B.; Aravena, D.; Ruiz, E.; Muñoz, M. C.; Ohba, M.; Ohtani, R.; Kitagawa, S.; Real, J. A. Enhanced Bistability by Guest Inclusion in Fe(II) Spin Crossover

Porous Coordination Polymers. *Chem. Commun.* **2012**, *48* (39), 4686. https://doi.org/10.1039/c2cc31048a.
(114) Zenere, K. A.; Duyker, S. G.; Trzop, E.; Collet, E.; Chan, B.; Doheny, P. W.; Kepert, C. J.; Neville, S. M. Increasing Spin Crossover Cooperativity in 2D Hofmann-Type Materials with Guest Molecule Removal. *Chem. Sci.* **2018**, *9* (25), 5623–5629. https://doi.org/10.1039/C8SC01040D.
(115) *Python Software Foundation. Python Language Reference, version 3.8. Available at*. Python.org. https://www.python.org/.
(116) *R Core Team (2020). R: A language and environment for statistical computing. R Foundation for Statistical Computing, Vienna, Austria. URL*. https://www.r-project.org/.
(117) Bennet, M. A. Multi-Parameter Quantitative Mapping of Microfluidic Devices, University of Edinburgh, Lyon, France, 2011.
(118) Radziuk, D.; Möhwald, H. Ultrasonically Treated Liquid Interfaces for Progress in Cleaning and Separation Processes. *Phys. Chem. Chem. Phys.* **2016**, *18* (1), 21–46. https://doi.org/10.1039/C5CP05142H.
(119) Jonak, C.; Skvara, H.; Kunstfeld, R.; Trautinger, F.; Schmid, J. A. Intradermal Indocyanine Green for In Vivo Fluorescence Laser Scanning Microscopy of Human Skin: A Pilot Study. *PLoS ONE* **2011**, *6* (8), e23972. https://doi.org/10.1371/journal.pone.0023972.
(120) He, X.; Hu, L.; Zou, L.; Zhong, J.; Luo, H.; Pu, Z. Enhanced Fluorescence Properties of Flexible Waterborne Polyurethane Films by Blocking Fluorescein Isothiocyanate (FITC). *Mater. Lett.* **2021**, *293*, 129668. https://doi.org/10.1016/j.matlet.2021.129668.
(121) Zhang, L.; Bian, Z.; Hu, A.; Li, J.; Liu, L.; Chu, F. Iodine Ions Sensing Based on Fluorescence Quenching Method and Hydrogel Fiber Doped with Fluorescein. *Opt. Commun.* **2020**, *475*, 126225. https://doi.org/10.1016/j.optcom.2020.126225.
(122) *ImageJ*. https://imagej.nih.gov/ij/index.html (accessed 2022-05-17).
(123) Tian, S.; Chen, Y.; Zhu, Y.; Fan, H. A Fluorescent Polyurethane with Covalently Cross-Linked Rhodamine Derivatives. *Polymers* **2020**, *12* (9), 1989. https://doi.org/10.3390/polym12091989.
(124) Crichton, R. R. Basic Coordination Chemistry for Biologists. In *Biological Inorganic Chemistry*; Elsevier, 2012; pp 21–34. https://doi.org/10.1016/B978-0-444-53782-9.00002-4.
(125) Hagen, W. R. EPR Spectroscopy. In *Practical Approaches to Biological Inorganic Chemistry*; Elsevier, 2013; pp 53–75. https://doi.org/10.1016/B978-0-444-56351-4.00003-8.
(126) *5.6: Crystal Field Theory*. Chemistry LibreTexts. https://chem.libretexts.org/Courses/National_Chiao_Tung_University/Chemistry_2/05%3A_Transition_Metals_and_Coordination_Chemistry_(OpenSTAX_and_Brown)/5.06%3A_Crystal_Field_Theory (accessed 2021-09-07).
(127) OpenStax. 19.3 Spectroscopic and Magnetic Properties of Coordination Compounds. **2016**.
(128) Mackay, K. M.; Mackay, R. A. *Introduction to Modern Inorganic Chemistry*, 4th ed.; Blackie Prentice Hall: Glasgow London Englewood Cliffs (N.J.), 1989.
(129) Martinho, P. N.; Gildea, B.; Harris, M. M.; Lemma, T.; Naik, A. D.; Müller-Bunz, H.; Keyes, T. E.; Garcia, Y.; Morgan, G. G. Cooperative Spin Transition in a Mononuclear Manganese(III) Complex. *Angew. Chem. Int. Ed.* **2012**, *51* (50), 12597–12601. https://doi.org/10.1002/anie.201205573.
(130) Scheuermayer, S.; Tuna, F.; Bodensteiner, M.; Scheer, M.; Layfield, R. A. Spin Crossover in Phosphorus- and Arsenic-Bridged Cyclopentadienyl-Manganese(II) Dimers. *Chem. Commun.* **2012**, *48* (65), 8087. https://doi.org/10.1039/c2cc32893c.
(131) Howarth, A. J.; Wang, T. C.; Al-Juaid, S. S.; Aziz, S. G.; Hupp, J. T.; Farha, O. K. Efficient Extraction of Sulfate from Water Using a Zr-Metal–Organic Framework. *Dalton Trans.* **2016**, *45* (1), 93–97. https://doi.org/10.1039/C5DT04163E.

(132) Kazakova, A. V.; Tiunova, A. V.; Korchagin, D. V.; Shilov, G. V.; Yagubskii, E. B.; Zverev, V. N.; Yang, S. C.; Lin, J.; Lee, J.; Maximova, O. V.; Vasiliev, A. N. The First Conducting Spin-Crossover Compound Combining a Mn III Cation Complex with Electroactive TCNQ Demonstrating an Abrupt Spin Transition with a Hysteresis of 50 K. *Chem. – Eur. J.* **2019**, *25* (43), 10204–10213. https://doi.org/10.1002/chem.201901792.
(133) Cowan, M. G.; Olguín, J.; Narayanaswamy, S.; Tallon, J. L.; Brooker, S. Reversible Switching of a Cobalt Complex by Thermal, Pressure, and Electrochemical Stimuli: Abrupt, Complete, Hysteretic Spin Crossover. *J. Am. Chem. Soc.* **2012**, *134* (6), 2892–2894. https://doi.org/10.1021/ja208429u.
(134) Guo, Y.; Yang, X.-L.; Wei, R.-J.; Zheng, L.-S.; Tao, J. Spin Transition and Structural Transformation in a Mononuclear Cobalt(II) Complex. *Inorg. Chem.* **2015**, *54* (16), 7670–7672. https://doi.org/10.1021/acs.inorgchem.5b01344.
(135) Komatsu, Y.; Kato, K.; Yamamoto, Y.; Kamihata, H.; Lee, Y. H.; Fuyuhiro, A.; Kawata, S.; Hayami, S. Spin-Crossover Behaviors Based on Intermolecular Interactions for Cobalt(II) Complexes with Long Alkyl Chains. *Eur. J. Inorg. Chem.* **2012**, *2012* (16), 2769–2775. https://doi.org/10.1002/ejic.201101040.
(136) Hayami, S.; Shigeyoshi, Y.; Akita, M.; Inoue, K.; Kato, K.; Osaka, K.; Takata, M.; Kawajiri, R.; Mitani, T.; Maeda, Y. Reverse Spin Transition Triggered by a Structural Phase Transition. *Angew. Chem. Int. Ed.* **2005**, *44* (31), 4899–4903. https://doi.org/10.1002/anie.200500316.
(137) Chmielewski, P. J.; Latos-Grażyński, L. Reactions of Nickel(II) 2,21-Dimethyl-2-Aza-21-Carbaporphyrin with Phenyl Grignard Reagents, Phenyllithium, and *n* -Butyllithium. *Inorg. Chem.* **2000**, *39* (25), 5639–5647. https://doi.org/10.1021/ic000052p.
(138) Krober, J.; Codjovi, E.; Kahn, O.; Groliere, F.; Jay, C. A Spin Transition System with a Thermal Hysteresis at Room Temperature. *J. Am. Chem. Soc.* **1993**, *115* (21), 9810–9811. https://doi.org/10.1021/ja00074a062.
(139) Kahn, O.; Martinez, C. J. Spin-Transition Polymers: From Molecular Materials Toward Memory Devices. *Science* **1998**, *279* (5347), 44–48. https://doi.org/10.1126/science.279.5347.44.
(140) Chauhan, A. Random Forest Classifier and Its Hyperparameters. *Analytics Vidhya*, 2021.
(141) Hodges, J. L. Discriminatory Analysis : Nonparametric Discrimination Consistency Properties. University of California, USAF School of Aviaton Medicine February 1951, p 24.

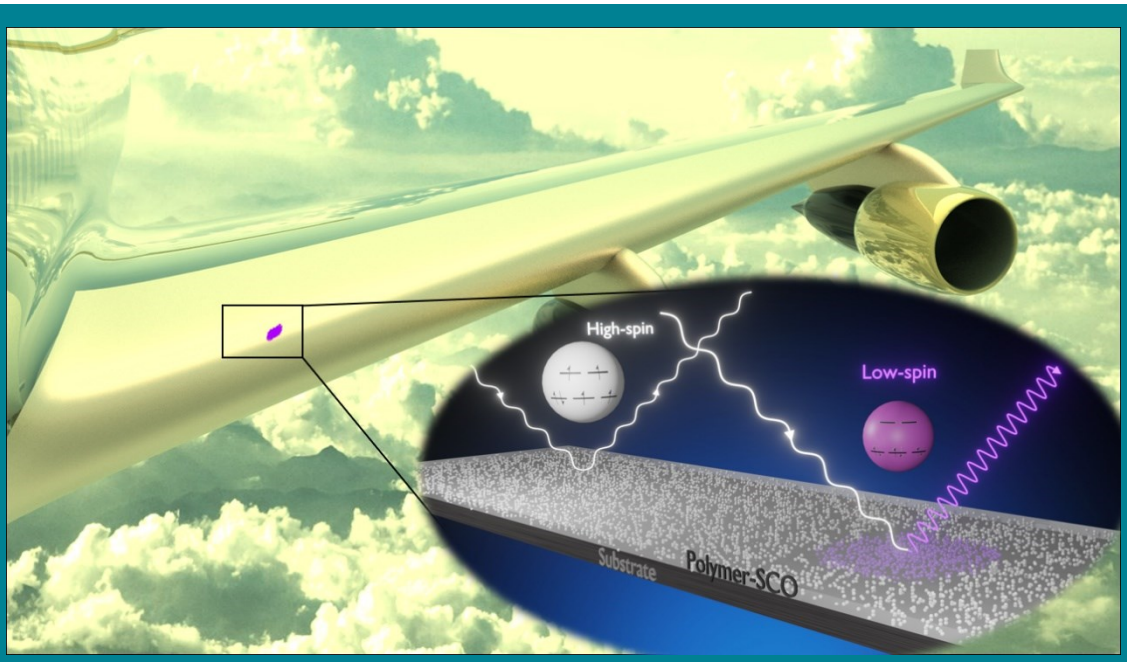

Development of Intelligent Piezochromic Materials based on Spin Crossover Complexes

Author : Arnaud Nizet

This master thesis demonstrates the piezochromic capabilities of a new type of polyurethane-spin crossover compound hybrid material for coating applications, as well as its superiority over currently researched piezochromic compounds. Two spin crossover compounds, $[Fe(NH_2trz)_3]Br_2 \cdot nH_2O$ and $Fe(pyrazine)[Fe(CN)_5NO]$ displayed degrees of compatibility with regular as well as UV-cured waterborne polyurethane matrices, with piezochromic and/or thermochromic properties for different ranges of temperature.

The piezochromic response of this hybrid material presented a mappable relationship with the pressure applied, which allowed for the development of impact detection and pressure determination models. For impact detection, an ensemble of multiple typical machine learning algorithms provided the best results. For pressure determination, “random forest” and polynomial models were found to be optimal.

This same hybrid material was then modified to provide both piezo- and thermofluorescent responses as well, by coupling the spin crossover phenomenon with the fluorescence intensity of well-known fluorophores from the fluorescein and rhodamin families.

UNIVERSITÉ CATHOLIQUE DE LOUVAIN
Faculté des bioingénieurs
Croix du Sud, 2 bte L7.05.01, 1348 Louvain-la-Neuve, Belgique | **www.uclouvain.be/agro**